

**THE INFLUENCE OF WELDING PARAMETERS ON THE  
SENSITISATION BEHAVIOUR OF 3CR12**

**By**

**Mary Louise Greeff**

Submitted in partial fulfilment of the requirements for the degree

MSc (Applied Science) Metallurgy

In the Faculty of Engineering, the Built Environment and Information Technology, University of  
Pretoria, Pretoria

2006

Dedicated to my parents, Marthinus and Dedrie Greeff.

### **Acknowledgements**

I would like to express my sincerest gratitude and appreciation to all the people and companies for their assistance during the course of this project.

- § To God the Father, Jesus Christ, our Lord and the Holy Spirit, without whom none of this would have been possible.
- § My parents, Marthinus and Dedrie Greeff for all the opportunities that they gave me.
- § My husband, Johann Petrick for his encouragement and love.
- § My parents-in-law, Johann and Louise Petrick for their wonderful support.
- § All my friends for being there with lots of tea and coffee.
- § Madeleine du Toit for her excellent guidance and hard work.
- § Prof. G.T. van Rooyen for all his brilliant suggestions.
- § Prof. Chris Pistorius for his invaluable advice.
- § Johann Borman and Charl Small that helped in too many ways to mention.
- § Mintek for the opportunity to complete the project.
- § Columbus Stainless Steel for financial sponsorship of the project.
- § Everyone at the Material Science and Metallurgical Engineering Department at the University of Pretoria.

## ABSTRACT

The sensitisation of a 12% chromium ferritic stainless steel, conforming to EN 1.4003 and available commercially in South Africa under the trade name of 3CR12, was investigated during the course of this project. 3CR12 was designed to pass through the ( $\alpha+\gamma$ ) phase field on cooling, with the austenite transforming to martensite on subsequent cooling to room temperature. The aim of this investigation was to verify that 3CR12 can sensitise during continuous cooling after welding, provided that low heat input levels are used. Two grades of 3CR12 with slightly different chemistries, designated 41220 (A) and 41311 (B), were evaluated. Grade 41220 has a higher austenite potential than grade 41311. 3CR12 plate was joined autogenously to AISI 316L by means of a series of square butt welds. Gas tungsten arc welding with argon shielding was used, and the heat input was varied from approximately 30 J/mm to 450 J/mm, in conjunction with welding speeds ranging from 2.36 mm/s to 33.3 mm/s. Rosenthal's heat flow equations were used to calculate the cooling rate from 1500°C to 800°C for each experimental weld, and to illustrate the influence of the effective heat input and welding speed on the martensite content of the high temperature heat-affected zone. An increase in welding speed reduces the heat input and increases the cooling rate after welding. At lower heat input levels (less than approximately 100 J/mm), austenite nucleation was found to be suppressed by the rapid cooling rates, and a continuous network of ferrite-ferrite grain boundaries formed in the high temperature heat-affected zone. Higher heat inputs resulted in slower cooling with more martensite in the high temperature heat-affected zone after cooling. At heat input levels above approximately 250 J/mm, enough martensite formed during cooling to eliminate a continuous network of ferrite-ferrite grain boundaries in the high temperature heat-affected zone. Sensitisation was evaluated using an electrolytic oxalic acid etch (ASTM 763-99, Practice W), and a potentiostatic etch in 0.5M H<sub>2</sub>SO<sub>4</sub>. During the potentiostatic etch test, the potential was maintained at 0 V<sub>SCE</sub> to reveal the presence of any chromium depleted zones. Both grades of 3CR12 were found to be sensitised when a continuous network of ferrite-ferrite grain boundaries was present in the high temperature heat-affected zone (i.e. after welding at low heat input levels). When the heat input during welding was high enough to ensure the presence of martensite on the majority of the heat-affected zone grain boundaries, thereby effectively eliminating continuous ferrite-ferrite grain boundary networks, the welds were not in the sensitised condition. The austenite that forms during cooling acts as a carbon sink, absorbing any excess carbon. This prevents supersaturation of the ferrite and subsequent carbide precipitation that can lead to chromium depletion and sensitisation. Due to its higher austenite potential, grade 41311 can be welded at lower heat input levels and with faster cooling rates than grade 41220 without inducing continuous carbide precipitation and sensitisation. In order to prevent sensitisation, a fusion-line cooling rate of 80°C/s should not be exceeded in 3 mm 3CR12 plate during welding.

Keywords: Continuous Cooling Sensitisation, Ferritic Stainless Steel, Duplex Stainless Steel, EN 1.4003, 3CR12, Phase Determination, Chromium Depletion Test.

## TABLE OF CONTENTS

<b>CHAPTER 1</b>	<b>GENERAL BACKGROUND</b>	<b>1</b>
1.1.	INTRODUCTION	4
1.2.	AIM OF THE INVESTIGATION	5
1.3.	REFERENCES	
<b>CHAPTER 2</b>	<b>WELDING OF 3CR12</b>	<b>6</b>
2.1.	OVERVIEW	6
	2.1.1. Welding of ferritic and duplex stainless steel	7
2.2.	WELDING OF 3CR12	10
	2.2.1. General	10
	2.2.2. Expected heat-affected zone microstructure	11
	2.2.3. Gas tungsten arc welding process	12
2.3.	HEAT INPUT AND HEAT FLOW MODELLING	12
	2.3.1. Heat input	12
	2.3.2. Rosenthal's heat-flow equations	13
	2.3.3. Approximation of the arc efficiency	15
	2.3.4. Critical thickness	16
	2.3.5. Influence of welding parameters on the cooling rate.	18
2.4.	SUMMARY	21
2.5.	REFERENCES	22
<b>CHAPTER 3</b>	<b>SENSITISATION OF 3CR12</b>	<b>23</b>
3.1.	INTERGRANULAR CORROSION THEORIES	23
3.2.	CHROMIUM DEPLETION AND CARBIDE PRECIPITATION	25
3.3.	SENSITISATION OF 3CR12	29
	3.3.1. Isothermal sensitisation	30
	3.3.1.1. <i>Double heat treatment</i>	31
	3.3.1.2. <i>Overlapping heat-affected zones</i>	31
3.4.	CONTINUOUS COOLING SENSITISATION	32
3.5.	REFERENCES	34
<b>CHAPTER 4</b>	<b>EXPERIMENTAL PLAN</b>	<b>36</b>
4.1.	ALLOYS INVESTIGATED	36
4.2.	EXPERIMENTAL PLAN	37
4.3.	MATERIAL HOMOGENISATION	38

4.4.	WELDING	38
4.5.	SENSITISATION TESTING	41
4.5.1.	ASTM A 763-93	41
	4.5.1.1 Practice Z	43
	4.5.1.2 Practice W	42
4.5.2.	Potentiostatic chromium depletion test	44
4.6.	PHASE DISTRIBUTION DETERMINATION	45
4.7.	REFERENCES	47
<b>CHAPTER 5</b>	<b>RESULTS AND DISCUSSION</b>	<b>48</b>
5.1.	MODIFIED EXPERIMENTAL PLAN	48
5.2.	WELDING	48
5.3.	PHASE DETERMINATION	50
	5.3.1. Results and Discussion	50
5.4.	THE INFLUENCE OF $q$ AND $n$ ON THE COOLING RATE	51
	5.4.1. Derivation and Calculation	51
	5.4.2. Results	52
	5.4.3. Discussion	53
5.5.	THE INFLUENCE OF $q$ AND $v$ ON THE ESTIMATED MARTENSITE CONTENT.	53
	5.5.1. Results	53
	5.5.2. Discussion	53
5.6.	SENSITISATION TESTS	55
	5.6.1. Results	55
	5.6.1.1. Practice Z: Boiling Cu-CuSO <sub>4</sub> -6%H <sub>2</sub> SO <sub>4</sub> test	55
	5.6.1.2. Practice W: 10% oxalic acid electrolytic etch	59
	5.6.1.3. Chromium depletion test	65
	5.6.2. Discussion	72
5.7.	REFERENCES	75
<b>CHAPTER 6</b>	<b>SUMMARY AND CONCLUSIONS</b>	<b>76</b>
6.1	SUMMARY	76
6.2	CONCLUDING REMARKS	78
6.3	RECOMMENDATIONS	79
	APPENDIX A	80
	APPENDIX B	81

## CHAPTER 1

## GENERAL BACKGROUND

## 1.1. INTRODUCTION

3CR12 is the trade name of a low carbon, 11 - 12% chromium stainless steel, developed and produced by Columbus Stainless, a primary stainless steel producer in South Africa. This EN 1.4003-type alloy is used extensively in the petrochemical, metallurgical, pulp, paper and sugar industries for structural applications, replacing mild and galvanized steel in mildly corrosive environments<sup>[1, 2]</sup>. The availability of 3CR12 in rolled structural sections for general engineering applications (round, square and flat bar, as well as angle and channel sections) has also increased demand and highlights the need for reliable welds. The past few years have also seen a marked increase in the use of this material in the transport, mining and agricultural sectors<sup>[3, 4]</sup>.

The specified composition range<sup>[1]</sup> of 3CR12 at the time of this investigation is given in Table 1.1. It is supplied in the fully annealed condition, its softest and most ductile state. In the annealed condition, 3CR12 is ferritic, with all the carbon precipitated as carbides and all the austenite that forms during cooling transformed to ferrite. A typical as-supplied microstructure is given in Figure 1.1, showing ferrite bands interlaced with carbide.

Table 1.1. Specified chemical composition limits (wt-%) of 3CR12 at the time of this investigation (balance Fe)<sup>[3]</sup>

C	Mn	Cr	Si	S	P	Ni	N
0.03 max	1.50 max	10.5 – 12.5	1.0 max	0.015 max	0.040 max	0.3 – 1.0 max	0.03 max

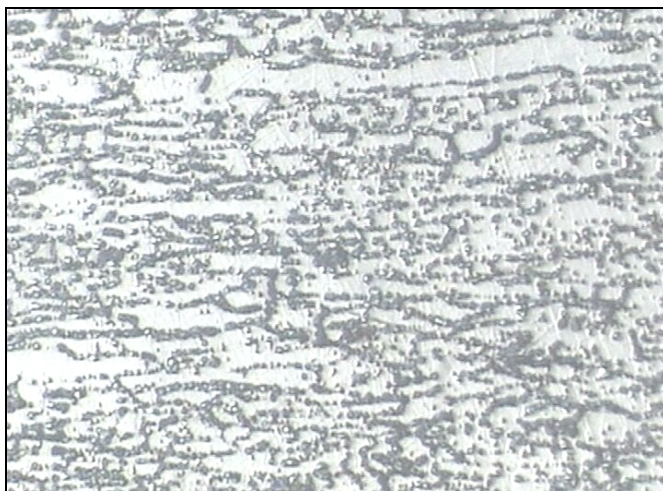


Figure 1.1. A typical microstructure of 3CR12 is shown in the as-received condition. (Etch: Oxalic acid, 1 A/cm<sup>2</sup> for 60 seconds). The light phase is ferrite and the darker particles are carbides. (500 X).

3CR12 was developed as a utility stainless steel with improved weldability over that of other low-alloyed ferritic stainless steels, such as AISI 409<sup>[1]</sup>. This was accomplished by adjusting the composition of the steel in such a way that it passes through the dual-phase,  $\alpha + \gamma$  phase field in the Fe-Cr binary phase diagram during heating and cooling (Figure 1.2). A brief review of the metallurgy of these alloys is given below for background information.

The structure of 11-12% chromium steels can vary from fully ferritic to fully martensitic with only minor changes in chemical composition, resulting in a wide range of possible properties. In Figure 1.2<sup>[5]</sup>, the Fe-Cr phase diagram, it can be seen that a dual-phase structure exists above approximately 850°C for pure Fe-Cr alloys containing approximately of 12 to 13% chromium.

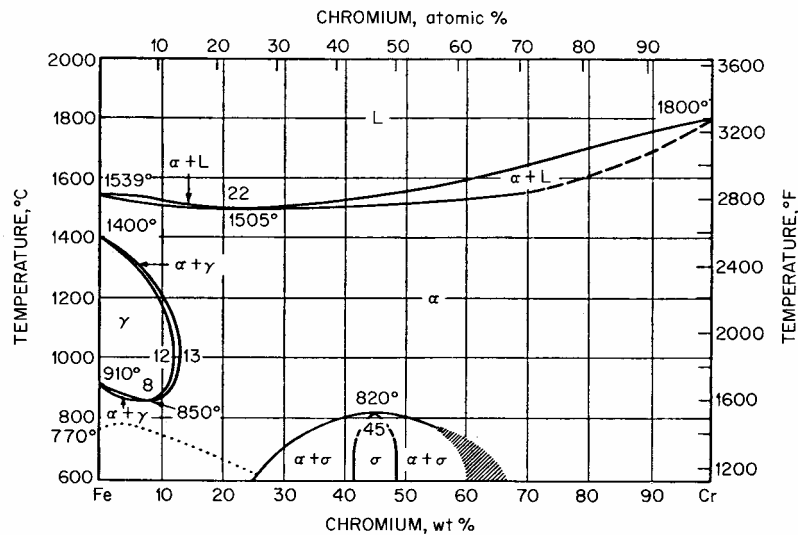


Figure 1.2. Binary iron-chromium equilibrium phase diagram<sup>[5]</sup>.

The austenite ( $\gamma$ ) and austenite-ferrite ( $\gamma$  and  $\alpha$ ) phase fields on the phase diagram are collectively known as the gamma loop. Austenite has a face centred cubic (FCC) structure and ferrite a body centred cubic (BCC) structure. At high temperatures, ferrite-forming elements (such as chromium, molybdenum and silicon) decrease the range over which austenite is stable, thereby restricting the gamma loop, whereas austenite-forming elements, such as carbon, nickel and nitrogen, enlarge it, as shown in Figure 1.3<sup>[6]</sup>.

In part (a) Figure 1.3, the Fe-Cr pseudo-binary phase diagram in the region of the gamma loop is shown for a carbon content of less than 0.01%. Below approximately 0.01% C, the carbon solubility limit in ferrite is not exceeded, and consequently no carbide precipitation occurs over the entire temperature range from the liquidus temperature to room temperature. Figure 1.3 (b) demonstrates the influence of 0.05% carbon on the phases present in Fe-Cr alloys.

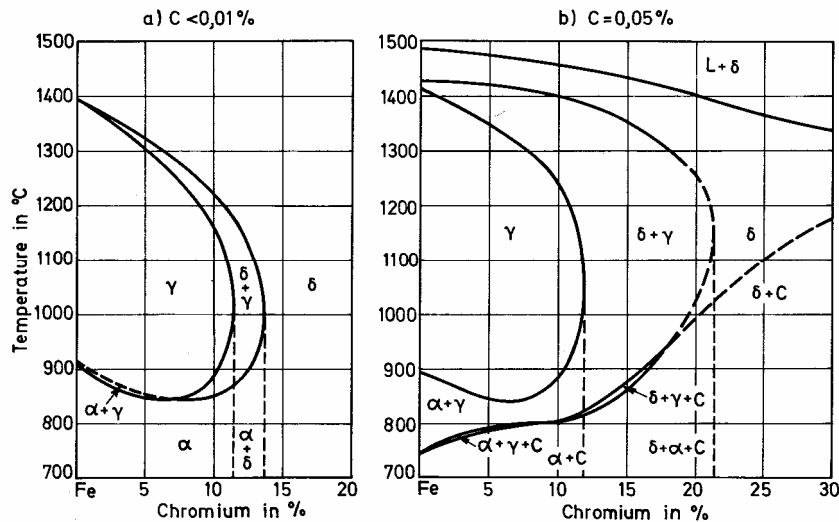


Figure 1.3. Vertical sections at (a)  $C < 0.01\%$ , and (b)  $C = 0.05\%$ , of the Fe-Cr-C ternary system, illustrating the influence of carbon on the gamma loop. C denotes  $M_{23}C_6$  in this figure<sup>[6]</sup>.

The  $\gamma$  and the  $\alpha + \gamma$  (duplex) phase fields are enlarged to about 21% Cr for 0.05 % C as shown in Figure 1.3 (b). The austenite in 3CR12 that forms at elevated temperatures during cooling will transform to martensite if no austenite-stabilising elements, such as nickel and nitrogen, are present. It is also evident from this pseudo-binary diagram that the solubility of carbon in ferrite is exceeded at lower temperatures in alloys containing 0.05 % C, and that precipitation of carbides, in this instance,  $M_{23}C_6$  (denoted by C), occurs. Carbide precipitation can occur at any temperature below which austenite is unstable, since the FCC phase has a higher solubility for carbon than the BCC phase, due to larger interstitial spaces. Therefore, a carbon content exceeding the solubility limit in ferrite promotes carbide precipitation. Figure 1.3 (b) suggests that a thermodynamic driving force for carbide precipitation always exists in 11-12% chromium alloys with sufficient carbon. The extent to which carbide precipitation occurs and its consequences, however, is a function of the composition of the alloy and the cooling rate. Carbide precipitation is, however, difficult to prevent in most commercially available ferritic stainless steels, regardless of the cooling rate.

Chromium has a higher affinity for carbon than iron. Therefore it makes up most (70 – 80%) of the metallic component of the  $M_{23}C_6$  carbide<sup>[7]</sup>. Even though Figure 1.3(b) is valid for 0.05% carbon, the 0.03 % carbon in 3CR12 consequently exceeds the carbon solubility during cooling (note the presence of carbides in the as-received microstructure shown in Figure 1.1), and therefore same principle applies.

It is important to note that the phase diagrams described above are valid for thermodynamic equilibrium conditions associated with slow cooling rates. Given enough time, the phase diagram in Figure 1.3 predicts that austenite will transform completely to  $\alpha$ -ferrite and carbide, as happens during annealing in 3CR12 (as shown in Figure 1.1).

The cooling rates associated with welding, however, are such that thermodynamic equilibrium is difficult to achieve. The high temperature austenite that forms during cooling transforms to martensite, due to a lack of

nickel and nitrogen stabilisation. This results in a duplex structure consisting of a ferrite matrix with martensite on the grain boundaries in the heat-affected zone at the normal cooling rates associated with welding. Changing the cooling rate by modifying the welding parameters can modify this duplex structure. This will be considered in more detail in Chapter 2.

## 1.2. AIM OF THE INVESTIGATION

3CR12 was believed to be mostly resistant to sensitisation during welding, due to the presence of a dual-phase microstructure in the heat-affected zone during cooling. A spate of recent in-service failures, however, attributed to stress corrosion cracking caused by sensitisation during welding, demonstrated that 3CR12 can be sensitised under certain specific conditions, and highlighted the need for further research.

This investigation concentrates on sensitisation that occurs in 3CR12 as a result of welding at very low heat input levels, and was motivated by incidents of sensitisation observed in the region of fillet welds with excessive overlap. The overlap resulted in low effective heat inputs near the toe of the welds. Excessive welding speeds, further reducing the heat input into the welds, apparently also played a role in causing failure. The results will also be of importance in view of proposals from industry to use welding processes with inherently low heat input levels, such as laser welding, to control grain growth in the heat-affected zone of 3CR12 welds. The fast cooling rates associated with low heat input welding influence the phase balance in the heat-affected zone, and can change the mechanism of sensitisation as compared to that normally observed in these EN 1.4003 type alloys.

In order to study this phenomenon, a range of heat inputs was used to weld two different grades of 3CR12. The phase composition and sensitisation resistance of the resulting heat-affected zones were then evaluated as a function of cooling rate and weld parameters.

1.3. REFERENCES

1. Grobler, C. Weldability studies on 12% and 14% chromium steels. PhD dissertation. University of Pretoria. 1987. pp. 5 – 6; 12
2. Maxwell, D.K., Dewar, K., Warrington, I. From niche to commodity, 3CR12 – a ten-year scenario. *INFACON 6. Proceedings of the 1<sup>st</sup> International Chromium Steel and Alloys Congress, Cape Town*. Volume 2. Johannesburg, SAIMM, 1992. pp. 203 – 209.
3. 3CR12 - The Utility Stainless Steel. Technical Manual published by Columbus Stainless. 1997.
4. Meyer, A. M. Interstitial diffusion from the weld metal into the high temperature heat affected zone in 11 – 12 percent chromium steel welded joints. M.Eng. thesis. University of Pretoria. (2000)
5. Peckner, P. and Bernstein, I. M. *Handbook of Stainless Steel*.. McGraw-Hill Book Company. 1977. pp. 2-4
6. Folkhard, E. Welding metallurgy of Stainless Steels. Springer-Verlag. 1988. p. 11.
7. Cowan, R.L., Tedmon, C.S. Advances in corrosion science and Technology. Vol. 3, Fontana & Staehle. 1973. p. 319.

CHAPTER 2

**WELDING OF 3CR12**

This investigation was prompted by the failure of welds as a result of sensitisation induced by the weld thermal cycle. This chapter therefore provides more information on the welding of 3CR12 and illustrates how welding parameters can influence the cooling rate after welding, and consequently also the development of the heat-affected zone microstructure.

2.1. OVERVIEW

3CR12 is welded extensively in practice. Its widespread use in structural applications highlights the need for reliable welds. Mild steel is often replaced by 3CR12 in mildly corrosive environments, and therefore the alloy and its welds should, in addition to adequate mechanical properties, also have sufficient corrosion resistance.

Recent in-service failures have brought to light the importance of welding parameters, especially heat input and welding speed, on the corrosion resistance of 3CR12 welds. The welding parameters are known to influence the cooling rate experienced by the heat-affected zone. It will be shown that the cooling rate affects the phase transformations that occur during cooling. These phase transformations, in turn, determine the sensitisation resistance of the heat-affected zone.

3CR12 is a low chromium, low carbon corrosion resistant steel. As a result of its low chromium content, 3CR12 is not susceptible to the intermetallic compound formation that plagues the higher alloyed duplex and ferritic stainless steels during welding. However, it can sensitise under specific conditions during welding. The phase transformations that occur in the heat-affected zone during cooling are critical in this respect, and it is therefore important to understand how the cooling rate is affected by the welding parameters.

Welding is a complex process. When considering a weld cross-section, each point at a given distance from the weld centre line experiences a different peak temperature and cooling rate. As the distance from the weld centre line increases, the peak temperature and the cooling rate decrease, and this influences the microstructure that develops. Five distinct areas can normally be identified in the microstructure of a 3CR12 weld, as shown in Figure 2.1. The weld bead represents the material that was completely molten during the weld thermal cycle, and consists of an admixture of 3CR12 and filler metal. The fusion line between the high temperature heat-affected zone and the weld bead is very narrow and cannot always be clearly discerned. The high temperature heat-affected zone (HTHAZ) is located adjacent to the fusion line where the peak temperatures during welding were below the melting point of the base metal, but high enough for extensive

grain growth to occur. In the case of 3CR12, the peak temperature in the high temperature heat-affected zone is typically above 1400 °C. The liquidus and solidus temperatures can vary with changes in chemical composition; the accepted values for 3CR12 are 1510°C and 1430°C, respectively <sup>[4]</sup>. The low temperature heat-affected zone (LTHAZ) represents the area where recrystallisation occurred during welding, i.e. where the temperatures were high enough for austenite to form, but not high enough for significant grain growth to occur. The unaffected parent material is located beyond the low temperature heat-affected zone.

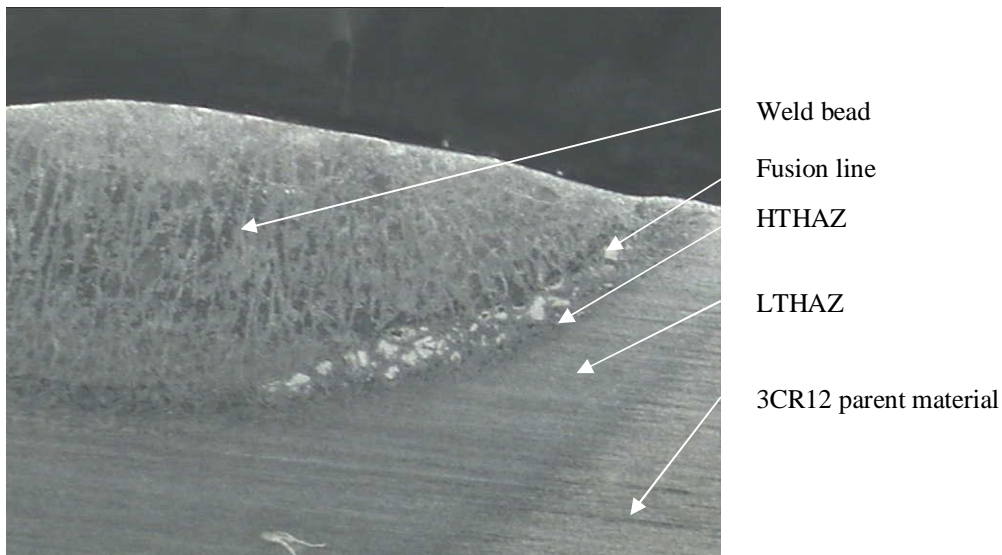


Figure 2.1. Photomicrograph of a 3CR12 weld with the different metallurgical zones highlighted (autogenous GTAW, heat input: 293.7 J/mm). (5X)

### 2.1.1. Welding of ferritic and duplex stainless steel

3CR12 was designed to pass through the  $\alpha + \gamma$  dual-phase region of the Fe-Cr-C phase diagram, shown in Figure 2.2 <sup>[6]</sup>, in order that solid-state phase transformations can aid in reducing the grain size in the high temperature heat-affected zone during welding. 3CR12 is entirely ferritic above the gamma loop, and as it cools down through the dual-phase field, austenite nucleates on the grain boundaries. If the cooling rate is not excessive (and the steel has a sufficiently high austenite potential), the austenite has time to grow and cover all available ferrite grain boundaries. At very slow cooling rates, this austenite can transform to ferrite on further cooling (as predicted by the phase diagram), but this generally does not occur during welding. 3CR12 is not sufficiently alloyed for the austenite to remain stable down to room temperature, therefore it transforms to martensite, resulting in a duplex heat-affected zone microstructure. In order to describe the influence of welding parameters on the microstructure and sensitisation resistance of 3CR12 in context, some of the important factors influencing the weldability of ferritic and duplex stainless steel are considered below.

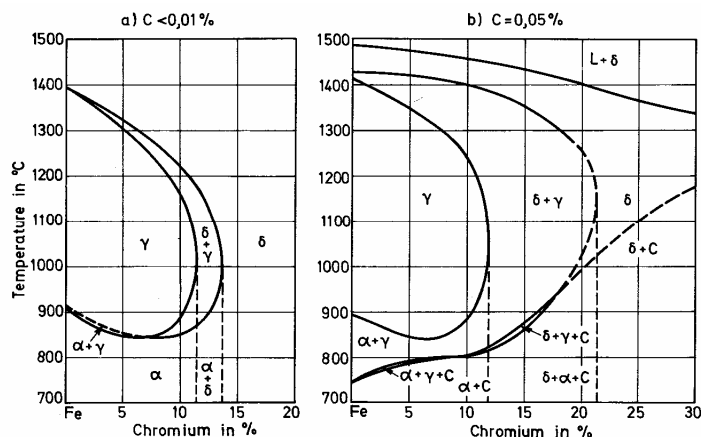


Figure 2.2. Vertical section at (a)  $C < 0.01\%$ , and (b)  $C = 0.05\%$ , of the ternary Fe-Cr-C system, showing the influence of carbon on the extent of the gamma loop<sup>[6]</sup>.

Ferritic stainless steels are essentially iron-chromium alloys containing 12% to 30% chromium as major alloying element, carbon up to a maximum of 0.25%, and other minor alloying elements. Most of the alloys that fall into this category solidify as ferrite and remain ferritic (BCC) down to room temperature under normal heat treatment conditions. They are relatively low in cost because they do not contain significant amounts of nickel. During welding, the high temperature heat-affected zone spends significant time above the grain coarsening temperature, resulting in considerable grain growth. These large grains cause low heat-affected zone ductility and toughness and contribute to the poor weldability of some of the ferritic stainless steels. The higher alloyed ferritic stainless steels also suffer from embrittlement due to sigma phase and other intermetallic compounds that can form during welding. Ferritic stainless steels may be susceptible to sensitisation (to be considered in more detail in Chapter 3).

In order to control grain growth, it is generally recommended that ferritic stainless steels are welded with little or no preheat. This increases the cooling rate after welding and reduces the amount of time spent above the grain coarsening temperature. Single-pass welds with low heat input levels are preferred, and if possible, austenitic filler metal should be used to improve the ductility and toughness of the weld.

Duplex stainless steels have higher nickel and nitrogen contents than the ferritic stainless steels, and achieve optimal mechanical and corrosion properties with a room temperature microstructure consisting of approximately equal amounts of austenite and ferrite. These steels solidify as ferrite, but upon cooling, partial transformation of ferrite to the desired amount of austenite occurs through careful control over alloy content and cooling rate. The chemical compositions of duplex stainless steels are extremely varied <sup>[1]</sup>. A generalised chemical composition range is shown in Table 2.1 to illustrate the major chemistry differences between duplex stainless steels and 3CR12.

Table 2.1. General chemical composition range for duplex stainless steels, compared with that of 3CR12 (percentage by mass, balance Fe).

Material	Cr	Ni	Mo	N	Other
Duplex	19.5 – 27	4 - 10	1.5 – 4.5	0.07 – 0.25	Some Cu, Si and Mn with N
3CR12	10.5 - 12.5	0.3 - 1.0	No deliberate addition	0.03 max	-

The dual-phase microstructure, as well as the low carbon and high nitrogen contents of the newer generation duplex stainless steels, result in excellent resistance to sensitisation and intergranular corrosion <sup>[1]</sup>.

The rapid cooling rates associated with welding suppress austenite formation and often result in an unfavourable phase balance in the weld metal and heat-affected zone of duplex stainless steel welds. Welding procedures for duplex stainless steels often focus on obtaining a phase balance similar to that of the parent material in the heat-affected zone after welding, and in this respect the cooling rate from 1200°C to 800°C is very important <sup>[2]</sup>. A cooling rate fast enough to prevent sigma phase formation and to limit grain growth is required, but enough austenite should form to ensure adequate mechanical and corrosion properties <sup>[3]</sup>. The mechanism of sensitisation in duplex stainless steels will be considered in the next chapter.

Nitrogen alloying has proved to be beneficial in promoting austenite formation, since nitrogen is a powerful austenite-former. Duplex stainless steels are generally welded with nitrogen-alloyed filler metal with increased nickel to promote the formation of austenite. Excessive dilution should be avoided, and large root gaps for welding root passes are recommended to ensure the use of enough filler metal. Duplex stainless steels suffer from brittle intermetallic phase formation and it is therefore important to avoid the temperature range between 300 °C and 1070 °C during service or heat treatment.

The lower chromium (and molybdenum) content of 3CR12 renders it resistant to 475°C embrittlement (alpha prime formation) and to embrittlement due to the precipitation of intermetallic phases (such as sigma or chi phase) during welding. Unfortunately, low ductility in the welded condition, a ductile-to-brittle-transition and sensitisation are potential problems that need to be addressed when 3CR12 is welded. Sensitisation of 3CR12 is examined in the next chapter.

It is always important to follow the manufacturer's recommendations when welding a stainless steel. The guidelines considered above are very general and by no means constitute recommended practice.

## 2.2. WELDING OF 3CR12

### 2.2.1. General

3CR12 has good weldability characteristics for a range of engineering applications, according to the Fabrication Guide of 3CR12 distributed by Columbus Stainless<sup>[4]</sup>. The heat input per welding pass should be limited to a maximum of 1.0 kJ/mm and it is recommended that an interpass temperature of 100°C should not be exceeded. Stringer beads are preferred. These recommendations aim to reduce the amount of time the material spends above the grain coarsening temperature during the weld thermal cycle, and therefore attempt to limit grain growth in the heat-affected zone.

A range of welding processes can be used to join 3CR12. The following arc welding processes are recommended:

Gas Metal Arc Welding (GMAW) or Metal Inert Gas (MIG) welding.

Gas Tungsten Arc Welding (GTAW) or Tungsten Inert Gas (TIG) welding.

Shielded Metal Arc Welding (SMAW) or Manual Metal Arc (MMA) welding.

Flux Cored Arc Welding (FCAW)

Plasma Arc Welding (PAW)

Care should be taken when using submerged arc welding, since it is an inherently high heat input process. The high heat input and efficiency of heat transfer cause excessive grain growth in the heat-affected zone, resulting in very low heat-affected zone toughness. Only with proper design and extensive procedural testing should it be considered for welding 3CR12.

Austenitic consumables are generally recommended for welding 3CR12. Although this leads to a property mismatch between the weld and the surrounding base metal, the tough austenitic weld metal improves the overall toughness of the weld by absorbing some of the impact that the joint may be exposed to during service. The recommended electrode for most processes and applications is E309L, but E308L and E316L can also be used. The compositions of these consumables are shown in Table 2.2. Matching electrodes are not recommended for applications where impact, shock, fatigue, or any other form of non-static loading is anticipated. A matching electrode is produced by Afrox in South Africa under the trade name Transarc E3CR12 (AWS designation E410NiMo, with modified chromium content), but the weld metal has been shown to suffer from the same grain growth problems as the heat-affected zone, leading to loss in strength and very low toughness. It is only specified in applications where matching corrosion resistance is important.

Table 2.2. Approximate compositions of consumables recommended for welding 3CR12 (% by mass, balance Fe).

Elements (wt. %)	C	Cr	Ni	Mn
E3CR12	0.03 max	11 – 12	1.5	1.5
E309L	0.03 max	26	13.5	2.0
E316L	0.03 max	17	12	2.0
E308L	0.03 max	20	10	0.75

### 2.2.2. Expected heat-affected zone microstructure

A weld performed with an austenitic filler metal, such as E309L, at a heat input below the specified maximum of around 1 kJ/mm, typically displays the microstructure shown in Figure 2.3. A distinctive grain growth area, the high temperature heat-affected zone, surrounds the weld metal adjacent to the fusion line. This area is bordered by an area where recrystallisation occurred during the weld thermal cycle, the low temperature heat-affected zone, resulting in a finer grain size. The unaffected parent material is located further from the weld. The typical heat-affected zone microstructure consists of ferrite grains surrounded by martensite on the grain boundaries. The martensite forms on cooling from austenite present as a grain boundary film at higher temperatures due to the partial transformation of ferrite in the dual-phase  $\alpha + \gamma$  phase field.

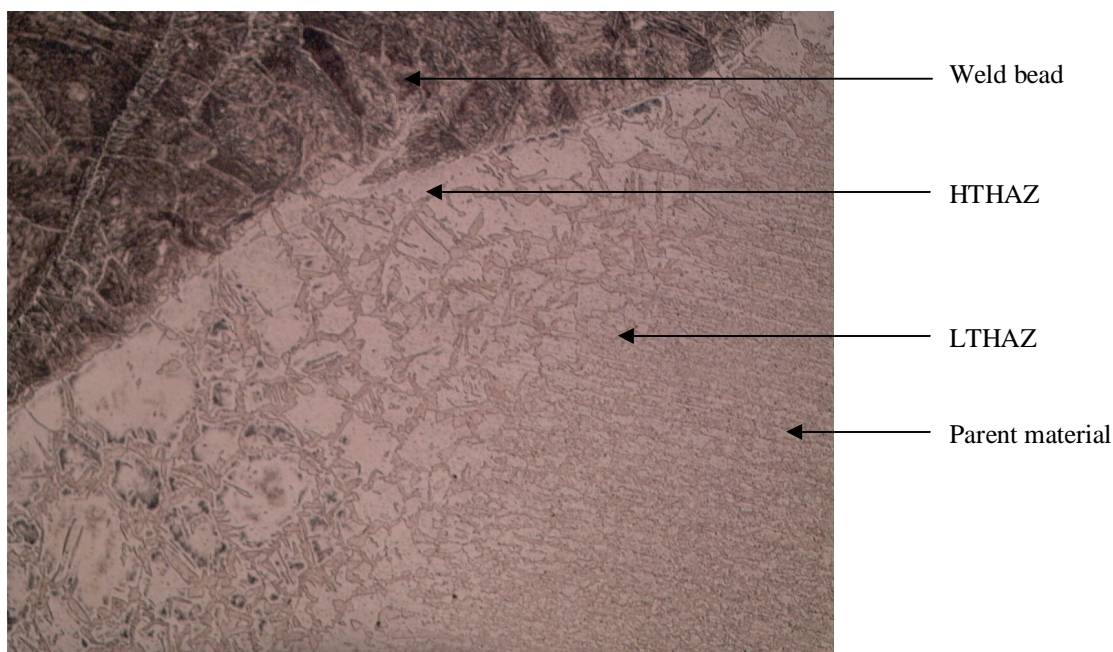


Figure 2.3. Typical 3CR12 heat-affected zone microstructure consisting of ferrite (light phase) and martensite (dark phase). Heat input: 303 J/mm. Etch: Oxalic Acid, 1 A/cm<sup>2</sup> for 60 s. (50X)

### 2.2.3. Gas tungsten arc welding process

For the purpose of this investigation, gas tungsten arc welding was selected for producing the experimental welds, since it allows close control over welding parameters, and enables bead-on-plate welds to be produced at very low heat inputs.

In this process, heat is generated from an electric arc formed between the work piece and a non-consumable tungsten electrode. Shielding provided by an inert gas, usually argon, prevents atmospheric contamination. Although a low deposition rate is obtained, high quality welds can be produced. A 1 – 2% thoriaed tungsten electrode is generally recommended for ferrous alloys, with a tip angle of 30 – 60° for optimum penetration at the lowest current range used.

Since this investigation was aimed at establishing the influence of heat input and cooling rate on the heat-affected zone microstructure and sensitisation resistance of 3CR12 welds, these factors are considered in more detail below.

## 2.3. HEAT INPUT AND HEAT FLOW MODELLING

### 2.3.1. Heat input

One of the most important parameters in fusion welding is the heat input rate, given by Equation 2.1. Its importance stems from the fact that it controls the heating and cooling rates, as well as the weld pool size, to a large extent. Generally, a high heat input results in larger weld pools and slower cooling rates. Slower cooling increases the amount of time spent above the grain coarsening temperature during the weld thermal cycle, leading to coarser heat-affected zone microstructures. Cooling rates can therefore be controlled by manipulating the heat input rate. This has important metallurgical consequences, influencing the strength, ductility, impact toughness, and sensitisation behaviour of 3CR12.

If  $V$  represents the arc voltage,  $I$  the welding current,  $v$  the welding speed, and  $h$  the proportion of the arc energy that is transferred as heat to the workpiece, the heat input rate per unit length of weld is given by:

$$\text{Heat input} = HI = \frac{hVI}{v} = \frac{q}{v} \quad (2.1)$$

where:  $q$  is the power or heat flux (W).

The arc efficiency,  $h$ , is a function of the welding process, with some typical values shown in Table 2.3. Gas tungsten arc welding has a low arc efficiency compared to other popular arc welding processes due to heat losses caused by electrode heating during welding.

Table 2.3. Arc efficiencies for the different welding processes<sup>[6]</sup>.

Process	Arc efficiency, $h$
Shielded Metal Arc Welding (SMAW)	0,70 - 0,85
Gas Tungsten Arc Welding (GTAW)	0,22 - 0,48
Gas Metal Arc Welding (GMAW)	0,66 - 0,75
Submerged Arc Welding (SAW)	0,90 - 0,99

### 2.3.2. Rosenthal's heat-flow equations

In order to quantify the influence of heat input on the weld thermal cycle, conduction-driven heat flow in the heat-affected zone can be modelled. The most widely used solutions to the heat flow equations of a moving point heat source were given by Rosenthal<sup>[5]</sup>.

In order to solve the heat-flow equations, Rosenthal made a number of assumptions. The most important of these assumptions are listed below<sup>[5]</sup>:

1. The plate is semi-infinite.
2. The welding arc is represented by a moving point source or line. This assumption leads to the prediction of an infinite temperature under the arc. The solutions to the equations are therefore only appropriate some distance away from the source of heat, and should only be applied in the heat-affected zone.
3. Changes of state and temperature do not affect material properties such as thermal conductivity, specific heat and thermal diffusivity.
4. No radiative heat losses or convective flow occurs, heat transfer is by conduction only. Heat losses at the plate surface are negligible.
5. Latent heat changes due to phase transformations are ignored.

The energy delivered to the workpiece is defined as  $q/v$ , and the workpiece experiences this as a short, intense pulse of linear power. The arc moves faster than the heat can dissipate (as determined by the thermal diffusivity), so that heat flow perpendicular to the travel direction is large compared to heat flow in the travel direction. The time taken to dissipate the heat depends on whether heat flow is two- or three-dimensional. For thick plate, heat flow is assumed to be three-dimensional and the cooling time is inversely proportional to the thermal conductivity,  $k$ , and independent of the plate thickness. For a thin plate, heat flow is two-

dimensional and a function of the plate thickness, the thermal conductivity and the specific heat per volume of material,  $rc$ .

Before the Rosenthal equations could be applied to quantify the influence of heat input on the cooling rate after welding for the experimental welds examined in this investigation, it was necessary to characterise heat flow as either two-, or three-dimensional.

As a preliminary step, the critical thickness (or the transition thickness between thick and thin plate conditions),  $d'$ , was calculated according to Equation 2.2:

$$d' = \sqrt{\frac{q}{2rcv} \left( \frac{1}{773 - T_0} + \frac{1}{1073 - T_0} \right)} \quad (2.2)$$

where:

$T_0$  is the original temperature of the plate prior to welding (K),

$q$  is the work transferred to the plate (W),

$v$  is the welding speed ( $\text{ms}^{-1}$ ), and

$rc$  is the specific heat per unit volume ( $\text{Jm}^{-3}\text{K}^{-1}$ ).

Equation 2.2 was originally derived for carbon steels welds, where the cooling rate through the temperature range from 800°C (1073 K) to 500°C (773 K) is critical, since most solid-state phase transformations from austenite to its transformation products (ferrite/pearlite/bainite/martensite) occur within this temperature range (800°C is the approximate A3 transformation temperature, and 500°C represents the lower limit where diffusional changes in the microstructure can occur). For the purpose of this investigation, the critical temperature range was adjusted to consider cooling from 1500°C to 800°C. This temperature range represents the time required to cool from just below the liquidus temperature, to a temperature just below the gamma loop on the phase diagram. For 3CR12, Equation 2.2 then becomes:

$$d' = \sqrt{\frac{q}{2rcv} \left( \frac{1}{1073 - T_0} + \frac{1}{1773 - T_0} \right)} \quad (2.3)$$

The material properties required in the Rosenthal equations were obtained from Columbus Stainless, and are shown in Table 2.4.

Table 2.4: Material Properties of 3CR12<sup>[4]</sup>

Volume thermal capacity ( $rc$ ) ( $\text{Jm}^{-3}\text{K}^{-1}$ )	$3.69972 \times 10^6$
Thermal diffusivity ( $a = l/rc$ ) ( $\text{m}^2\text{s}^{-1}$ )	$1.10819 \times 10^5$
Thermal conductivity ( $l$ ) ( $\text{Wm}^{-1}\text{K}^{-1}$ or $\text{Jm}^{-1}\text{s}^{-1}\text{K}^{-1}$ )	41.0

Preliminary calculations for a plate thickness of 3 mm, performed using heat input values calculated from the measured welding parameters without considering the arc efficiency factor, showed that two-dimensional heat flow (thin plate conditions) exist in the experimental welds.

### 2.3.3. Approximation of the arc efficiency

In order to study the influence of heat input on the microstructure and sensitisation resistance of 3CR12 welds, experimental welds were produced at heat input levels ranging from 70 J/mm to 900 J/mm (calculated from Equation 2.1 without considering the arc efficiency,  $h$ ). The original matrix of welding parameters selected for the experimental welds is shown in Table A.1 in the Appendix. In order to accurately ascertain the influence of heat input on cooling rate, the actual heat input during welding had to be determined. As shown in Equation 2.1, the actual heat input is a function of the welding parameters and the arc efficiency factor,  $h$ . A simplification of Rosenthal's equation for two-dimensional heat flow, Equation 2.4, was therefore used to calculate the arc efficiency by comparing the actual  $q/v$  required to produce a weld with a given weld pool diameter (measured experimentally) with the heat input calculated from the welding parameters.

$$T_p - T_0 = \sqrt{\frac{2}{pe}} \frac{q/v}{drc2r} \quad (2.4)$$

where:  $T_p$  is the peak temperature during the weld thermal cycle at a specific position, defined by  $r$ , in the heat-affected zone (K),  
 $d$  is the plate thickness (m), and  
 $r$  is the radial distance from the weld centre line (m).

For a plate thickness of 3 mm,  $d$  is equal to 0.003 m and the volume thermal heat capacity,  $rc$ , is  $3.69972 \times 10^6 \text{ Jm}^{-3}\text{K}^{-1}$  (from Table 2.4). If  $r$  is assumed to be the distance from the centre of the weld to the fusion line (or half of the weld bead width), the peak temperature at that point is equal to the liquidus temperature of the alloy. The distance,  $r$ , was measured experimentally for a number of welds. As no pre-heating was

performed prior to welding,  $T_o$  is assumed to be room temperature or 298 K, while the liquidus temperature ( $T_p$ ) is assumed to be 1500°C (1773 K). If these values are substituted into Equation (2.4), a value for the actual heat input ( $q/v$ ) can be approximated for any specific weld (given that  $r$  on the fusion line is known). The calculated heat inputs,  $q/v$ , are shown in Table 2.5. By comparing these heat input values with the heat inputs estimated from the welding parameters ( $V$ ,  $I$  and  $\eta$ ), the arc efficiency factor can be determined.

As shown in Table 2.5, the efficiency of the welding machine used during this investigation,  $h$ , is estimated to be 47.76% on average. This value approaches the upper end of the range given in Table 2.3, since electrode negative polarity, which focuses the majority of the heat generated by the machine into the workpiece and limits electrode heating, was used for welding.

For each experimental weld, the actual heat input was then calculated using Equation 2 by considering the measured weld parameters and an average arc efficiency of 47.76%. These heat input values will be considered in more detail in Chapter 4.

#### **2.3.4. Critical thickness**

Before Rosenthal's equations can be applied to calculate the cooling rates of the experimental welds, the critical thickness,  $d'$ , has to be recalculated using the actual heat input values calculated by taking the arc efficiency into consideration. This is necessary in order to confirm that heat flow during welding was two-dimensional. The actual heat input values were substituted into Equation 2.3, and new  $d'$  values were determined for each heat input.

The calculated critical thickness values for the actual heat inputs used in this investigation are shown in Table 2.6. Since  $d'$  is always greater than the plate thickness, 3 mm, heat flow occurred under thin plate (two-dimensional) conditions in all the experimental welds.

Table 2.5. Calculation of the arc efficiency of the welding machine by estimation of the heat input.

<b>HI (from welding parameters)</b>	<b><math>q/v</math> (calculated)</b>	<b><math>h</math></b>
<b>J/mm</b>	<b>J/mm</b>	
70000	50360	0.7194
100000	54693	0.5469
200000	97752	0.4888
300000	144057	0.4802
400000	165260	0.4132
500000	241497	0.4830
600000	259626	0.4327
700000	278806	0.3983
800000	283662	0.3546
900000	413134	0.4590
<b>Average</b>		<b>0.4776</b>

Table 2.6. Calculation of the critical thickness with and without  $h$  for the temperature range 1500°C to 800°C.

<b>HI (from welding parameters)</b>	<b><math>d</math> for HI</b>	<b><math>h \times HI</math></b>	<b><math>d</math> for <math>h \times HI</math></b>
<b>(J/m)</b>	<b>(mm)</b>	<b>(J/m)</b>	<b>(mm)</b>
70000	4.9	32760	3.4
100000	5.9	46800	4.1
200000	8.4	93600	5.8
300000	10.2	140400	7.1
400000	11.8	187200	8.2
500000	13.2	234000	9.1
600000	14.5	280800	10.0
700000	15.6	327600	10.8
800000	16.7	374400	11.5
900000	17.7	421200	12.2

### 2.3.5. Influence of welding parameters on the cooling rate.

In order to determine the influence of the welding speed and heat flux or power,  $q$ , on the time taken to cool from 1500°C to 800°C after welding, Rosenthal's original heat flow equation for thin plate, Equation 2.5, has to be considered. Rosenthal envisaged a heat source (arc) moving at a constant speed,  $v$ , along the  $x$ -axis of a moving rectangular coordinate system, as shown in Figure 2.4. In Equation 2.5,  $x$  is the distance of the point heat source from some fixed position along the  $x$ -axis and is dependent on the velocity of the moving source, as shown in Equation 2.6.

$$T - T_0 = \frac{q}{2I d \sqrt{\rho v r / a}} \exp\left(-\frac{v(x+r)}{2a}\right) \quad (2.5)$$

where:  $T$  is the temperature at a radial distance  $r$  from the heat source (K),

$I$  is the thermal conductivity ( $\text{Wm}^{-1}\text{K}^{-1}$  or  $\text{Jm}^{-1}\text{s}^{-1}\text{K}^{-1}$ ),

$a$  is the thermal diffusivity ( $\text{m}^2\text{s}^{-1}$ ), where  $a = I/\rho c$   $\text{m}^2\text{s}^{-1}$ ,

$x$  is the distance from the moving heat source in the  $x$ -direction ( $x > 0$  for points in front of the heat source, and  $x < 0$  for points behind the heat source), and

$r$  is the radial distance from the heat source where:

$$r = \sqrt{\xi^2 + y^2 + z^2}$$

$$x = x - vt \quad (2.6)$$

where:  $t$  is time (s).

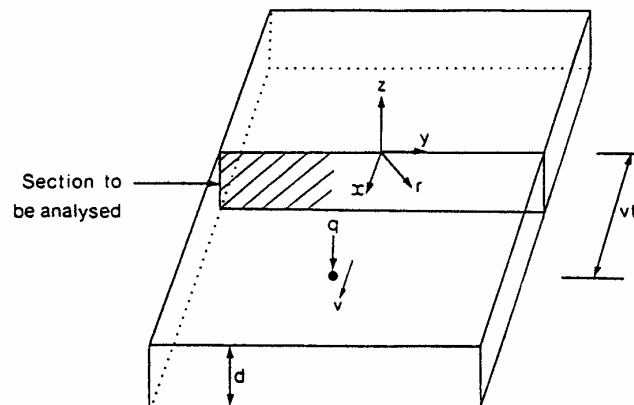


Figure 2.4 Welding configuration in terms of a point heat source,  $q$ , and a constant velocity,  $v$ .

Equation 2.5 was used to calculate the thermal cycle experienced by a point on the fusion line of each experimental 3CR12 weld. As a first step, the distance from the weld centre line to the fusion line (i.e. the width of the weld bead) was calculated for each weld, supposing that the temperature of a point on the fusion line is equal to the liquidus temperature (approximately 1500°C). This was done by assuming that  $x = 0$ ,  $y = r$  and  $z = 0$  when the heat source is in line with the point on the fusion line. Since  $x = x + vt$  and  $t = 0$  seconds when the heat source is in this position,  $x = 0$ . Equation 2.5 then becomes:

$$T - T_0 = \frac{q}{2I d \sqrt{\rho v y / a}} \exp\left(-\frac{v y}{2a}\right) \quad (2.7)$$

This calculated distance,  $y$ , and  $x = vt$  (for assumed values of  $t$ ) was then used to calculate  $r$  as a function of time as the heat source moves away from the point (defined by  $x = 0$ ) on the fusion line. The calculated  $r$ -values were substituted into Equation 2.5 to calculate the thermal cycle of a point on the fusion line as a function of heat flux,  $q$ , and the welding speed,  $v$ .

The cooling curves will be considered in more detail in Chapter 5, but the thermal cycles experienced by a point on the fusion line of a 3CR12 weld on 3 mm plate for low, intermediate and high heat input levels are shown in Figures 2.5 to 2.7. These thermal profiles were calculated for times starting at 10 seconds before the heat source passes the point, until the temperature falls below 800°C during cooling. The differences in the temperature profiles are evident. For a low heat input and a fast welding speed (shown in Figure 2.5 for a heat input of 33.7 J/mm and a welding speed of 33 mm/s), a sharp temperature peak is shown, signifying rapid heating and cooling. A cooling time of only 0.22 seconds is required for the temperature to decrease from 1500°C to 800°C at the fusion line. At an intermediate heat input (153.6 J/mm at a welding speed of 8.23 mm/s), the cooling rate is noticeably slower (Figure 2.6), and a cooling time of 2.08 seconds is required for cooling from 1500°C to 800°C. Welding at a high heat input (431.5 J/mm at a welding speed of 2.36 mm/s), yields the slowest cooling rates (Figure 2.7). A cooling time of 18.4 seconds is required for the temperature to decrease from 1500°C to 800°C at the fusion line.

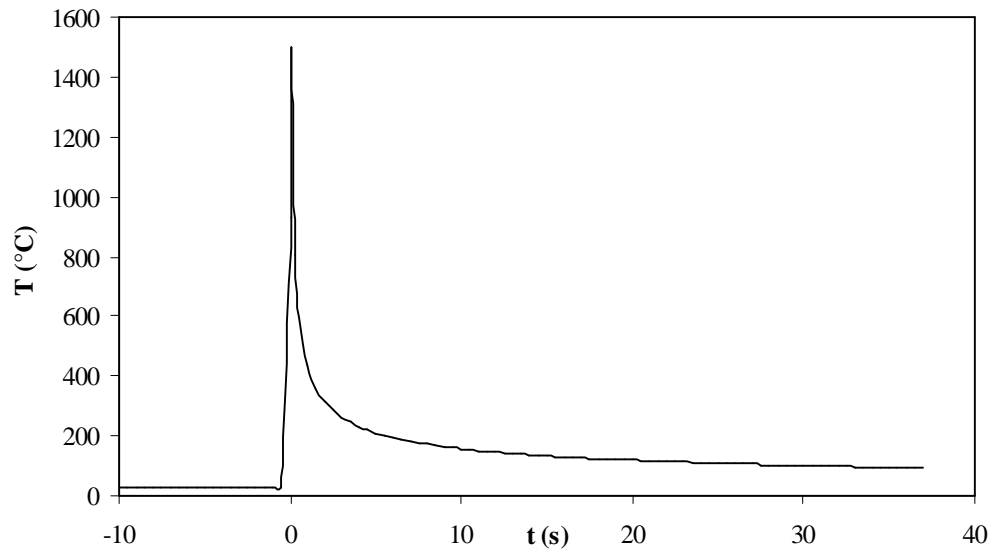


Figure 2.5. Calculated temperature-time profile experienced by a point on the fusion line for a low heat input weld (168 A, 14 V and 33.3 mm/s, yielding 33.7 J/mm). Cooling time from 1500°C to 800°C = 0.22 s.

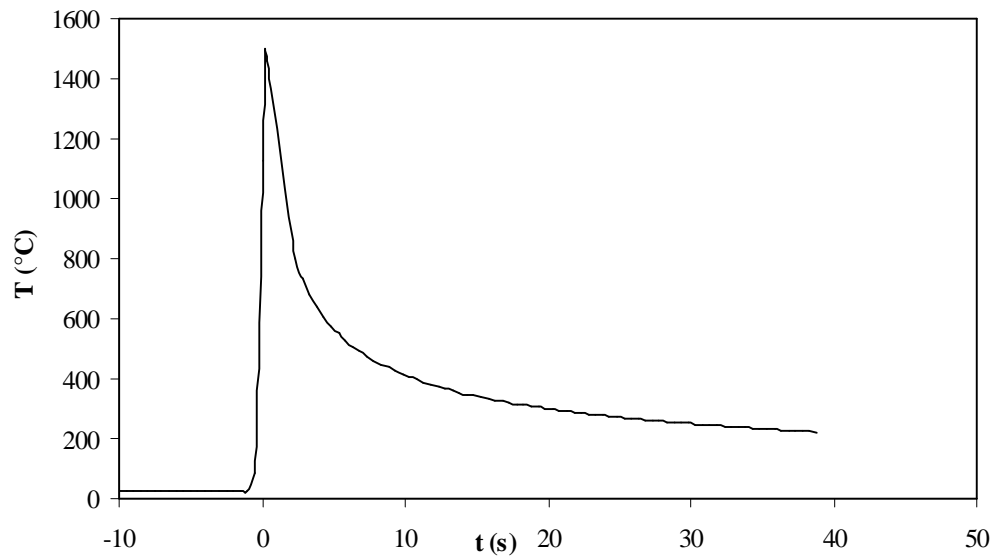


Figure 2.6. Calculated temperature-time profile experienced by a point on the fusion line for an intermediate heat input weld (189 A, 14 V and 8.23 mm/s, yielding 153.6 J/mm). Cooling time from 1500°C to 800°C = 2.08 s.

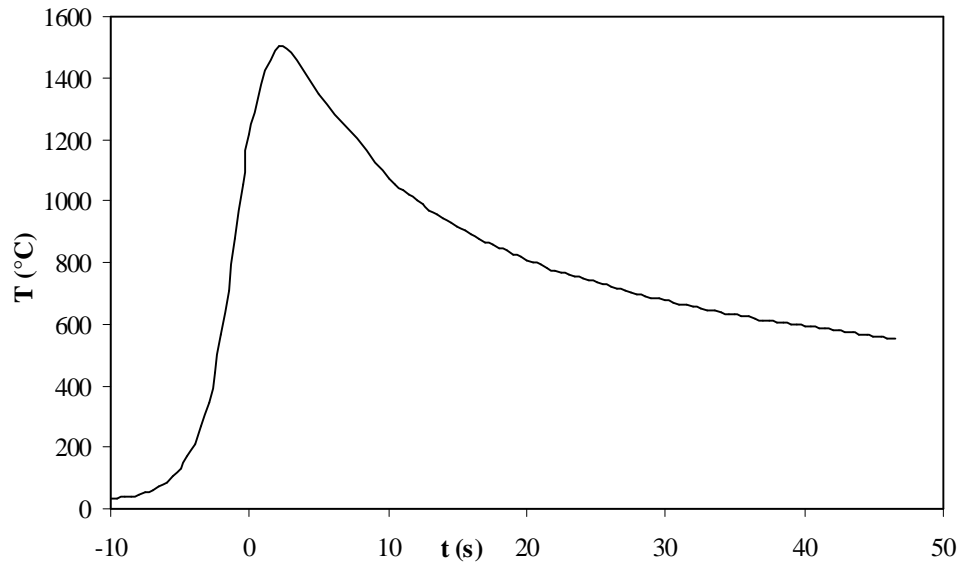


Figure 2.7. Calculated temperature-time profile experienced by a point on the fusion line for a high heat input weld (164 A, 13 V and 2.36 mm/s, yielding 431.5 J/mm). Cooling time from 1500°C to 800°C = 18.40 s.

#### 2.4. SUMMARY

This chapter describes some of the important aspects related to the welding of 3CR12, including the expected heat-affected zone microstructures, and the recommended welding processes, consumables and practices. Gas tungsten arc welding was selected for the experimental welds during the course of this project, since it allows autogenous welding and close control over welding parameters. In order to determine the influence of the heat input and welding parameters on the cooling rate and heat-affected zone microstructure of 3CR12, a range of welding parameters were selected, resulting in heat inputs ranging from 70 J/mm to 900 J/mm, and welding speeds from 1.67 mm/s to 33.3 mm/s.

Rosenthal's heat flow equations were used to calculate the efficiency of the welding machine and to estimate the actual heat input for each experimental weld. These heat inputs were then used to determine the thermal cycle experienced by a point on the fusion line of the experimental 3CR12 welds. An increase in heat input results in the prediction of slower cooling rates, whereas a low heat input causes very rapid cooling. The influence of cooling rate on sensitisation will be considered in the next chapter.

2.5. REFERENCES

1. Charles, J. Super duplex stainless steel: structure and properties. Volume 1. Duplex Stainless Steel '91. Beaunne, Bourgogne, France. Les Editions de Physique. October 1991. pp. 3 – 48
2. Lindblom, B. E. S. & Hannerz, N. Austenite reformation in HAZ of ferritic austenitic stainless steel. Volume 2. Duplex Stainless Steel '91. Beaunne, Bourgogne, France. Les Editions de Physique. October 1991. pp. 951 – 958
3. Bernharsson, S. The corrosion resistance of duplex stainless steel. Volume 1. Duplex Stainless Steel '91. Beaunne, Bourgogne, France. Les Editions de Physique. October 1991. pp. 185 – 210
4. Fabrication guide of 3CR12. Published by Columbus Stainless.
5. Rosenthal, D. The theory of moving sources of heat and its application to metal treatments. Transactions of the AIME. Vol. 68. November 1946 pp. 849-866.
6. Folkhard, E. Welding metallurgy of Stainless Steels. Springer-Verlag. 1988. p. 11

CHAPTER 3

**SENSITISATION OF 3CR12**

3.1. INTERGRANULAR CORROSION THEORIES

A brief description of the mechanism of sensitisation in stainless steels is given below, in order to place the sensitisation of 3CR12 welds in the proper context.

Intergranular corrosion in stainless steel is believed to occur when chromium is depleted from the grain boundary areas. Since chromium is required for passivation, the depleted grain boundary regions are less corrosion resistant than the bulk material, and may suffer preferential attack on exposure to a corrosive environment. In stainless steels, this phenomenon appears to be associated with the precipitation of chromium-rich carbides at the grain boundaries during heat treatment within the carbide precipitation temperature range. The resultant structure is described as being “sensitised” to intergranular corrosion.

There are three widely recognised theories explaining the influence of carbide precipitates in the mechanism of intergranular corrosion <sup>[1]</sup>: the chromium depletion theory, the stress theory, and the microcell theory. Although the chromium depletion theory is supported by overwhelming experimental proof in the majority of stainless steels <sup>[1-4]</sup>, evidence in some types of stainless steel substantiates the other theories <sup>[1]</sup> under specific conditions, as summarised by Číhal (1983). The chromium depletion theory is the main concern of this study, and will be discussed in detail below. A short description of the other two theories is included for the sake of completeness.

The stress theory suggests that considerable local stresses are generated when the carbides precipitate and grow. This occurs preferentially at the grain boundaries and substantial energy differentials develop in the steel structure, which may lower the polarization of the anodic reaction areas adjacent to the grain boundaries. This sometimes causes imperfect passivation of the boundaries, resulting in intergranular corrosion. This theory does not account for the reduced sensitivity to intergranular corrosion frequently observed after extended periods of time in the carbide precipitation range, and will therefore be discounted in this investigation.

The microcell theory proposes that intergranular attack may be due to local electrochemical cells that form in the vicinity of the carbides. The theory suggests that the carbide, normally more noble, acts as the cathode and the neighbouring, less noble bulk metal forms the anode. This implies that a prolonged heat treatment within the carbide precipitation and growth temperature range would result in more pronounced intergranular attack. The converse has been observed experimentally, and this can be satisfactorily

explained by referring to the back-diffusion of chromium to the depleted zone. As a result, grain boundary chromium depletion appears to be the dominant mechanism for sensitisation in the majority of stainless steels.

The chromium depletion theory, illustrated schematically in Figure 3.1, holds that sensitisation to intergranular attack is due to the formation of chromium-depleted zones along the grain boundaries caused by intergranular chromium carbide precipitation. These precipitates, typically  $M_{23}C_6$  type carbides, are highly enriched in chromium. If chromium depletion reduces the chromium level in the affected areas to below the concentration required to maintain passivation, intergranular corrosion can ensue. This mechanism holds for all stainless steels, even though different sensitising conditions are required for the various types of stainless steels. Although the presence of carbides does not always result in sufficient chromium depletion to cause sensitisation, it is important to understand the conditions under which chromium depletion can occur.

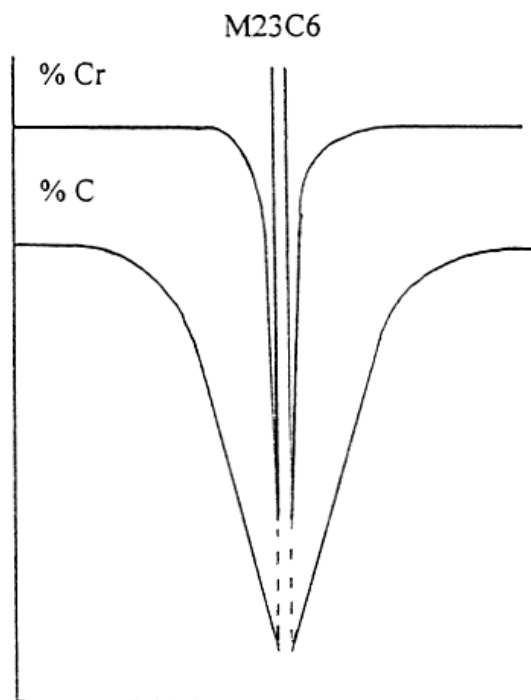


Figure 3.1. Schematic representation of chromium and carbon levels around a chromium carbide as the steel is sensitised.

A thorough understanding of the mechanism of carbide precipitation in ferritic and duplex ferritic-martensitic stainless steels is of importance in this investigation, since 3CR12 is a ferritic stainless steel that has a duplex structure of ferrite and austenite at high temperatures. This transforms to a dual-phase ferrite-martensite structure in the heat-affected zone on cooling after welding. The conditions required for

precipitation of carbides in ferrite, austenite and martensite will be considered below, followed by a discussion of the different ways in which 3CR12 can be sensitised.

### 3.2. CHROMIUM DEPLETION AND CARBIDE PRECIPITATION

Carbides can potentially be present in all Fe-Cr-C alloys containing more than about 0.01% carbon (see Figure 1.3, Chapter 1). The mechanism of sensitisation depends on the type of stainless steel, and in particular on the crystal structure of the bulk material. Stainless steels are typically classified as austenitic, ferritic or martensitic based on the dominant phase structure (as shown in Table 3.1). The phase composition is, in turn, primarily dependent on the chemical composition of the steel. The austenite-ferrite balance is mainly determined by the ratio of austenite-forming to ferrite-forming elements in the steel. Stainless steel structures can range from fully austenitic (at high levels of  $\gamma$ -forming elements such as Ni, C and/or N), to duplex  $\alpha + \gamma$  at lower ratios, to fully ferritic at high concentrations of  $\alpha$ -formers, such as Cr and Mo. The stability of the austenite at lower temperatures is determined by the level of  $\gamma$ -stabilising elements, such as Ni and N. At lower concentrations of these elements, austenite can transform to martensite on cooling due to the high hardenability of these steels. The martensite that forms on transformation inherits the chemical composition of the austenite parent phase.

*Table 3.1. Summary of dominant phases in stainless steels with their respective crystal structures*

Abbreviation	Unit cell type	Stainless steel type	Magnetic or non-magnetic
FCC	Face centred cubic	Austenitic	Non-magnetic
BCC	Body centred cubic	Ferritic	Magnetic
BCT	Body centred tetragonal	Martensitic	Magnetic

These crystal structures also determine the solubility and diffusion rates of each element in the alloy, and therefore influence the kinetics of carbide precipitation and sensitisation in stainless steels.

Austenite has a higher maximum carbon solubility limit than ferrite, due to larger interstitial spaces in the FCC lattice, although carbon diffuses faster in ferrite than in austenite at comparable temperature <sup>[15]</sup>. Carbon is an austenite-forming element and preferentially partitions to the austenite if this phase is present. With higher carbon solubility of austenite, lower carbon contents significantly delay carbide precipitation and the austenite can become largely immune to sensitisation.

Chromium, on the other hand, has a BCC unit cell structure and is therefore a ferrite-forming element. Its diffusion rate is much faster in ferrite than in austenite. Chromium partitioning between ferrite and austenite also occurs with chromium segregating preferentially to the ferrite phase, resulting in a lower chromium content in the austenite.

Due to slower chromium diffusion rate in austenite than in ferrite at comparable temperatures, sensitisation in austenitic stainless steels can generally be prevented by heating the steel to a temperature above the carbide dissolution range, followed by rapid cooling to room temperature. The slow chromium diffusion rate does not allow the carbides to reprecipitate during the quench, and the resulting austenitic structure will be immune to sensitisation unless it is reheated within the carbide precipitation range. Carbide precipitation in ferritic steels is, however, difficult to avoid, promoted by both the low carbon solubility and the rapid chromium diffusion rate. Even rapid quenching from a temperature above the carbide dissolution range cannot prevent precipitation.

The diffusion rate of carbon as an interstitial element is much greater than that of chromium, whether in austenite, ferrite or martensite. As a result of the slow diffusion rate of chromium, most of the chromium required to form the chromium-rich carbides during precipitation, will be supplied by the volume of material immediately adjacent to the particles, resulting in a steep concentration gradient in the bulk phase surrounding the carbide precipitates (as shown schematically in Figure 3.1). If the carbide particle distribution is such that the chromium depleted regions overlap and a continuous low-chromium path is formed, then the stainless steel may be sensitised. For the steel to desensitise, chromium must diffuse back to the depleted grain boundary areas from the grain interior.

The differences between austenite and ferrite described above account for the different sensitisation kinetics observed. Austenite has a higher carbon solubility, therefore it is easier to produce low-carbon equivalents of standard grades that do not suffer from carbide precipitation and would therefore be almost immune to sensitisation. If the solubility of carbon in austenite is exceeded, the kinetics of carbide precipitation is relatively slow, although it accelerates as the carbon content increases. However, once austenite has sensitised, the diffusion rate of chromium is so slow in the FCC structure that desensitisation through heat treatment is prohibitively slow, as seen in Table 3.2 <sup>[7]</sup>.

In ferrite, however, carbide precipitation is difficult to prevent, yet the back-diffusion of chromium in the BCC structure is generally fast enough for self-healing to be possible. If not, the time required for a desensitising heat treatment may not be prohibitive. Once a ferritic stainless steel is fully recovered, it can only be resensitised if heated to a temperature high enough to dissolve the carbides, followed by rapid cooling.

Chromium carbides form at different temperatures in austenite and ferrite. In austenite the precipitation temperature range is between about 480°C and 760°C, and in ferrite between 550°C and 850°C. Different cooling rates are required for austenite and ferrite in order to sensitise during continuous cooling through the susceptible temperature range. Austenite requires a slow cooling rate to sensitise, and ferrite a fast cooling rate. The precipitation kinetics for austenite is relatively sluggish, so that slow cooling will allow

the carbides time to precipitate. Unfortunately, the cooling rates are usually not slow enough to allow the back-diffusion of chromium in order for the sensitised austenite to heal. Ferrite sensitises rapidly as soon as it enters the carbide precipitation temperature range. A slow cooling rate will allow enough time for healing, resulting in a desensitised structure. At faster cooling rates, carbide precipitation will still occur, but the diffusion of chromium will be hampered. If the cooling rate is fast enough, little or no back-diffusion of chromium will occur and the ferrite remain in the sensitised condition.

*Table 3.2. Calculation performed for 1Cr19Ni9 steel: approximate periods needed for concentration of chromium at the grain boundaries to level out. [7]*

Temperature (°C)	Levelling out of chromium content across a grain boundary at the specified temperature (hours)	
	To 12% chromium	Complete
550	1915	3800
650	248	495
750	59	108
850	19	37

In ferrous alloys martensite is a metastable phase that forms through a diffusionless shear transformation from FCC austenite to a BCT body centred tetragonal structure. This transformation starts at the martensite start temperature ( $M_s$ ) and is complete at the martensite finish temperature ( $M_f$ ). The carbon is trapped in the ferritic BCC-like structure, therefore distorting the BCC crystal structure to a BCT structure. This means that martensite can be viewed as a strained ferrite phase with trapped carbon. The distortion of the BCC matrix to BCT is one of the reasons why martensite is much harder, and therefore more brittle, than ferrite. To sensitise martensite, it must be heated to the carbide precipitation range of ferrite. The carbon escapes from the trapped lattice structure and chromium carbides precipitate. If the sample is then cooled rapidly, it will be sensitised. If a slow cooling rate is allowed, chromium back-diffusion from the grain interiors will heal the sensitised martensite. If the  $M_s$  is high enough and if the cooling rate is not too fast, autotempering of the martensite can occur.

In 3CR12, the maximum amount of austenite that can form is dependent mainly on the chemistry and the cooling rate. An important determining factor in the sensitisation behaviour of the ferritic-martensitic family of duplex stainless steels, of which 3CR12 is a member, is the amount of delta-ferrite that transforms to austenite on cooling [7]. Austenite has a higher solubility for carbon than ferrite, therefore an increase in the fraction austenite present at high temperatures in the carbide precipitation range reduces the tendency for intergranular carbide precipitation from carbon-supersaturated ferrite during cooling, and the steel is less susceptible to intergranular corrosion [6,7,8]. The micrograph shown in Figure 3.2 [7] displays

intergranular attack in the high temperature heat-affected zone of a duplex stainless steel, 3RE60 from Sandvik, which has a low austenite content. Attack is limited to the ferrite-ferrite grain boundaries.

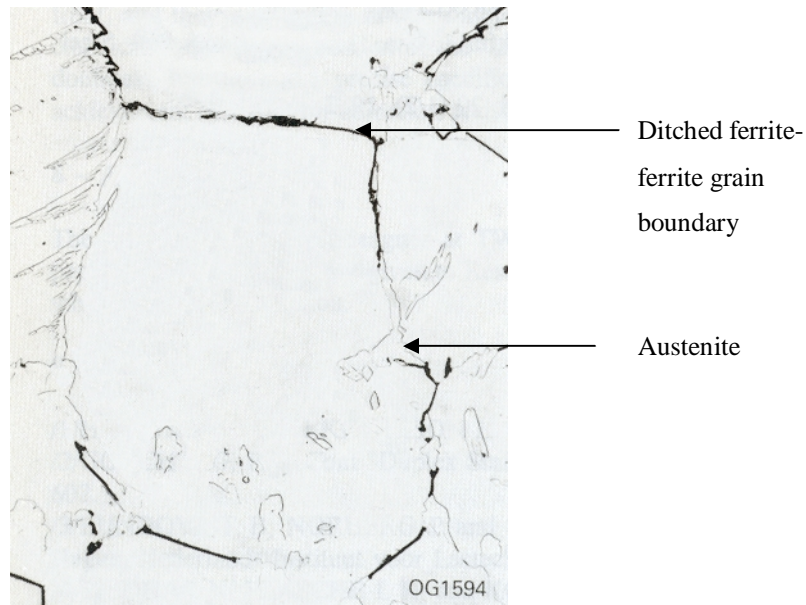


Figure 3.2. Intergranular attack in heat-affected zone of a low austenite content duplex stainless steel. Material 3RE60, welding parameters:  $I=250$  A,  $V= 16V$  and  $n = 140$  m/min. 6 mm plate thickness <sup>[7]</sup>. (500X).

Conversely, if less austenite forms at high temperature the available carbon is increased, which results in more carbide precipitation. If no austenite is present at high temperatures in the carbide precipitation range, extensive carbide precipitation on the ferrite-ferrite grain boundaries can be expected. In practice this can occur if very fast cooling rates suppress the nucleation of austenite on the delta ferrite grain boundaries, resulting in a continuous ferrite-ferrite grain boundary network. These very fast cooling rates also inhibit the back-diffusion of chromium from the grain interiors, resulting in a sensitised ferritic structure after cooling.

As described earlier, 3CR12 is a low carbon ferritic stainless steel designed to pass through the dual-phase  $\alpha + \gamma$  phase area of the Fe-Cr-C phase diagram during heating and cooling (illustrated in Figure 3.3) <sup>[10]</sup>. Even though Figure 3.3 is for a steel with 0.05% C, the same principle generally applies to ferritic steels with more than 0.01 %C: the ferrite phase cannot dissolve the excess carbon present, resulting in the precipitation of carbides on cooling, regardless of the cooling rate. This diagram shows that there is a change in the type of carbide that precipitates as the chromium content of the alloy increases.  $Fe_3C_2$  is the equilibrium carbide at low chromium contents, up to about 3% Cr.  $(Fe,Cr)_7C_3$  appears between 3 and 7 % Cr, and  $(Fe,Cr)_{23}C_6$  appears above 7 %.  $(Fe,Cr)_{23}C_6$  always forms in steels with chromium content between 10.5 and 12 %, such as 3CR12.

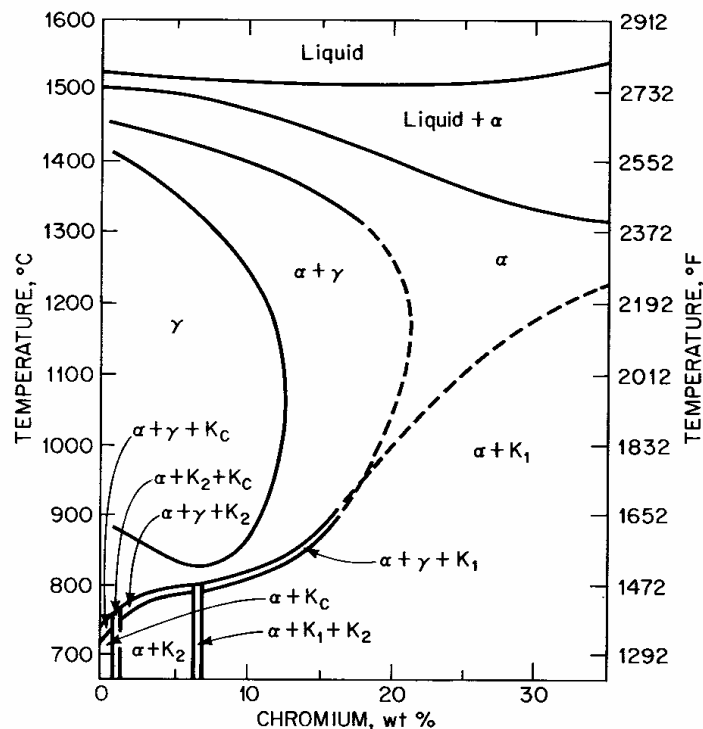


Figure 3.3. Constant section at 0.05 % carbon through the Fe-Cr-C ternary diagram.  $K_c = Fe_3C_2$ ,  $K_1 = (Fe, Cr)_{23}C_6$  and  $K_2 = (Fe, Cr)_7C_3$ .<sup>[10]</sup>

In summary, the kinetics of sensitisation in stainless steel is determined to a large extent by the phase composition of the alloy. Austenite requires slow cooling rates through the susceptible temperature range to sensitise, whereas ferrite sensitises after fast cooling. Martensite needs to be reheated to the ferrite carbide precipitation range, followed by rapid cooling, to sensitise. Therefore, if austenite is cooled down rapidly, and ferrite slowly, neither phase will be in the sensitised condition.

### 3.3. SENSITISATION OF 3CR12

It was initially believed that the dual-phase heat-affected zone microstructure of 3CR12 renders it largely resistant to sensitisation during welding. Duplex ferritic-austenitic stainless steels are known to be more resistant to sensitisation than the austenitic or ferritic grades<sup>[14]</sup>. A model for the sensitisation of duplex stainless steel, by Devine, is illustrated schematically in Figure 3.4<sup>[9]</sup>. When an  $M_{23}C_6$  carbide forms at an austenite-ferrite phase boundary, austenite contributes very little chromium. Due to the rapid diffusion rate of chromium in ferrite, most of the chromium in the  $M_{23}C_6$  carbide is donated by the ferrite phase, consequently a very wide, but shallow, chromium depleted zone forms on the ferrite side of the interface. On the austenite side of the interface, a deep, but very narrow, chromium depleted zone forms. This zone is responsible for the sensitisation of the alloy, but since it is so narrow, chromium diffusion from the interior

of the austenite grain occurs, resulting in healing. Chromium back-diffusion on the ferritic side occurs even more rapidly, resulting in structures that are generally not susceptible to intergranular corrosion <sup>[7,8]</sup>.

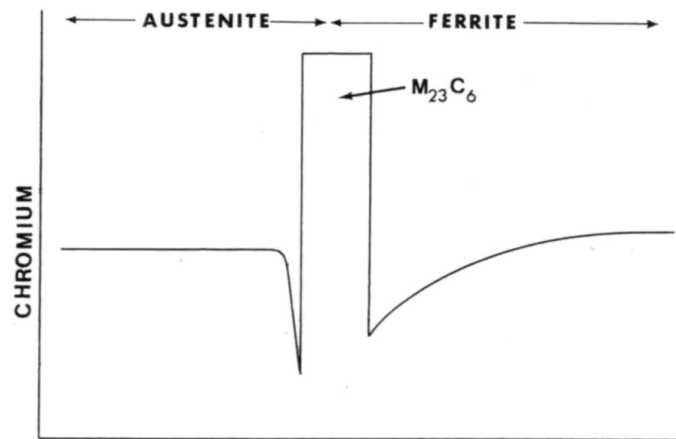


Figure 3.4. Schematic chromium concentration profile at an austenite-ferrite interface containing  $M_{23}C_6$ . <sup>[9]</sup>

A number of recent in-service failures of 3CR12 welds were, however, found to be due to stress corrosion cracking caused by chromium depletion and sensitisation during welding. This prompted a series of studies aiming to identify the mechanisms of chromium depletion and sensitisation in 3CR12. Three possible ways of sensitising 3CR12 have been identified to date and are considered in more detail below.

### 3.3.1. Isothermal sensitisation

Isothermal sensitisation of 3CR12 results in sensitisation of the ferrite-martensite phase boundaries. If the as-supplied material, in its fully healed ferritic condition with the majority of the carbon trapped as carbides, is heat treated to a temperature within the  $\alpha + \gamma$  phase field above the carbide dissolution range (starting from around 950 °C), the austenite that forms will absorb most of the carbon released as the carbides dissolve. Upon cooling the austenite transforms to martensite, as discussed previously. If this martensite is subsequently heated within the carbide precipitation range (between 550°C to 850°C), chromium-rich carbides will precipitate on the martensite-ferrite grain boundaries, resulting in sensitised martensite. This is illustrated in Figure 3.5 <sup>[5]</sup>. In practice a double heat treatment, or a heat treatment followed by a weld, has been found to cause sensitisation.

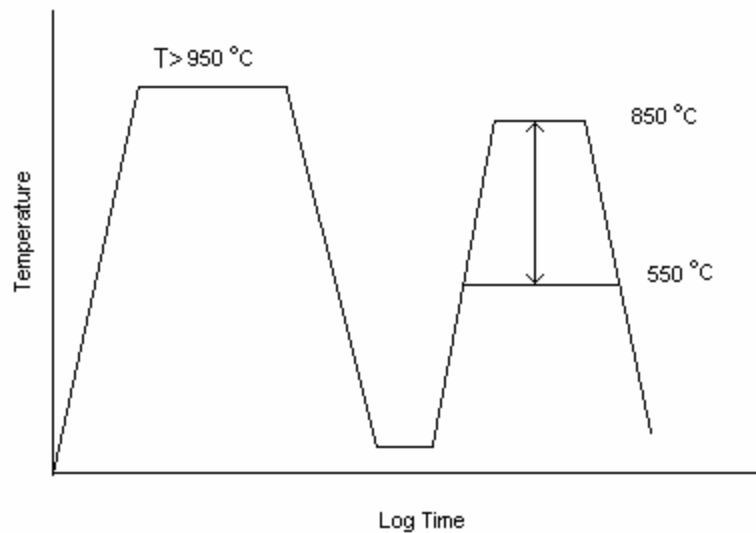


Figure 3.5. Schematic illustration of isothermal sensitisation of martensite in 3CR12. <sup>[5]</sup>

### 3.3.1.1 Double heat treatment

If 3CR12 is heated to a temperature within the  $\alpha + \gamma$  phase field, above the carbide dissolution temperature (in the region of 950°C) and quenched, followed by a second heat treatment between 550°C and 850°C for a sufficient period of time (shown schematically in Figure 3.5), carbide precipitation would result in sensitisation of the martensite phase. If the time within the carbide precipitation temperature range is sufficiently long, back-diffusion of chromium occurs, resulting in healing.

### 3.3.1.2 Heat treatment above 950 °C followed by welding

If 3CR12 is quenched from a temperature above approximately 950°C, and the steel is welded, the area adjacent to the weld that experiences peak temperatures within the carbide precipitation temperature range of 550°C to 850°C, may become sensitised. Care should be taken during the annealing of 3CR12 that the recommended annealing temperature range is not exceeded, as this can result in sensitisation if the steel is subsequently welded. Annealing is normally carried out at 700°C to 750°C, followed by air-cooling.

### 3.3.2. Overlapping heat-affected zones

This mode of sensitisation requires very specific weld geometry of overlapping welds, or parallel welds spaced at a very specific intervals. It is illustrated schematically in Figure 3.6 <sup>[5]</sup>. During the first weld the carbon is taken into solution in the austenite where the heat-affected zone achieves temperatures higher than approximately 950 °C. This austenite transforms to the relatively high carbon martensite in the heat-affected zone on cooling. If another weld is aligned in such a way that the martensite formed during the

first weld is subjected to the temperature range where the precipitation of chromium carbides in ferrite occurs, this martensite will become sensitised.

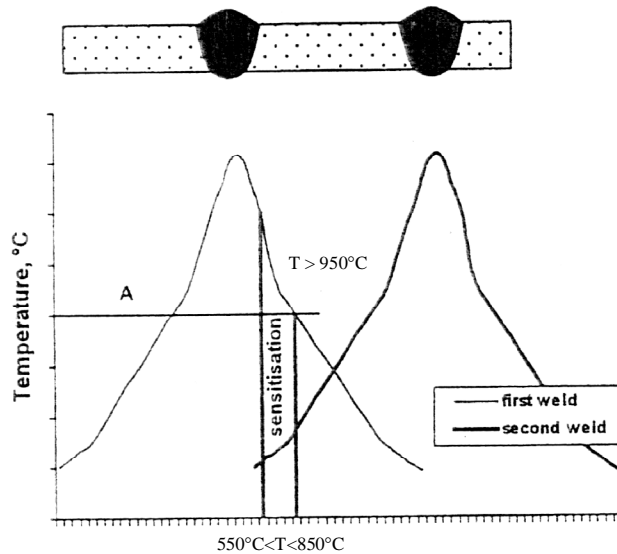


Figure 3.6. Temperature profiles due to overlapping welds, showing the position where sensitisation is possible.

### 3.4. CONTINUOUS COOLING SENSITISATION

Sensitisation of correctly heat-treated and annealed 3CR12 during continuous cooling after welding in the absence of prior heating to temperatures greater than 950°C or overlapping heat-affected zones has also been observed. This mode of sensitisation is associated with either very high heat inputs, or very low heat inputs. Sensitisation during high heat input welding is the subject of a separate investigation and will not be considered further here. Sensitisation at low heat inputs is the subject of this investigation, and the remainder of this discussion and the following chapters will therefore focus on this phenomenon.

From the heat input and Rosenthal's heat flow equations discussed in Chapter 2, it was noted that the cooling time is directly proportional to the square of the heat input, rewritten in Equation 3.1 for thin plate (two-dimensional heat flow):

$$\Delta t_{8-5} \propto (q / v)^2 \quad (3.1)$$

The cooling rate, CR, after welding is therefore proportional to the inverse of the heat input squared, as shown in Equation 3.2:

$$CR \propto \frac{1}{(q/v)^2} \quad (3.2)$$

This implies that low heat inputs and/or fast travel speeds result in rapid cooling after welding.

The continuous cooling sensitisation of 3CR12 is strongly dependent on the cooling rate. It is postulated that the very rapid cooling rate associated with low heat input welding suppresses austenite formation during cooling in such a way that almost fully ferritic heat-affected zones can be obtained. This results in carbon supersaturation of the ferrite. When the ferrite cools down rapidly through the carbide precipitation temperature range, carbides precipitate, but little or no chromium back-diffusion has the opportunity to occur, resulting in a continuous network of sensitised ferrite-ferrite grain boundaries.

In order to study this phenomenon, 3CR12 needs to be welded in such a way that very fast cooling rates are obtained. This can be achieved by welding at very low heat inputs and at high welding speeds. The following chapter describes the experimental procedure used in this investigation to produce and test such welds.

3.5. REFERENCES

1. Číhal, V. Intergranular Corrosion of Steels and Alloys. Material Science Monographs, 18. Elsevier. 1984. pp. 79 – 83
2. Peckner, P. and Bernstein, I. M. Handbook of Stainless Steel. McGraw-Hill Book Company. 1977. p. 5-15
3. Frankenthal, R.P. and Pickering, H. W. Intergranular Corrosion of Ferritic Stainless Steel. Journal of the Electrochemical Society. January 1973. pp. 23 – 26.
4. Sheir, L. L. Ed., Corrosion Volume 1. Metal/Environment Reactions. Newnes-Butterworths. pp. 3:45 – 3:48.
5. Matthews, L. M., Griesel, B., Longman, P. T., Van Rooyen, G. T. and Prozzi, J. M. Sensitisation in low-carbon 12% chromium containing stainless steels. INFACON Proceedings. p. 332.
6. Lula, R. A. and Davis, J. A. Intergranular corrosion in 12% chromium ferritic stainless steels. Intergranular Corrosion of Stainless Alloys, ASTM STP 656, R. F. Steigerwald, Ed., American Society for Testing and Materials 1978, pp. 233-247.
7. Gooch, T.G. Corrosion resistance of welds in duplex stainless steels. Figure 2. Volume 1. Duplex Stainless Steel '91. 28 – 30 October 1991. Beaunne, Bourgogne, France. Les Editions de Physique. pp. 325 – 346.
8. Bernharsson, S. The corrosion resistance of duplex stainless steel. Volume 1. Duplex Stainless Steel '91. 28 – 30 October 1991. Beaunne, Bourgogne, France. Les Editions de Physique. . pp. 185 – 210
9. Solomon, H.D. and Devine, T. M. Duplex stainless steels – A tale of two phases. Conference Proceedings. Edited by R. A. Lula. American Society for Metals. 1983. pp. 693 – 756
10. Peckner, P. and Bernstein, I. M. Handbook of Stainless Steel. McGraw-Hill Book Company. 1977. p. 6-4.
11. Peckner, P. and Bernstein, I. M. Handbook of Stainless Steel. McGraw-Hill Book Company. 1977. p. 6-4.

12. Simmons, J.W., Atteridge, D. G. and Bruemmer, S.M. Continuous cooling sensitisation of Type 316 Austenitic Stainless Steel. *Corrosion* Vol. 48, no. 12, pp.976 – 982.
13. Solomon, H.D. Influence of Prior Deformation and Composition on Continuous Cooling Sensitisation of AISI 304 Stainless Steel. *Corrosion* Vol. 41, no. 9, pp. 512 – 517.
14. Číhal, V. Intergranular Corrosion of Steels and Alloys. *Material Science Monographs*, 18. Elsevier. 1984. p. 242 - 245.
15. Folkhard, E. *Welding metallurgy of Stainless Steels*. Springer-Verlag. 1988. p. 50.

## CHAPTER 4

**EXPERIMENTAL PROCEDURE**

This chapter describes the experimental plan designed during the course of this investigation to evaluate the influence of welding at low heat input levels on the heat-affected zone microstructure and sensitisation resistance of 3CR12 welds.

## 4.1. ALLOYS INVESTIGATED

Two grades of 3CR12 were supplied by Columbus Stainless in the form of 3 mm plate. The chemical compositions of both grades are given in Table 4.1. Also shown in Table 4.1 is the Kalthausser ferrite factor <sup>[1]</sup> (calculated from equation 4.1) that is used to quantify the ratio of ferrite- to austenite-forming elements in the steel.

*Table 4.1. The chemical compositions of the two grades of 3CR12 used for this investigation. (Balance Fe, percentage by mass).*

<b>Heat number</b>	328723	330011
<b>Grade</b>	<b>41220</b>	<b>41311</b>
<b>Designation used in this investigation</b>	<b>A</b>	<b>B</b>
<b>C</b>	0.018	0.012
<b>Mn</b>	0.56	0.49
<b>Cr</b>	11.61	11.57
<b>Si</b>	0.70	0.38
<b>Ti</b>	0.032	0.140
<b>Ni</b>	0.33	0.55
<b>N</b>	0.0213	0.0177
<b>Kalthausser ferrite factor</b>	12.10	9.64
<b>Ti/(C+N)</b>	0.814	4.714

$$\text{Kalthausser ferrite factor} = \text{Cr} + 6\text{Si} + 8\text{Ti} + 4\text{Mo} + 2\text{Al} - 40(\text{C} + \text{N}) - 2\text{Mn} - 4\text{Ni} \quad (4.1)$$

The choice of the two grades was determined by their respective chemistries: 41220 has a higher ferrite factor than 41311. A higher ferrite factor indicates that the steel has higher ratio of ferrite-to-austenite-forming elements, where the ferrite-forming elements promote ferrite at the expense of austenite within the gamma loop temperature range. Grade 41220's higher ferrite factor predicts that less austenite will form in the high temperature heat-affected zone during welding.

4.2. EXPERIMENTAL PLAN

The general experimental plan is outlined in Figure 4.1. Welds were evaluated for sensitisation using Practice Z and Practice W of ASTM 763-99, *Standard Practices for Detecting Susceptibility to Intergranular Attack in Ferritic Stainless Steels*, as well as a potentiostatic etch. Practice Z indicates embrittlement due to chromium depletion and sensitisation, Practice W tests for the presence of chromium carbides and the potentiostatic etch highlights chromium depletion. Each aspect of the experimental plan is discussed in detail in the remainder of this chapter.

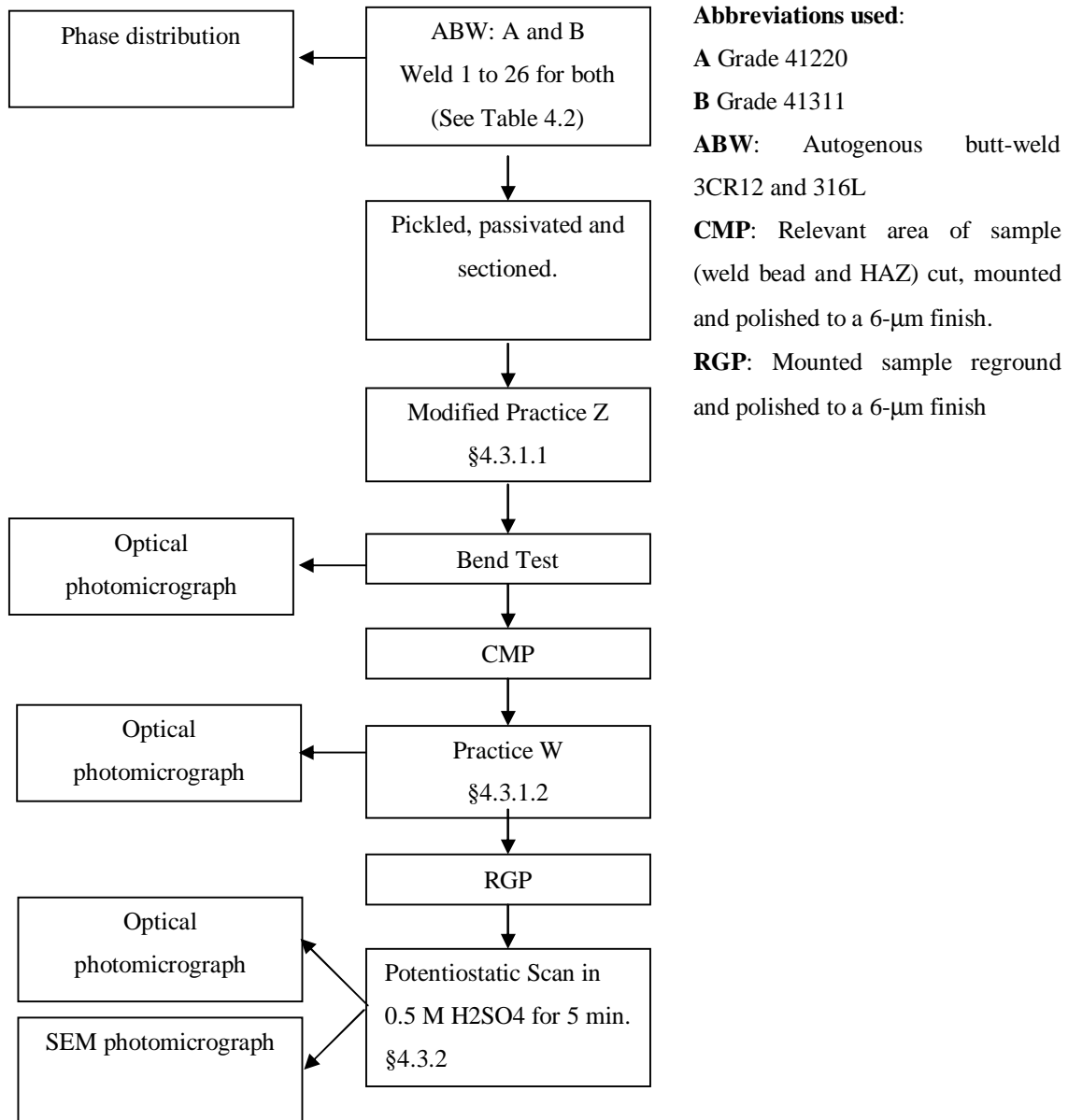


Figure 4.1. Experimental plan prepared for this investigation.

#### 4.3. MATERIAL HOMOGENISATION

The different steel samples supplied by Columbus Stainless were removed from the front and tail ends of coils. In order to ensure a homogeneous microstructure and chromium concentration in all the samples prior to welding, the plates were heat treated, after sectioning, in a furnace at 700 °C for an hour. The temperature of the samples was monitored with a thermocouple that was in contact with the centre plate. Figure 4.2 shows the configuration. After an hour, the furnace was switched off and the samples were allowed to cool. The slight scale that formed during homogenisation was subsequently removed by sandblasting.

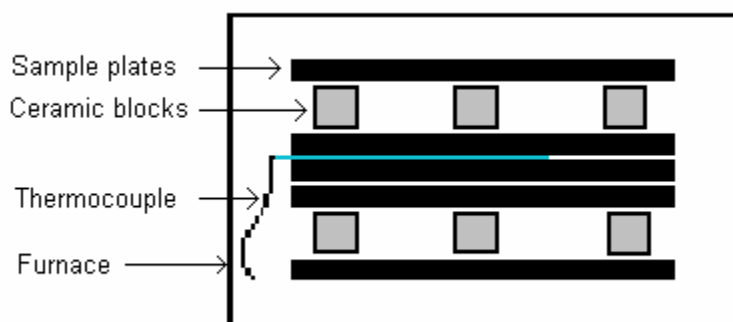


Figure 4.2. The configuration of the plates during homogenisation heat treatment.

#### 4.4. WELDING

In order to evaluate the influence of welding parameters on the microstructure and sensitisation resistance of 3CR12, ten different heat inputs were selected. The lower heat input welds, from 70 J/mm to 500 J/mm, were produced at three welding speeds: a very fast welding speed of 2 m/min (33.3 mm/s), a fast welding speed of 1 m/min (16.7 mm/s), and a normal welding speed of 0.3 m/min (5 mm/s). The higher heat input welds were made at two welding speeds, 0.3 m/min (5 mm/s) and 0.1 m/min (1.67 mm/s). The influence of higher welding speeds at high heat input levels could not be investigated, since the welding power source could not deliver the high welding currents required.

The heat input equation, discussed in Chapter 2, was used to calculate the necessary welding parameters to produce the required heat input levels. The welding parameters and heat inputs used in this investigation are shown in Table 4.2. Initial testing of bead-on-plate welds performed at 100 J/mm and 500 J/mm revealed that all welds performed at 100 J/mm suffered extensive corrosive attack of the weld bead and part of the heat-affected zone during the boiling acid test, Practice Z, and those produced at 500 J/mm showed intergranular corrosion of the weld bead, as well as attack at various locations in the heat-affected zone.

Active dissolution of the weld bead complicated the interpretation of the bend test results after the boiling test (see §4.3.1). The weld had to be made more noble to restrict attack to the sensitised high temperature heat-affected zone, but the addition of filler metal was impractical at the low heat inputs and fast welding speeds used.

Table 4.2. Calculated welding parameters used in this investigation.

Weld number	Welding Current	Arc Voltage	Welding Speed	Welding Speed	Calculated heat input	Actual heat input
	(A)	(V)	(mm/s)	(m/min)	(J/mm)	(J/mm)
1	167	14	33.33	2	70.1	33.5
2	97	12	16.67	1	69.8	33.3
3	44	8	5	0.3	70.4	33.6
4	222	15	33.33	2	99.9	47.7
5	128	13	16.67	1	99.8	47.7
6	50	10	5	0.3	100.0	47.8
7	317	21	33.33	2	199.7	95.4
8	208	16	16.67	1	199.6	95.3
9	91	11	5	0.3	200.2	95.6
10	263	19	16.67	1	299.8	143.2
11	167	15	8.33	0.5	300.7	143.6
12	125	12	5	0.3	300.0	143.3
13	259	18	11.67	0.7	399.5	190.8
14	208	16	8.33	0.5	399.5	190.8
15	143	14	5	0.3	400.4	191.2
16	231	18	8.33	0.5	499.2	238.4
17	167	15	5	0.3	501.0	239.3
18	83	10	1.67	0.1	497.0	237.4
19	200	15	5	0.3	600.0	286.6
20	91	11	1.67	0.1	599.4	286.3
21	219	16	5	0.3	700.8	334.7
22	106	11	1.67	0.1	698.2	333.5
23	235	17	5	0.3	799.0	381.6
24	111	12	1.67	0.1	797.6	380.9
25	250	18	5	0.3	900.0	429.8
26	125	12	1.67	0.1	898.2	429.0

It was subsequently decided to autogenously join 3CR12 to AISI 316L so that a passive weld bead could be obtained. This resulted in a more noble weld bead consisting of an admixture of 3CR12 and 316L, which allowed the study of the sensitised heat-affected zone. All twenty-six welds at different welding parameters and heat inputs, see Table 4.2, were performed in this way, with the results discussed in Chapter 5. The set-up used to perform the welds is shown schematically in Figure 4.3.

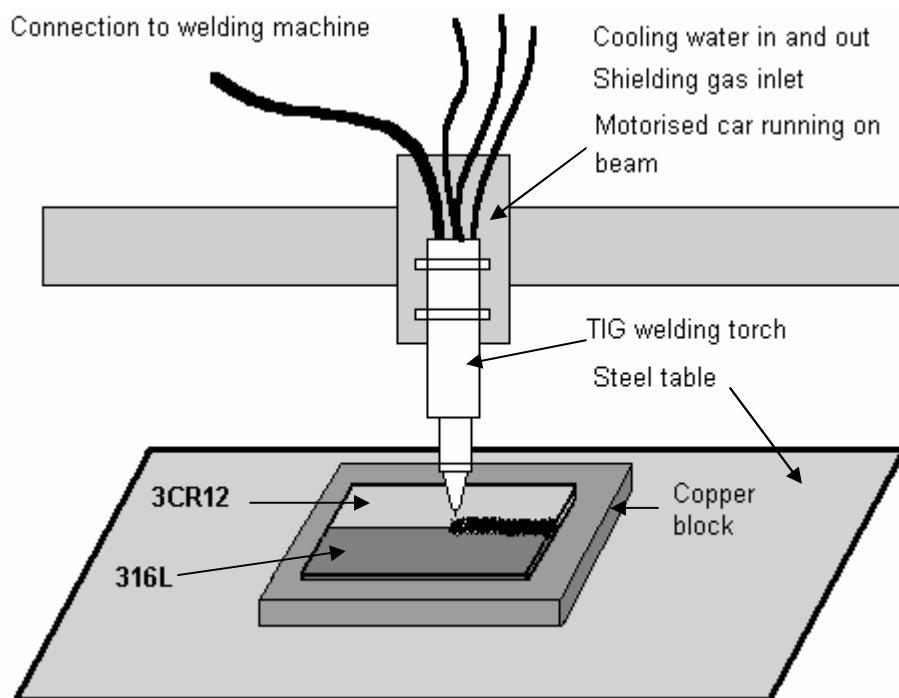


Figure 4.3. Schematic representation of GTAW experimental set-up used for welding.

Gas tungsten arc welding was used to perform the welds. A dial was used to select the welding current, and the arc voltage was measured across the arc gap during welding. Electrode negative polarity and argon shielding gas was used. The travel speed was controlled automatically using a motorised carriage mounted on a horizontal beam.

The welds were pickled and passivated with a 1 – 2% HF and a 20 – 30 %  $\text{NH}_3\text{OH}$  commercial passivating paste. This was done to remove the high temperature oxides formed during welding, and to reform the protective passive layer. High temperature oxides do not form an adherent passive layer and could reduce the corrosion resistance of the samples during the boiling acid test. Samples were sectioned from each weld after pickling and passivation, and subjected to the sensitisation tests.

#### 4.5. SENSITISATION TESTING

Sensitisation due to carbide precipitation and chromium depletion in the high temperature heat-affected zone of 3CR12 can be detected through the use of a bend test after immersion in a boiling test solution, through microscopic evaluation after electrolytic etching, or through a potentiostatic etch designed to reveal chromium depletion. Each of these tests are considered in more detail below.

##### 4.5.1. ASTM A 763-93

Evaluation of the welds for sensitisation was done using ASTM standard A 763 – 93 (Re-approved 1999). Two of the tests are applicable to 3CR12: Practice W, the 10% oxalic acid electrolytic etch that detects the presence of chromium carbides, and a modified Practice Z boiling acid test, that detects embrittlement due to sensitisation and chromium depletion.

##### 4.5.1.1 Practice Z

Practice Z is a copper-copper sulfate-16% sulphuric acid boiling immersion test for detecting the susceptibility of ferritic stainless steel to intergranular attack. Evaluation by bending is preferred for welds, since mass loss of different welds at a range of heat inputs would not be comparable. Bending reveals embrittlement of the weld and heat-affected zone due to chromium depletion at the grain boundaries. The experimental set-up used is shown schematically in Figure 4.4.

The standard sensitisation tests are too aggressive for 11 – 12 % chromium stainless steels<sup>[5]</sup>, therefore a modification was proposed. The acid concentration was reduced from 16% to 6%, and the boiling time from 24 hrs to 15 hrs. This modification was used in the current investigation. A 3000 ml corrosion cell was used. Copper shavings were used to cover each sample submerged in the test solution. The copper shavings were reused after cleaning with 30% nitric acid solution and rinsing with clean water. A reflux condenser was used to maintain volume and concentration during the duration of the test.

Sample volume was such that the volume of solution was approximately 15 cm<sup>3</sup> per 1 cm<sup>2</sup> sample area.

The specified bend test requires the sample to be bent through 180° over a radius equal to twice the thickness of the specimen. For 3 mm plate, this suggests a 12 mm diameter mandrel. The bend test is schematically illustrated in Figure 4.5. A solid steel block was used for the base, and was machined to give a profile shown in the figure, with a gap width of 20 mm. The base and mandrel assisted in performing the bend test, as shown. A hydraulic press was used to apply the pressure that resulted in either a bent or a fractured weld. Samples containing the weld, the heat-affected zone and some parent material were

sectioned from the bend test samples. These were mounted in cross section in resin and polished to a 6  $\mu\text{m}$  finish. The polished samples were then etched electrolytically in a 10% oxalic acid solution (Practice W) to reveal any chromium carbides present.

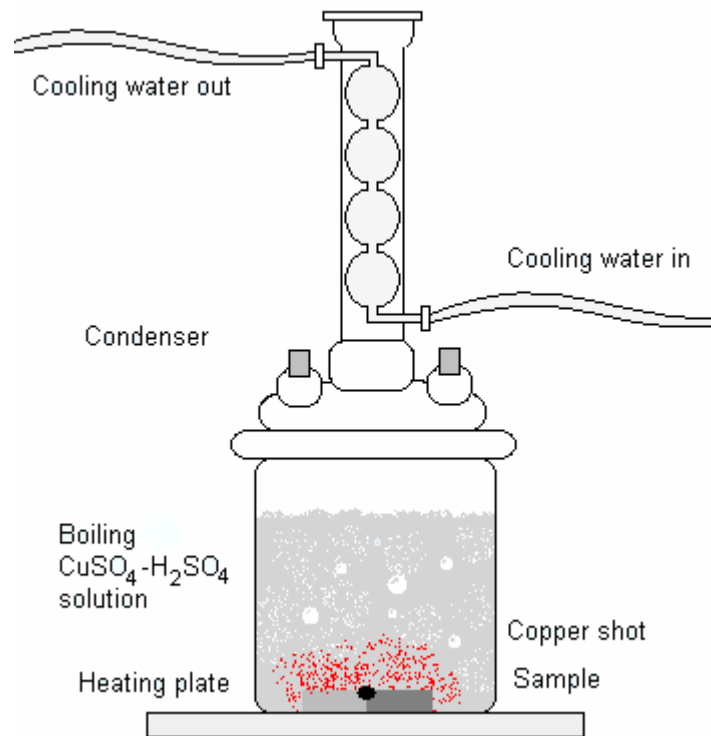


Figure 4.4. Schematic representation of Practice Z experimental set-up used in this investigation.

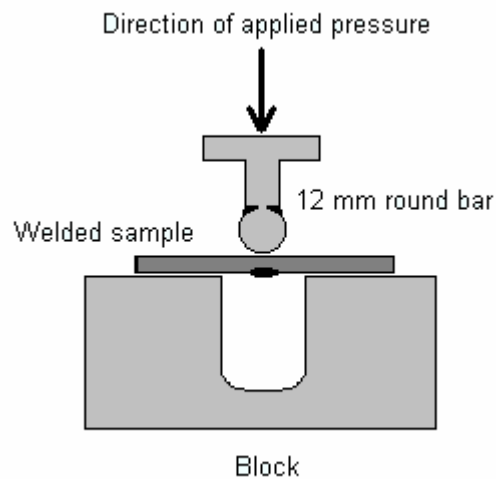


Figure 4.5. The schematic representation of the bend test configuration that was used to evaluate the welds after immersion in the modified Practice Z boiling acid test solution.

## 4.5.1.2. Practice W

The electrolytic oxalic acid etch attacks chromium carbides, and is used as a screening test to classify structures as sensitised or potentially sensitised. In this investigation it was used to highlight the position of any chromium carbides in the heat-affected zone. Electrolytic etching was performed at  $1 \text{ A/cm}^2$  for 60 seconds in a saturated oxalic acid solution. Etched samples were examined microscopically, and classified.

The presence of chromium carbides cannot be used to verify that the structure is sensitised, since a healed structure will also contain carbides, and susceptibility has to be confirmed with additional test(s).

The test set-up that was used is illustrated in Figure 4.6. A stainless steel bowl was used as the cathode and a stainless steel rod was brought in electric contact with the specific mounted weld cross section for the specified time, making it anodic. The specified current density was obtained by applying a potential, in the transpassive range between 4 and 6 V, where the chromium carbide particles, if present, actively dissolve, leaving a continuous ditched structure in susceptible samples. The absence of a continuous ditched grain boundary structure indicates that the sample is not sensitised.

Optical photomicrographs were taken of each weld after this test.

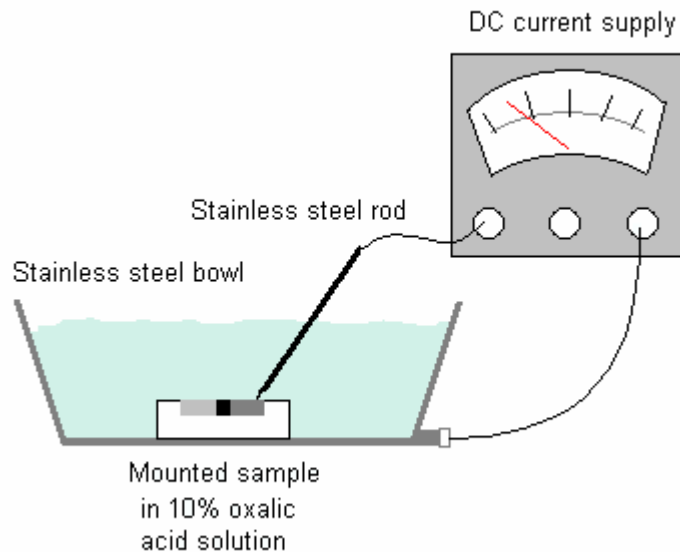


Figure 4.6. Schematic representation of the Practice W experimental set-up used in this investigation.

#### 4.5.2. Potentiostatic chromium depletion test

Difficulties in interpreting the results of the Strauss test (to be described in Chapter 5) necessitated the use of a potentiostatic chromium depletion test to verify the results of the oxalic acid etch. The passivation potential of a chromium containing steel changes with chromium content, as shown in Figure 4.7<sup>[3]</sup>.

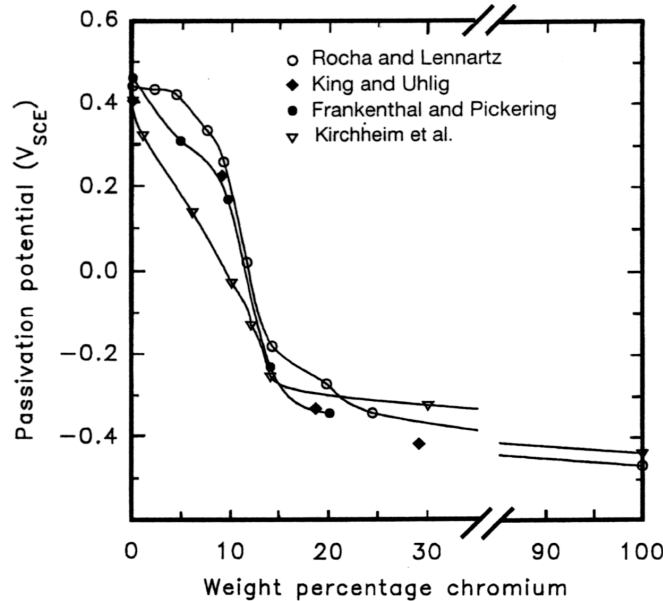


Figure 4.7. Passivation potential of binary iron-chromium alloys in 0.5 M H<sub>2</sub>SO<sub>4</sub> at room temperature relative to the saturated calomel electrode.<sup>[3]</sup>

Chromium depletion can be verified by controlling the potential at 0 V<sub>SCE</sub> in a 0.5 M H<sub>2</sub>SO<sub>4</sub> solution. At this potential, areas with 10 % chromium or more will be passive, whereas those areas with less than 10% chromium will be active and will dissolve. Any chromium-depleted regions will therefore dissolve preferentially.

Welds of both grades of 3CR12 were chosen after Practice W to undergo the potentiostatic corrosion test. The lower heat input welds, more likely to be sensitised (welds 1 to 15 in Table 4.2) of both grades were evaluated to ascertain the extent of sensitisation. After the first round of tests, it was decided to include samples 16 to 18 from grade 41220 (A). Weld 26 was included as a reference sample, since it was unlikely to be sensitised (as found during Practice W evaluation).

The sample was brought in contact with the 0.5M H<sub>2</sub>SO<sub>4</sub> solution and the potential was held at 0 V<sub>SCE</sub> for 300 seconds. This time was sufficient for the current to stabilise. Samples were evaluated optically and photomicrographs were recorded. Selected samples were also examined using a scanning electron microscope (SEM).

#### 4.6. PHASE DISTRIBUTION DETERMINATION

In order to illustrate the influence of cooling rate, welding speed and heat input on the phase distribution and subsequent sensitisation behaviour of the material, the martensite content of the high temperature heat-affected zone was estimated.

Four photomicrographs at 500X magnification were taken at random of each weld's high temperature heat-affected zone. Such a high magnification was required since the high temperature heat-affected zone, where sensitisation was thought to occur, was very narrow in the low heat input welds. This magnification was also used for the higher heat input welds so that the photomicrographs would be comparable.

Image analysis of the photomicrographs proved troublesome. The 10% oxalic acid etch was used to distinguish the ferrite from the martensite, since the phase boundaries were well defined. This etching technique highlighted texture differences between the ferrite and martensite, but consistent colour contrast, suitable for image analysis, could not be obtained. Etching with a modified Kalings no. 2 solution did not give consistent colour contrast results and clear distinction of the grain boundaries. It was therefore decided to use the manual point counting method to estimate the martensite content of the high temperature heat-affected zone of the welds.

Three methods were used in the evaluation. The first method used a grid of four lines intersecting in four points (called Test 1) <sup>[3]</sup>, the second used a grid with 215 points (called Test 2), and the third used a set of 49 random points (Test 3).

A point or line intersection falls either inside a martensite particle (counted as one), on a ferrite-martensite grain boundary (counted as a half), or inside a ferrite grain (counted as zero).

During Test 1, the grid with its four points was moved at random, and twenty counts were made on each photomicrograph. This resulted in a number out of a possible maximum of 80, which was used to calculate the percentage martensite for that photomicrograph.

With Test 2 the grid was placed on the photomicrograph and two different colour whiteboard markers were used to mark those cross hairs that fell in a martensite grain or on a martensite-ferrite grain boundary. One count per photomicrograph was made.

During Test 3, the grid with its 49 random points was moved randomly and ten counts per photomicrograph were made, resulting in a number out of a maximum of 490.

Test 1 was the easiest to perform on the higher martensite content heat-affected zones (20 to 50% martensite), since only four points required counting. Test 2 and 3 worked well on the low martensite content welds (1% to 20%), but proved somewhat cumbersome with the high martensite content welds.

All three tests were used at least once on the same weld and since repeatable results were obtained ( $\pm 5\%$  for martensite contents greater than 20%), it was decided to use Test 1 for the higher martensite samples. For grade 41220 this included welds 17 to 26, and for 41311 welds 10 to 26 (see Table 4.2). For lower martensite content high temperature heat-affected zones, Test 2 proved the most efficient.

It must be emphasised that this evaluation yields an *estimate* of the martensite content. This was used to illustrate the principle that high welding speeds and lower heat inputs cause faster cooling rates that suppress austenite nucleation, producing less martensite in the heat-affected zone. A more complete analysis for greater accuracy, especially in view of the fact that the range of heat inputs used resulted in significant variance in the size of the heat-affected zone, phase distribution and grain size, would not have added to the underlying principle that was clearly supported by the photomicrographs.

4.7. REFERENCES

1. Kalthausser, R. H *Improving the Engineering Properties of Stainless Steels*. Source book on the Ferritic Stainless Steel, pp. 212 - 218. ASM Engineering Bookshelf. 1982.
2. ASTM standard A 763 – 93 (Reapproved 1999). *Standard Practices for Detecting Susceptibility to Intergranular Attack in Ferritic Stainless Steels*
3. Pistorius, P.C and Coetzee, M. *Sensitisation of 430 ferritic stainless steel during continuous annealing*. The Journal of the South African Institute of Mining and Metallurgy. Vol. 96, no.3. pp. 119 - 125. 1996.
4. Higginson, R.L. and Sellars, C.M. Worked examples in Quantitative Metallography. p. 19 – 25. IOM<sup>3</sup>. Maney Publishing. 2003
5. Devine, T.M. and Drummond, B.J. An Accelerated Intergranular Corrosion Test for Detecting Sensitisation in Low Chromium Ferritic Stainless Steels. Corrosion. Vol. 38, no. 6. pp. 327 – 330. NACE 1982.

## CHAPTER 5

### RESULTS AND DISCUSSION

Chapter 4 described the experimental plan designed to test the sensitisation behaviour of low heat input 3CR12 welds. This chapter considers the results obtained.

#### 5.1. MODIFIED EXPERIMENTAL PLAN

The original experimental plan given in Figure 4.1 had to be modified during the course of the investigation. Certain samples, generally the low heat input welds (1 to 15 in Tables B.1 and B.3 in Appendix B), suffered aggressive attack in the heat-affected zone during the boiling acid test that hampered evaluation of the microstructure. For this reason a number of autogenous bead-on-plate welds of both grades were produced (in addition to the butt welds described in Chapter 4) to facilitate microstructural assessment. This modified experimental plan is shown schematically in Figure 5.1.

#### 5.2. WELDING

Two 3CR12 chemistries, designated 41220 and 41311 (with compositions as shown in Table 4.1), were welded using a range of heat inputs and welding speeds. Grade 41311 has a higher austenite potential than grade 41220, and is therefore expected to have a higher martensite content in the high temperature heat-affected zone at the same welding parameters.

In order to confine attack during the boiling acid test to the heat-affected zone (rather than the weld metal), 3CR12 and 316L were joined autogenously, as described in Chapter 4. These welds were subjected to the boiling Cu-CuSO<sub>4</sub>-6% H<sub>2</sub>SO<sub>4</sub> test, followed by bending. Samples were cut, mounted and polished to a 6 µm finish before evaluation with Practice W (the 10% oxalic acid etch). Following microstructural evaluation, these samples were reground and prepared for the 0.5 M H<sub>2</sub>SO<sub>4</sub> potentiostatic etch. Optical photomicrographs of all the welds were taken at each of these stages and selected samples were assessed with a scanning electron microscope.

During the boiling acid test, a number of the low heat input welds (1 to 15) suffered aggressive attack in the high temperature heat-affected zone that complicated microstructural analysis. These welds were therefore repeated as autogenous bead-on-plate welds, and subjected to Practice W in order to facilitate evaluation of the high temperature heat-affected zone microstructure. All the welding parameters used are given in Tables B.1 to B.4 in Appendix B.

The autogenous bead-on-plate welds (1 to 15) were welded at slightly different welding parameters, since it proved difficult to obtain exactly the same welding speed as the earlier welds.

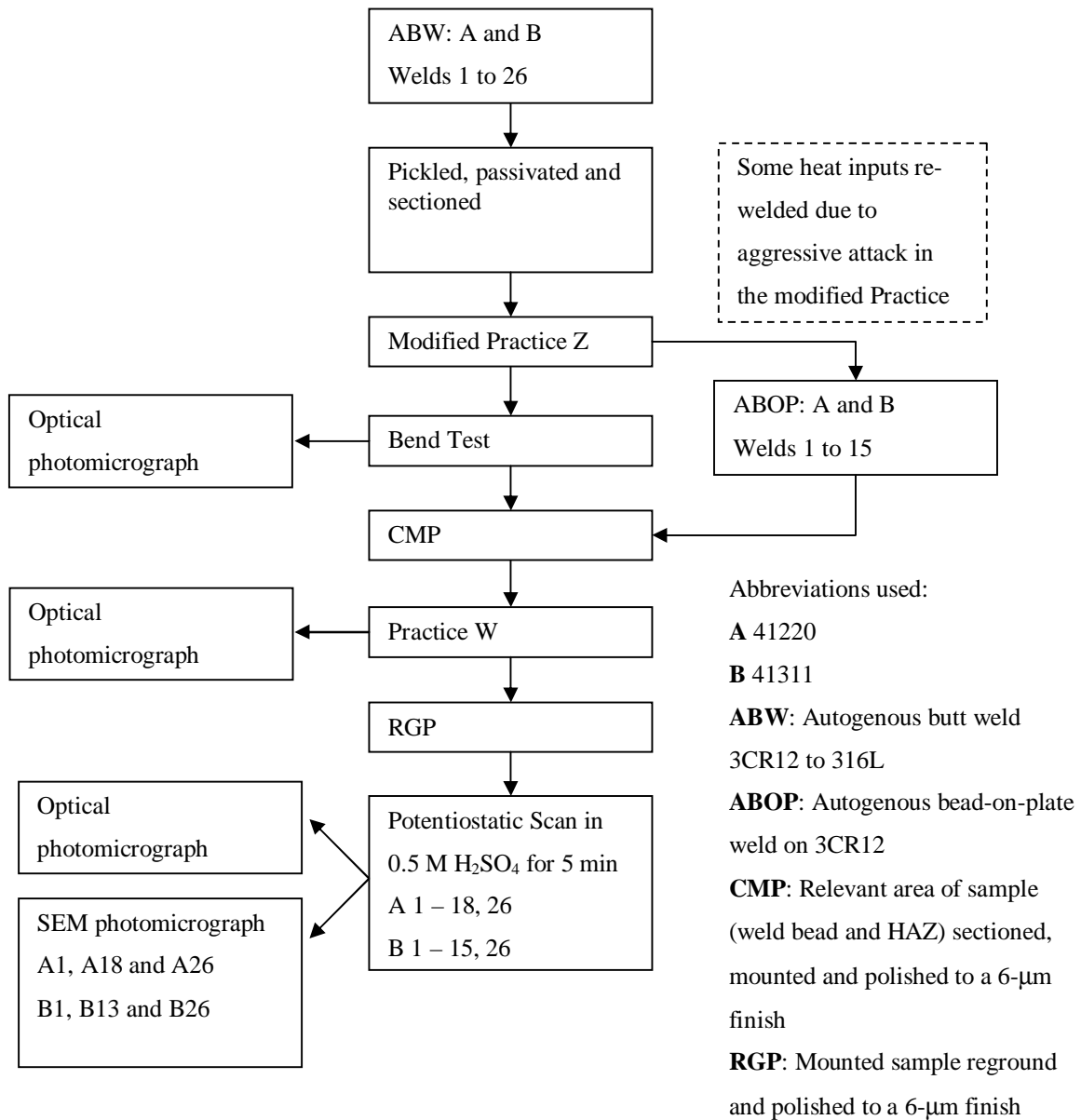


Figure 5.1. Modified experimental plan. Welding parameters are shown in Tables B.1 to B.4 in Appendix B.

## 5.3. PHASE DETERMINATION

## 5.3.1. Results and Discussion

In order to quantify the influence of welding speed and heat input on the heat-affected zone microstructure of the two 3CR12 alloys, point counting, described in Chapter 4, was used to estimate the amount of martensite in the region of the high temperature heat-affected zone of each weld. The results are tabulated in Appendix B in Tables B.6 and B.7. Also given in these tables is the actual power  $q$  (W) delivered to the work piece after the calculated arc efficiency (from Chapter 2) was taken into account. The calculated cooling rate, the travel speed and cooling time from 1500°C to 800°C are also included.

The estimated martensite content, with the calculated standard deviation, is presented graphically in Figure 5.2 for grades 41220 and 41311. A general trend is apparent for both grades: as the heat input increases, the martensite content also increases.

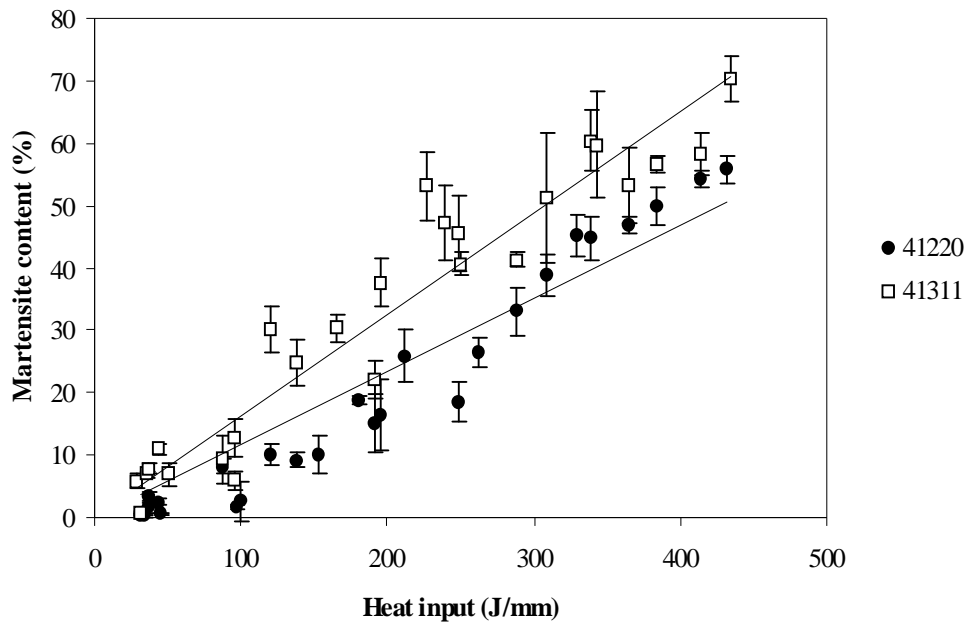


Figure 5.2. The estimated martensite content as a function of the actual heat input with the standard deviation for each determination.

Considerable scatter is evident in the measured martensite content. A clear distinction between the martensite and ferrite phases in the heat-affected zone microstructure proved difficult to obtain. Etchants such as Kallings no. 1 and 2, even diluted with water, did not provide consistent results. The oxalic acid etch worked very well for the low heat input welds of both steels. For the 41220 material, it continued to work well at high heat input levels. In the case of 41311, oxalic acid worked reasonably well at the higher heat input levels, since it showed a difference in texture between the ferrite and martensite, but this difference in texture was less apparent with 41311 than with 41220.

5.4. THE INFLUENCE OF  $q$  AND  $n$  ON THE COOLING RATE

Rosenthal's conduction heat flow model was used to determine the cooling rates of the welds in order to demonstrate the influence of welding parameters on the observed heat-affected zone microstructures.

**5.4.1. Derivation and Calculation**

In order to determine the influence of the welding speed and heat flux or power,  $q$ , on the time taken to cool down from 1500°C to 800°C, Rosenthal's heat flow equation for thin plate is required. Consider Equation 5.1, Rosenthal's two-dimensional heat flow solution for thin plate.

$$T - T_0 = \frac{q}{2Id\sqrt{pvr/a}} \exp\left(-\frac{v(x+r)}{2a}\right) \quad (5.1)$$

where:  $T$  is the temperature at a radial distance  $r$  from the heat source (K),

$T_0$  is the original temperature of the plate prior to welding (K),

$q$  is the work transferred to the plate (W),

$I$  is the thermal conductivity ( $\text{Wm}^{-1}\text{K}^{-1}$  or  $\text{Jm}^{-1}\text{s}^{-1}\text{K}^{-1}$ ),

$v$  is the welding speed ( $\text{ms}^{-1}$ ),

$a$  is the thermal diffusivity ( $\text{m}^2\text{s}^{-1}$ ), where  $a = I/\rho c \text{ m}^2\text{s}^{-1}$ ,

$x$  is the distance from the moving heat source in the  $x$ -direction ( $x > 0$

for points  
source),

in front of the heat source, and  $x < 0$  for points behind the heat

$d$  is the plate thickness, and

$r$  is the radial distance from the heat source where:

$$r = \sqrt{x^2 + y^2 + z^2}$$

Equation 5.1 was used to calculate the thermal cycle experienced by a point on the fusion line of a 3CR12 weld. As a first step, the distance from the weld centre line to the fusion line (i.e. the width of the weld bead) was calculated for each weld. This was done by assuming that  $x = 0$ ,  $y = r$  and  $z = 0$  when the heat source is in line with the point on the fusion line at  $t = 0$  seconds.  $\xi$  values used are given in Table B.5 in Appendix B.

5.4.2. Results

The calculated values of the time taken to cool down from 1500°C to 800°C for grades 41220 and 41311 are given in Appendix B as Tables B.6 and B.7. The heat flux ( $q$ ) is the energy that is supplied to the workpiece at the respective welding speeds, that has taken  $\eta = 0.4776$  into account.

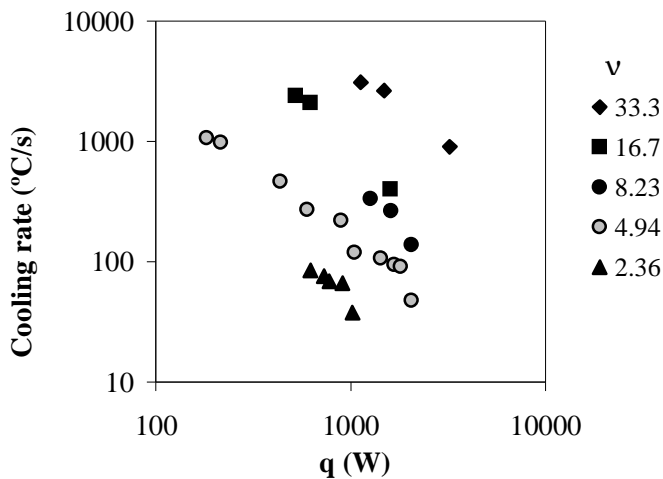


Figure 5.3. The influence of  $q$  and  $n$  on the cooling rate of each weld for Grade 41220

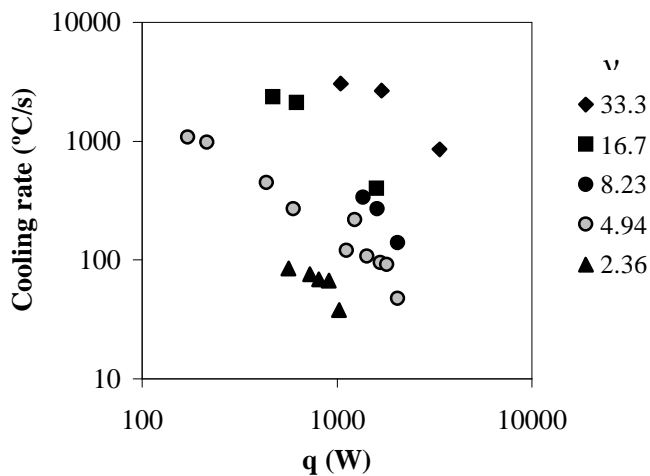


Figure 5.4. The influence of  $q$  and  $n$  on the cooling rate of each weld for Grade 41311

### 5.4.3. Discussion

The time taken to cool down from the liquidus temperature, 1500°C, to 800°C is represented by  $Dt_{15-8}$ . The influence of  $q$  (W) and  $n$  (mm/s), i.e. the welding parameters on  $Dt_{15-8}$  is shown in Figures 5.3 and 5.4. Here, the cooling rates corresponding to five different welding speeds, each with at least three different  $q$  values, are shown graphically. From these two figures it is evident that as the welding speed decreases, the cooling time increases.

## 5.5. THE INFLUENCE OF $q$ AND $v$ ON THE ESTIMATED MARTENSITE CONTENT.

### 5.5.1. Results

The estimated martensite contents for 41220 and 41311 are shown graphically against  $q$  (the fraction of the power of the welding power source that is used for melting), in Figures 5.5 and 5.6. Iso-heat input lines have been drawn in so that different heat inputs at the various welding speeds could be compared.

### 5.5.2. Discussion

The scatter in the results discussed in 5.2.2 is also evident here. The results of 41220 show better linearity than the results of 41311. A general trend can be discerned, even considering the amount of scatter.

Each welding speed has its own slope. The slope of the line decreases as the welding speed increases. This indicates that even at very high  $q$  values, the amount of martensite would increase very slowly. To obtain higher martensite contents, a very large increase in  $q$  is required. At slower welding speeds, a faster increase in the martensite content is obtained as  $q$  increases due to the steeper slope of the lines.

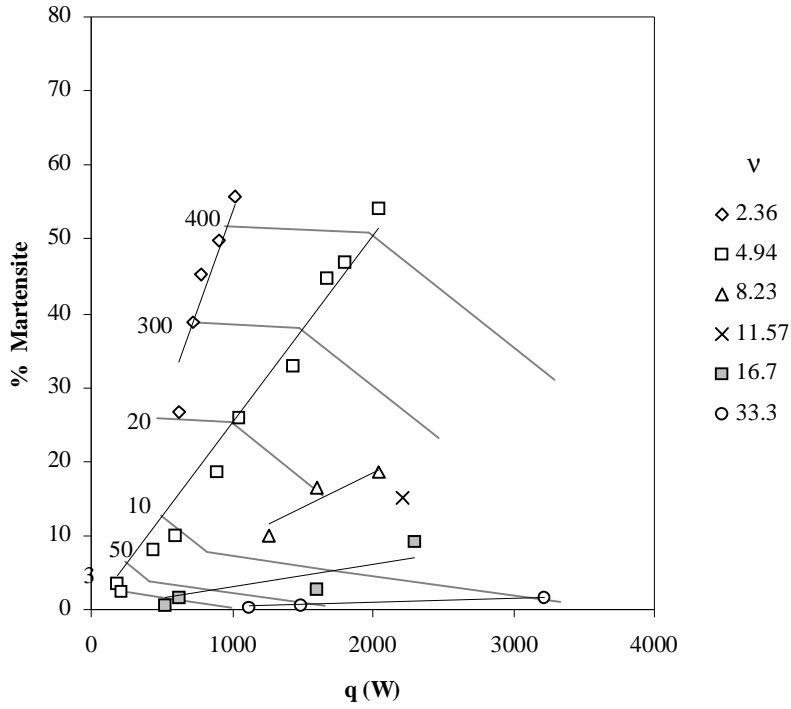


Figure 5.5 Influence of q and v on the estimated martensite content of 41220 welds. Drawn in are the iso-heat input lines.

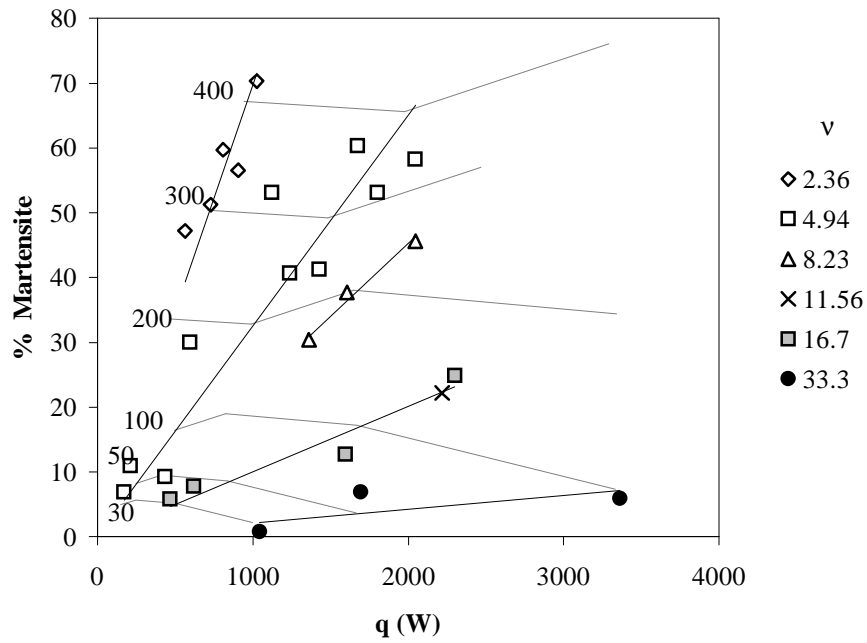


Figure 5.6. Influence of q and v on the estimated martensite content of 41311 welds. Drawn in are the iso-heat input lines

## 5.6. SENSITISATION TESTS

Three tests were used to evaluate the susceptibility of the welds to sensitisation and intergranular attack. All the welds were subjected to the modified Cu-CuSO<sub>4</sub>-6%H<sub>2</sub>SO<sub>4</sub> test to reveal the extent of chromium depletion at the grain boundaries. This test proved to be too aggressive, as will be explained below, and the results were generally unsatisfactory.

The oxalic acid etch (Practice W of ASTM 763-99) attacks chromium carbides, and although it is generally used only as a screening test for possible sensitisation, microstructural examination after etching supplies information on the distribution, amount and location of any carbide particles. The unsatisfactory results obtained during the boiling acid test necessitated the use of a third test to determine whether the carbides observed in the structure resulted in the chromium depletion required for sensitisation. The results from each of these tests are described below.

## 5.6.1. Results

5.6.1.1. Practice Z: Boiling Cu-CuSO<sub>4</sub>-6%H<sub>2</sub>SO<sub>4</sub> test

All the autogenous butt welds were subjected to the modified Practice Z test after pickling and passivation. Three different modes of attack were observed that appear to depend on the heat inputs that were used. These patterns of attack are summarised schematically in Figure 5.7.

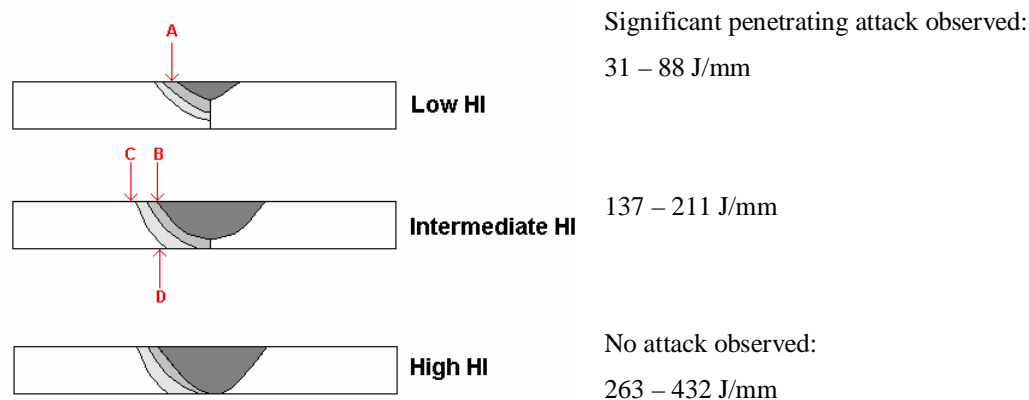


Figure 5.7. A summary of the modes of attack observed after Practice Z for the different groups of welds. No attack was observed in the high heat inputs welds.

The mode of attack in the high temperature heat-affected zone of the low heat input welds (33 to 88 J/mm) appeared to be intergranular, associated with severe grain drooping. This is depicted by A in Figure 5.7 and shown in the optical photomicrograph in Figure 5.8. Attack penetrated intergranularly on all grain

boundaries in the entire high temperature heat-affected zone. Behind the corrosion front grain dropping occurred.

The intermediate heat input welds (137 to 211 J/mm) were attacked in three regions, shown in Figure 5.7. In region B attack occurred on all the grain boundaries (ferrite-ferrite and ferrite-martensite), as shown in Figure 5.9. Behind the corrosion front, martensite suffered general corrosion, and grain dropping apparently occurred. Regions C and D are some distance from the weld, just outside the low temperature heat-affected zone in the parent material, as shown in Figures 5.9, 5.10 and 5.11. Attack also appeared to be intergranular, with the outer edges of this region apparently suffering from a more general type of corrosion. Considering that the parent material consists of long elongated ferrite grains, this seemingly equiaxed intergranular attack in the base metal appears inconsistent.

No attack was observed in the high heat input welds (263 to 432 J/mm) after the boiling test, as shown in Figure 5.12. Some of the autogenous butt-welds on the 41220 material cracked after the bend test, shown in Figure 5.13. On closer examination, these cracks were shown to be transgranular in nature, and not intergranular.

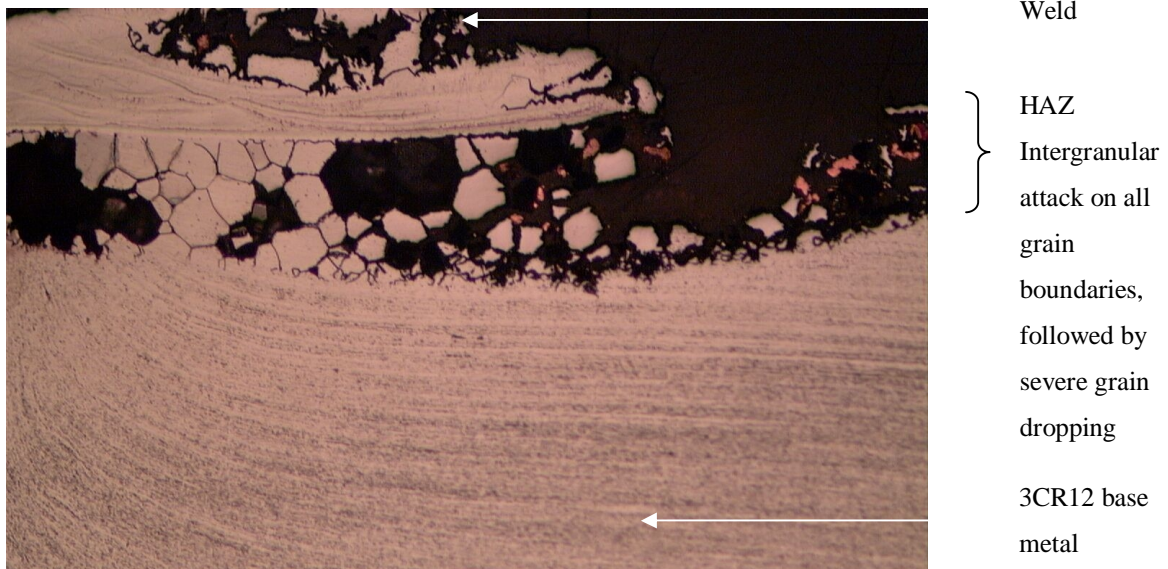


Figure 5.8. Optical photomicrograph of autogenous butt-weld B1 (41311 at 31.3 J/mm), etched with 10 % oxalic acid. (X200).

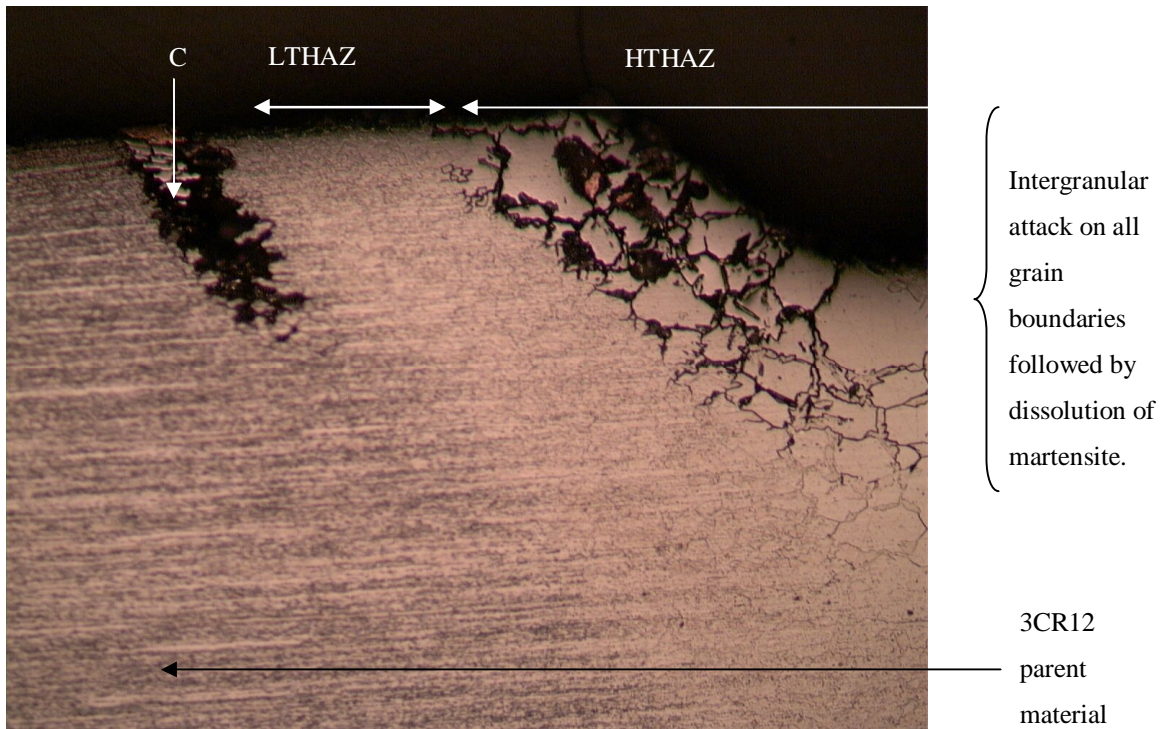


Figure 5.9. Optical photomicrograph of autogenous butt-weld A10 (41220 at 137.7 J/mm) after Practice Z, showing region C. Sample etched with 10% oxalic acid. (X500).

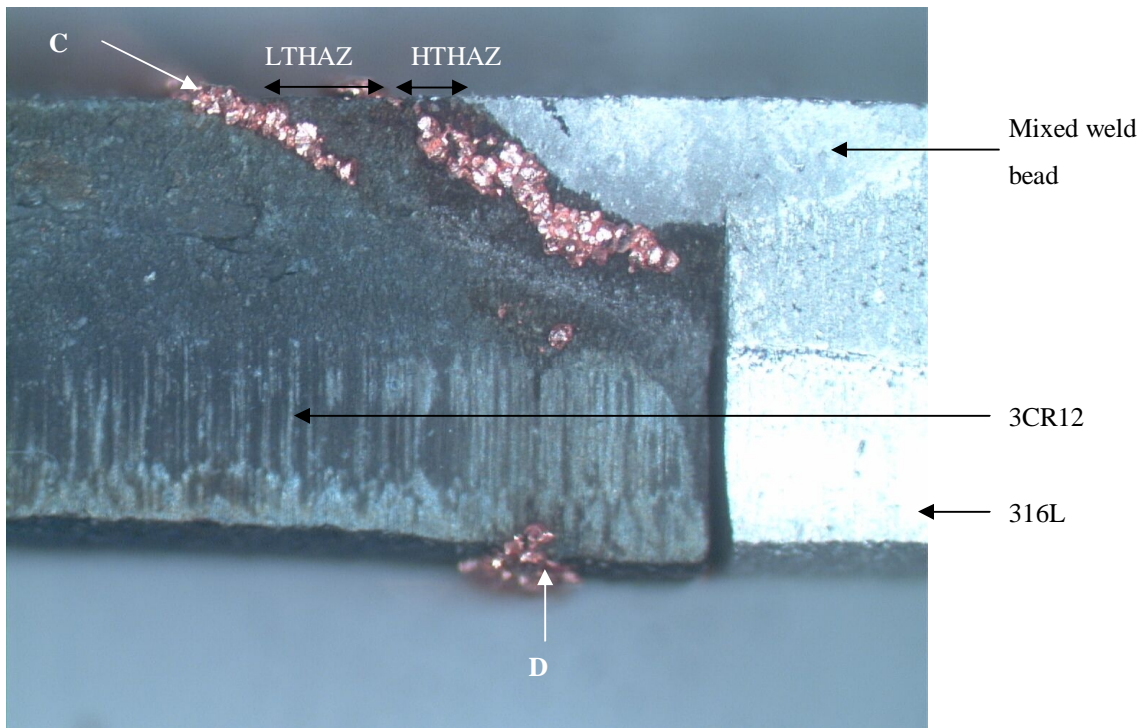


Figure 5.10. Stereo photomicrograph of autogenous butt-weld A11 (41220 at 153.6 J/mm) after Practice Z. (X11.4).

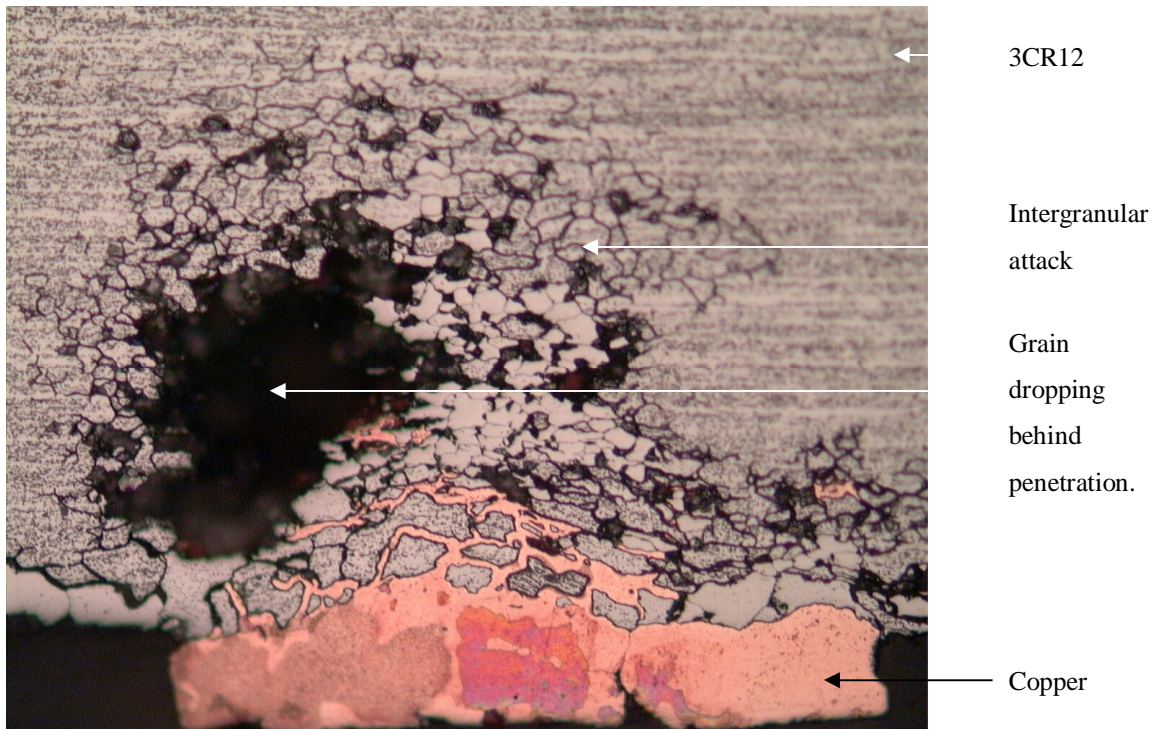


Figure 5.11. Optical photomicrograph of autogenous butt-weld A11 (41220 at 153.6 J/mm) after Practice Z, showing region D. Sample etched with 10% oxalic acid. (X200).

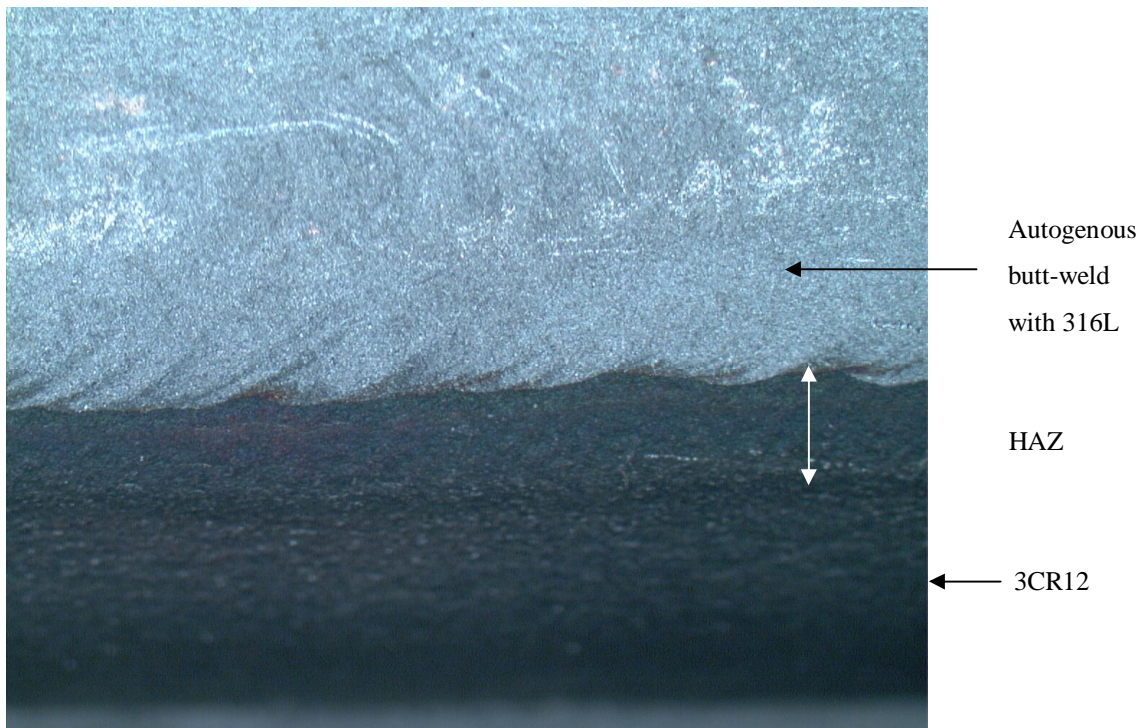


Figure 5.12. Stereo photomicrograph of autogenous butt-weld B20 (41311 at 308.4 J/mm) after Practice Z and bend test. No attack was observed. (X5.2).

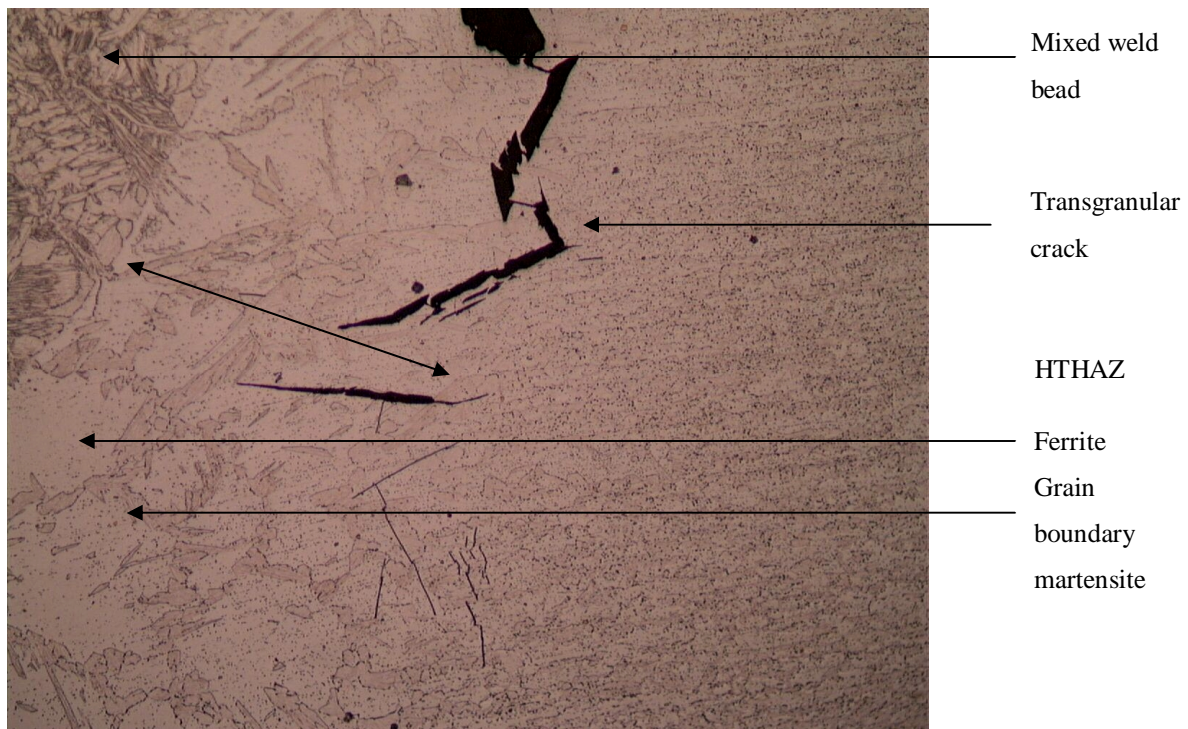


Figure 5.13. Optical photomicrograph of autogenous butt-weld A23 (41220 at 365.1 J/mm) after Practice Z and bend test. Sample etched with 10% oxalic acid. No intergranular attack observed on ferrite or martensite. (X100)

#### 5.6.1.2. Practice W: 10% oxalic acid electrolytic etch

The 10% oxalic acid electrolytic etch was performed at 1 A/cm<sup>2</sup> for 60 seconds for all the autogenous butt- and bead-on-plate welds. The test showed that the welds on 41220 and 41311 material fall into three broad categories in terms of the mode of attack. These categories seem to depend on the microstructure, and are summarised in Table 5.1. The results for all the welds are given in Tables B.8 and B.9 in Appendix B.

Category 1 refers to a microstructure that consisted of mostly ferrite-ferrite grain boundaries that were almost all severely ditched. Between 0 and 50% of the grain boundaries contained martensite. This signifies that at least one grain had no grain boundary martensite (all the boundaries were ferrite-ferrite), and that at least one grain had three of its sides covered in martensite. Severe ditching of the ferrite implies that the ferrite-ferrite grain boundaries may be sensitised. The absence of continuously ditched ferrite-martensite grain boundaries indicates that these boundaries are not in the sensitised condition.

Table 5.1. Summary of Practice W results in relation to heat-affected zone microstructure.

Category	Microstructure	Practice W
1	Mostly ferrite-ferrite grain boundaries.  Martensite on approximately 0 to 50% of all grain boundaries.	All ferrite-ferrite grain boundaries ditched.  Martensite-ferrite grain boundaries only slightly attacked in some areas.
2	Mostly ferrite-ferrite grain boundaries with some martensite-ferrite grain boundaries.  Martensite extending over at least ½ a grain boundary, over 65 – 100% of the grain boundary area.	Ferrite-ferrite grain boundaries ditched.  Martensite-ferrite grain boundaries only slightly attacked in some areas.
3	Almost no ferrite-ferrite grain boundaries, mostly martensite-ferrite grain boundaries.  Martensite on 65 to 100% of the grain boundaries.	Discontinuous carbide precipitation observed on any ferrite-ferrite grain boundaries present.  Most of the grain boundaries contain martensite, and show discontinuous carbide precipitation.

Figures 5.14 and 5.15 show the lower end of the category where almost no grain boundary martensite is present in the HTHAZ (Category 1). In this structure a continuous network of ditched ferrite-ferrite grain boundaries is present. Very little martensite is present in the high temperature heat-affected zone, and the martensite shows little or no grain boundary attack.

Figures 5.16 and 5.17 show category 1 welds containing more martensite, although almost half of the grain boundaries are still ferrite-ferrite.

Category 2 includes microstructures with at least half of the grain boundaries containing martensite, with up to 65% (in the case of 41220) and 100% (for 41311) of the boundaries covered with martensite, as shown in Figures 5.18 and 5.19. This indicates that some ferrite-ferrite grain boundaries remain, although most of the grain boundaries are covered with martensite. Any ferrite-ferrite grain boundaries present show ditching, but only sporadic carbide attack was observed on the ferrite-martensite grain boundaries.

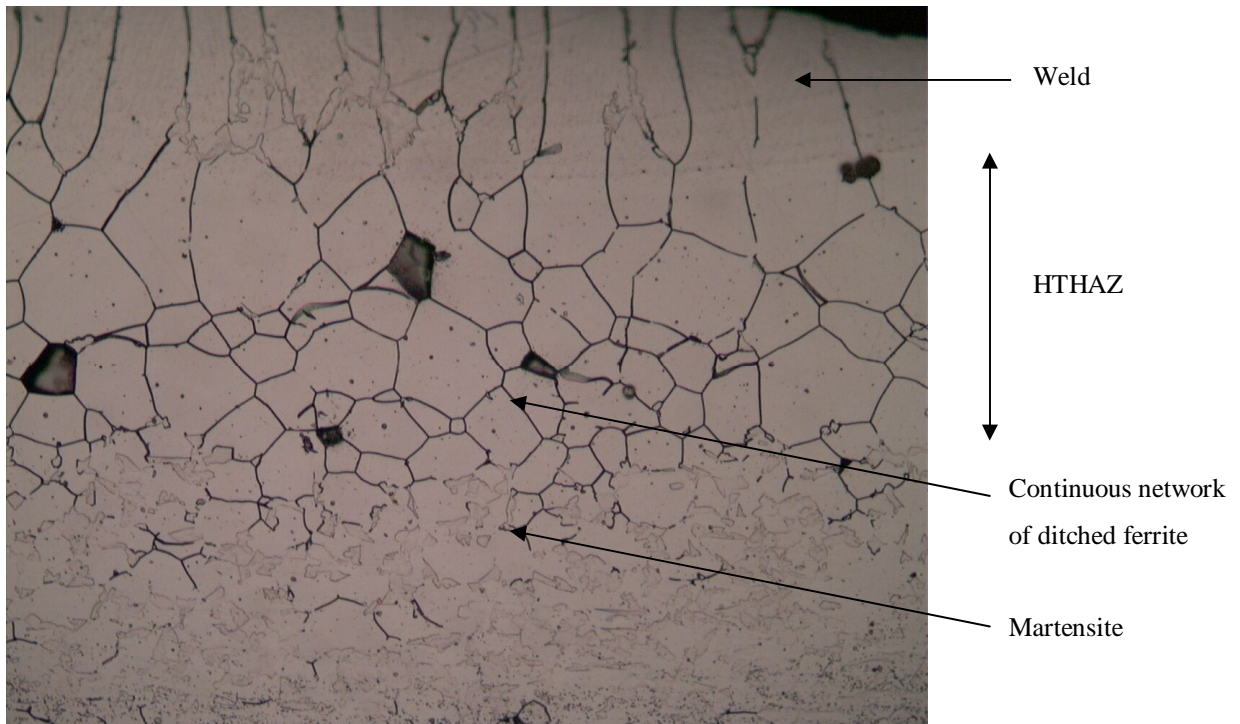


Figure 5.14. Optical photomicrograph of autogenous bead-on-plate weld A2 (41220 at 31.2 J/mm) etched with 10% oxalic acid. Continuous network of ditched ferrite-ferrite grain boundaries present. (X200).

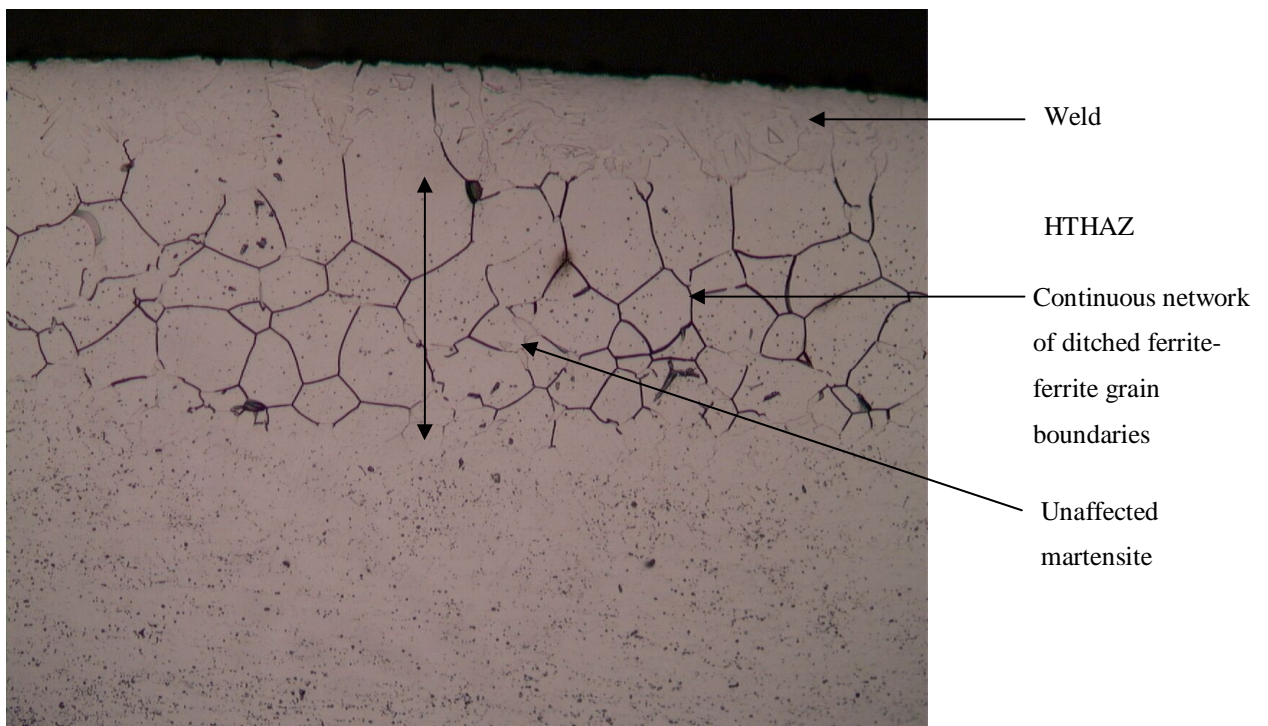


Figure 5.15. Optical photomicrograph of autogenous bead-on-plate weld B2 (41311 at 28.1 J/mm) etched with 10% oxalic acid. Continuous network of ditched ferrite-ferrite grain boundaries present. (X200).

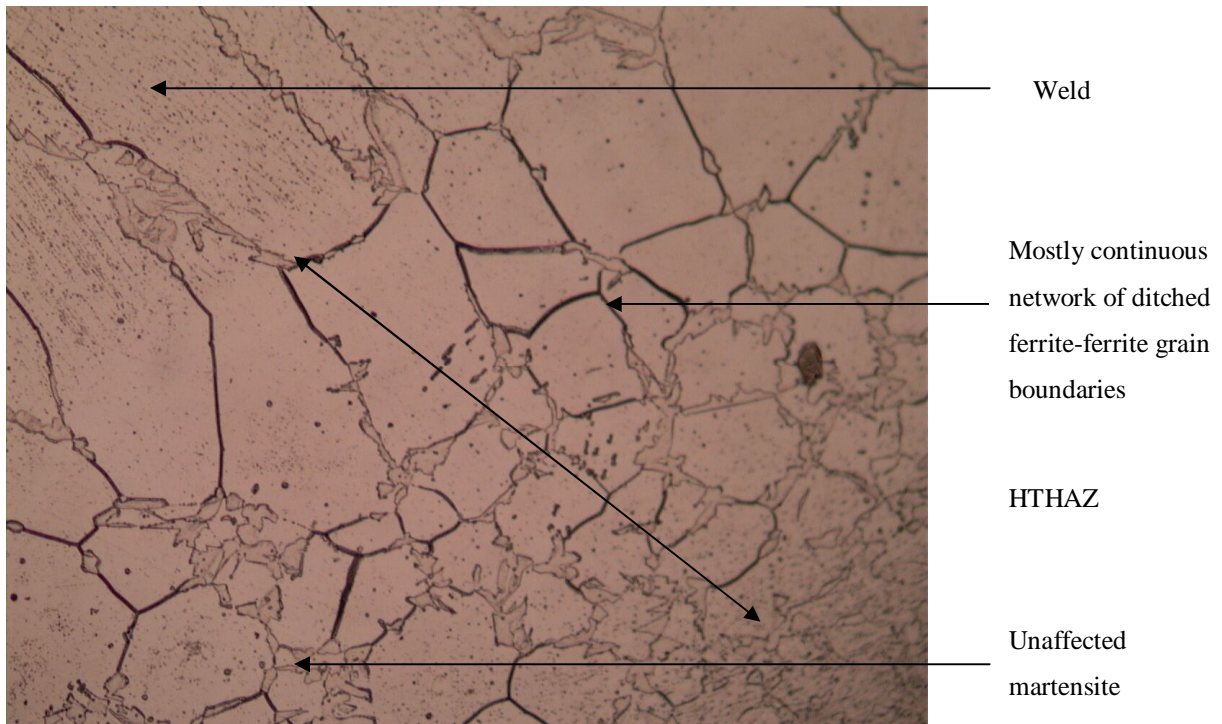


Figure 5.16. Optical photomicrograph of autogenous bead-on-plate weld A10 (41220 at 137.7 J/mm) etched in 10% oxalic acid. Mostly continuous network of ditched ferrite-ferrite grain boundaries present. (X200).

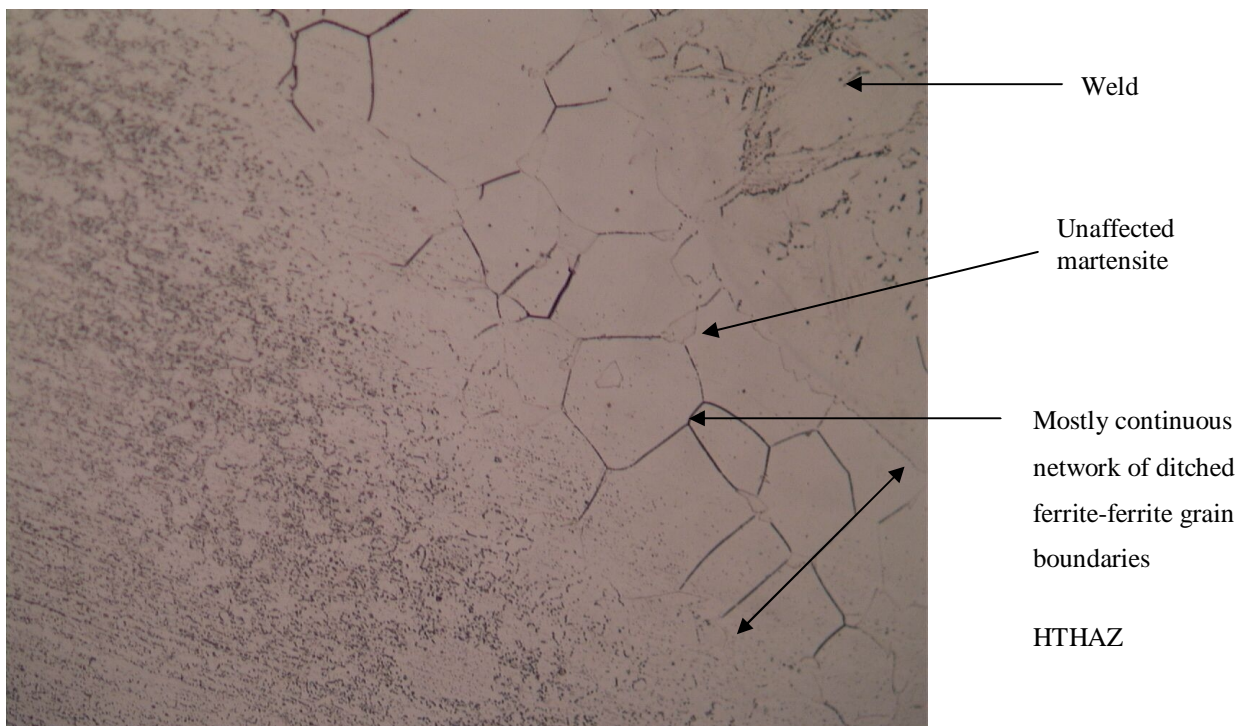


Figure 5.17. Optical photomicrograph of autogenous butt-weld B9 (41311 at 88 J/mm) etched in 10% oxalic acid. Mostly continuous network of ditched ferrite-ferrite grain boundaries present. (X200).

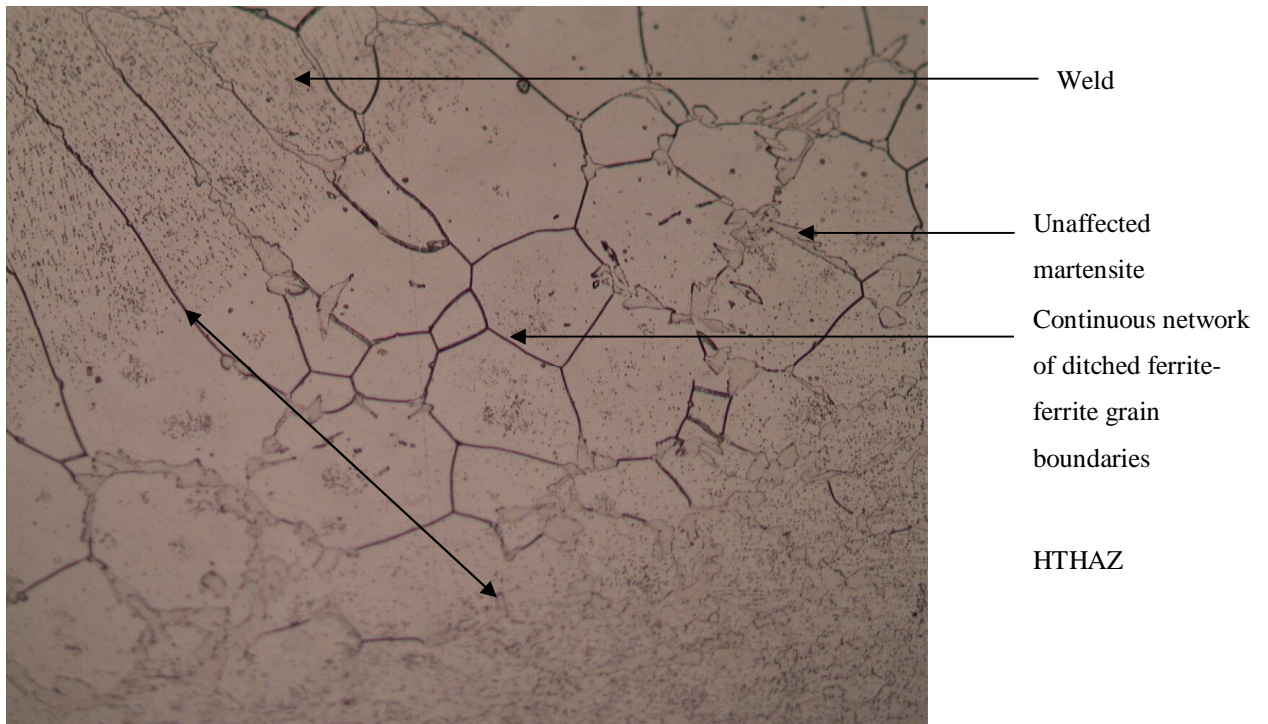


Figure 5.18. Optical photomicrograph of autogenous bead-on-plate weld A13 (41220 at 190.9 J/mm) etched with 10% oxalic acid. Continuous network of ditched ferrite-ferrite grain boundaries present. (X200).

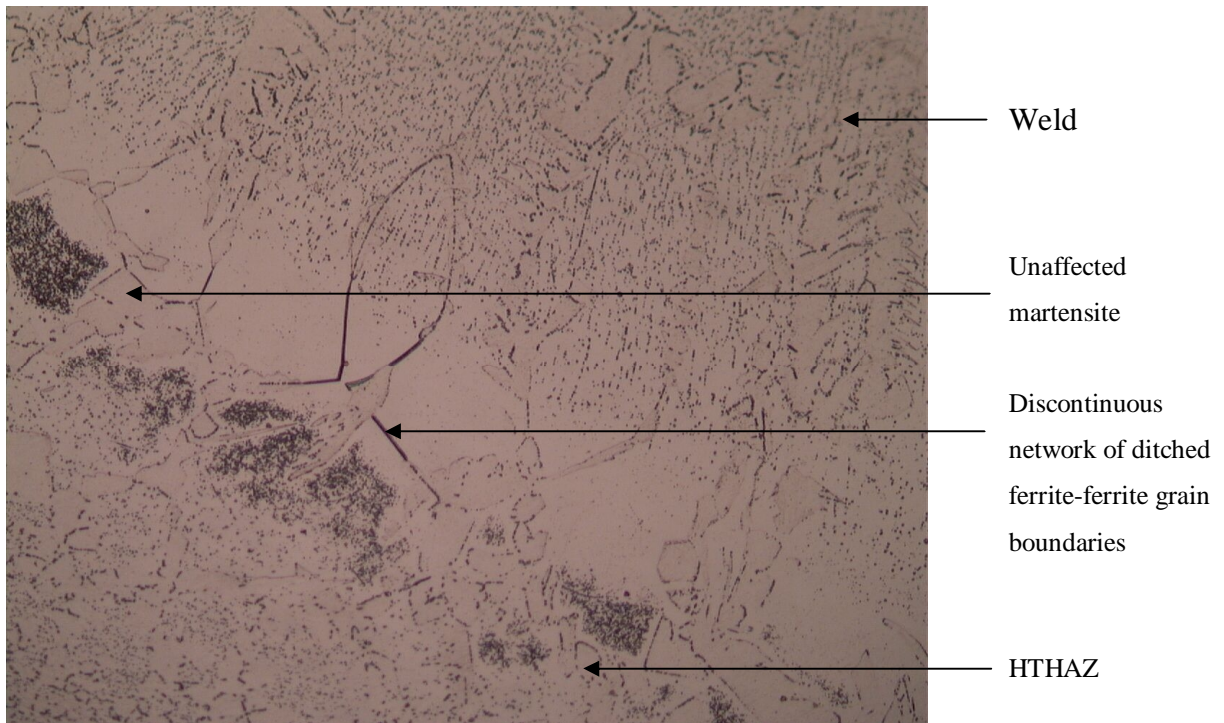


Figure 5.19. Optical photomicrograph of autogenous bead-on-plate B13 (41311 at 191.7 J/mm), 10% oxalic acid etch. No continuous ferrite-ferrite grain boundaries present. (X200).

The ditching observed on the ferrite-ferrite grain boundaries in category 2 indicates that sensitisation is possible, but additional tests are required to confirm this. The martensite-ferrite grain boundaries do not show continuous ditching, and are therefore assumed to be unsensitised, (shown in Figures 5.18 and 5.19).

The grain boundaries in category 3 do not show continuous ditching, as illustrated in Figures 5.20 and 5.21. Most of the grain boundaries contain martensite, with the martensite covering between 65% and 100% of the total grain boundary area in 41220 and up to 100% of the grain boundaries in 41311. This indicates that none of these grain boundaries are sensitised. A chromium depletion test will be used to confirm that these samples are in the unsensitised condition.

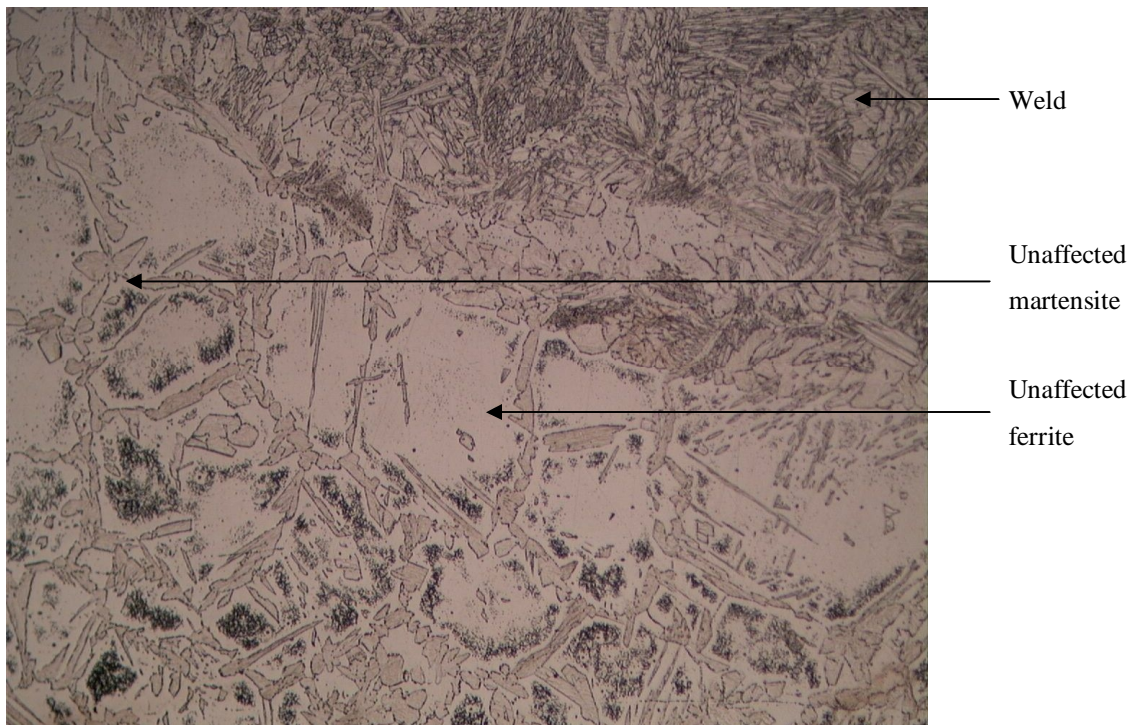


Figure 5.20. Optical photomicrograph of autogenous butt-weld A25 (41220 at 414.2 J/mm), etched with 10% oxalic acid. No ferrite-ferrite grain boundaries present. (X100).

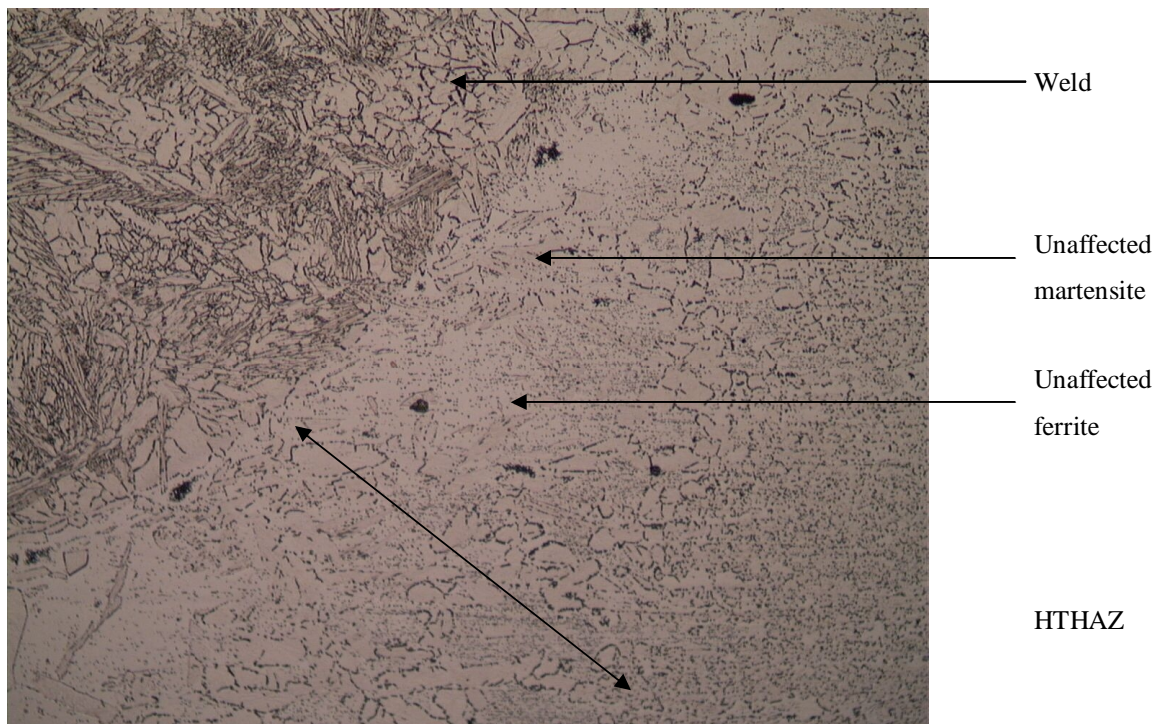


Figure 5.21. Optical photomicrograph of autogenous butt-weld B25 (41311 at 414.2 J/mm), etched with 10% oxalic acid. No ferrite-ferrite grain boundaries present. (X100).

#### 5.6.1.3 Chromium depletion test

Due to the unsatisfactory results of the Cu-CuSO<sub>4</sub>-6%H<sub>2</sub>SO<sub>4</sub> boiling test, a potentiostatic etch was applied to evaluate whether chromium depletion occurred as a result of the carbide precipitation observed after oxalic acid etching.

The potentiostatic scans were performed on an ACM potentiostat with a saturated calomel reference electrode. The potential was maintained at 0 V<sub>SCE</sub>, and the current for each sample was recorded. Unfortunately it is difficult to determine the area covered by the HTHAZ accurately. As a result, a current density value could not be calculated. A microstructural examination of the samples subjected to the test was preferred as a method of evaluation. The results agreed very well with those of the 10% oxalic acid electrolytic test: the ferrite-ferrite grain boundaries that were ditched during the oxalic acid etch generally displayed corresponding chromium depleted zones. Some of the results are considered below.

At the very low heat inputs, where almost no martensite is present in the HTHAZ, all the ferrite-ferrite grain boundaries were attacked during the potentiostatic scan, as shown in Figure 5.22. In this example, some of the sub-grain boundaries also showed evidence of corrosive attack. This confirms that the ferrite-ferrite grain boundaries are in the sensitised condition.

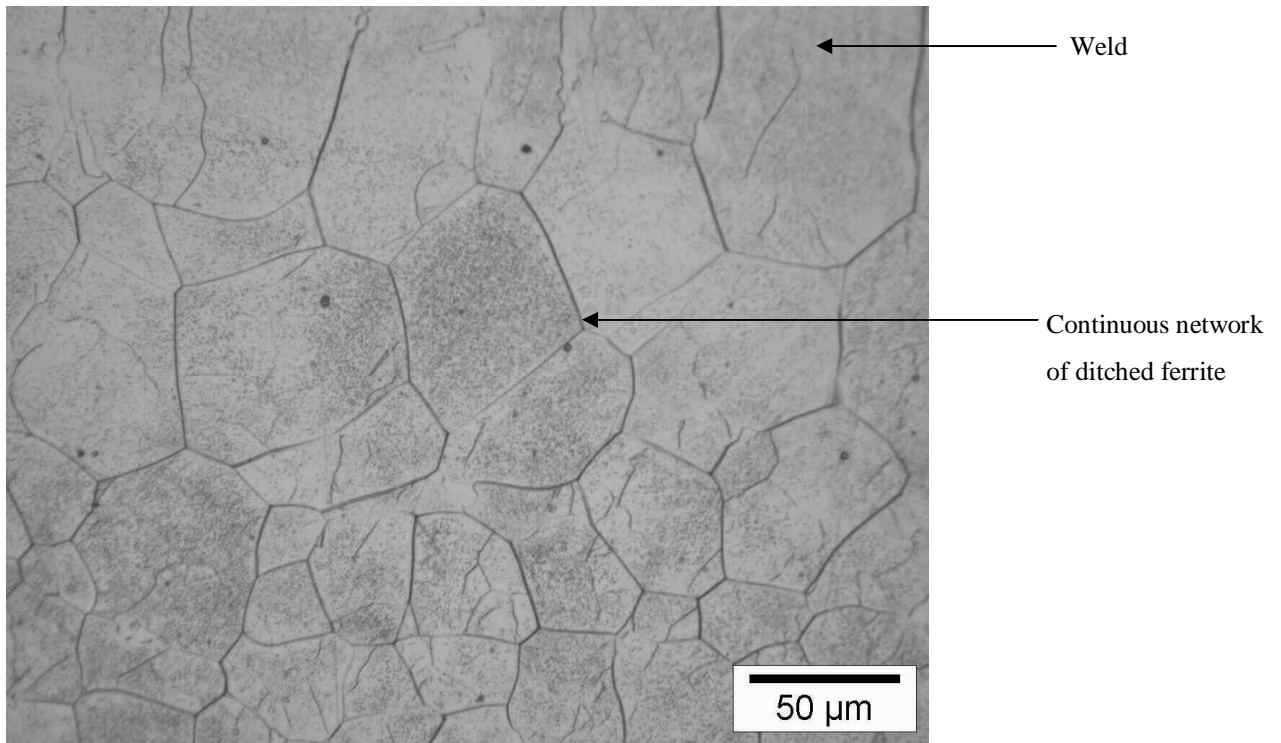


Figure 5.22. Optical photomicrograph of autogenous bead-on-plate weld A2 (41220 at 36.7 J/mm) after the potentiostatic chromium depletion test. Continuous network of ditched ferrite-ferrite grain boundaries present. (X500).

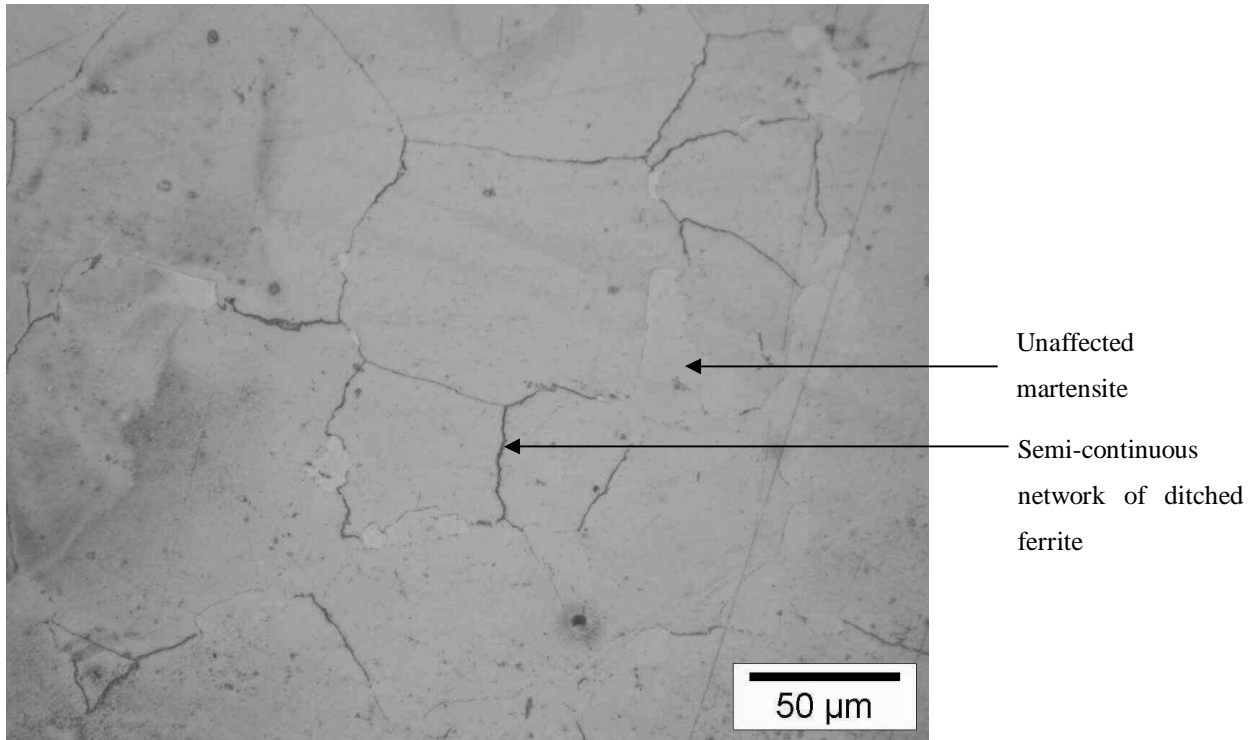


Figure 5.23. Optical photomicrograph of autogenous bead-on-plate weld A11 (41220 at 153.6 J/mm) after the potentiostatic chromium depletion test. Semi-continuous network of ditched ferrite-ferrite grain boundaries present. (X500).

In Figure 5.23, attack on the ferrite-ferrite grain boundaries is evident, while the lighter martensite phase shows virtually no grain boundary attack. Due to some staining of A14 after the potentiostatic etch, the martensite (shown as the lighter phase) is clearly visible in Figure 5.24. The lighter phase does not show any grain boundary ditching, whereas the grain boundaries of the darker ferrite phase are attacked. The same pattern is evident in Figure 5.25, where B12 shows pronounced attack of the ferrite-ferrite grain boundaries, but virtually no attack on the ferrite-martensite boundaries.

When a grain boundary is completely or almost completely covered in martensite, no chromium depletion is evident, as shown in Figures 5.26 and 5.27. This was confirmed by investigating these samples with a scanning electron microscope (SEM). SEM photomicrographs are shown in Figures 5.28 to 5.34. Note that the lighter phase is martensite and the darker phase ferrite.

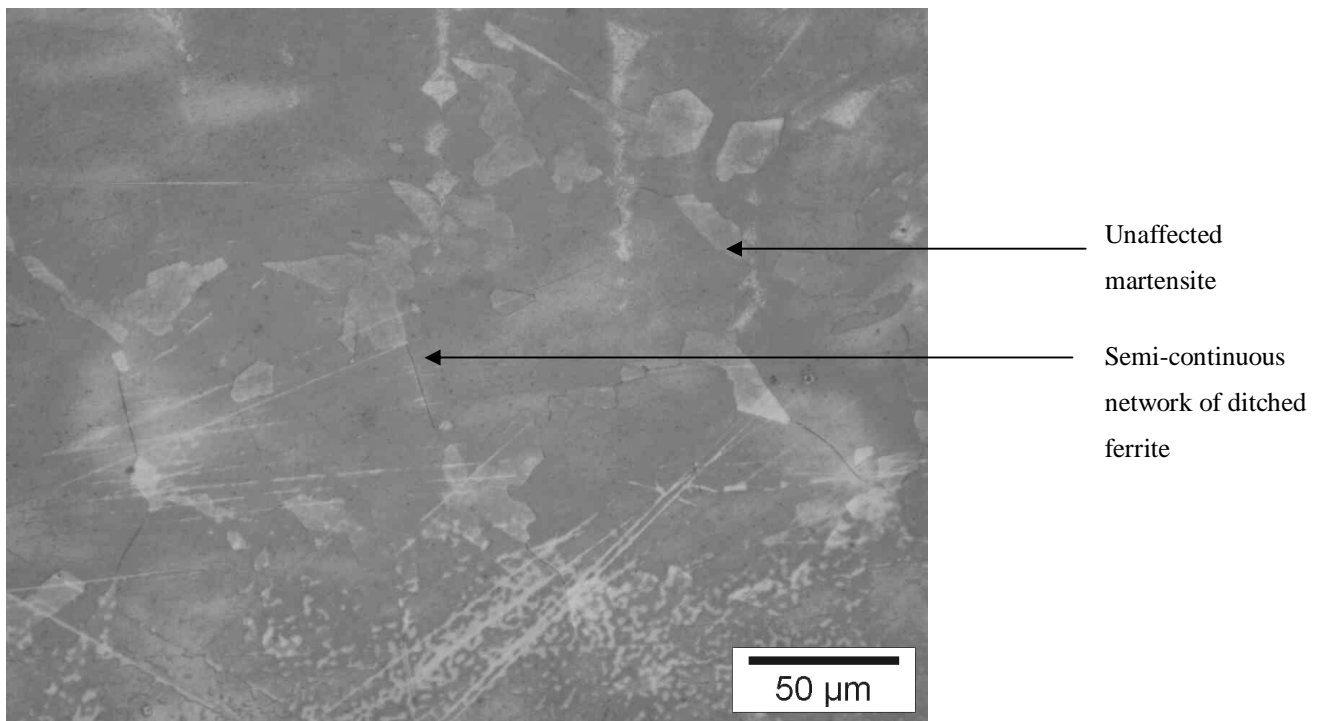


Figure 5.24. Optical photomicrograph of autogenous butt-weld A14 (41220 at 195.0 J/mm) after the potentiostatic chromium depletion test. Semi-continuous network of ditched ferrite-ferrite grain boundaries is present. (X500).

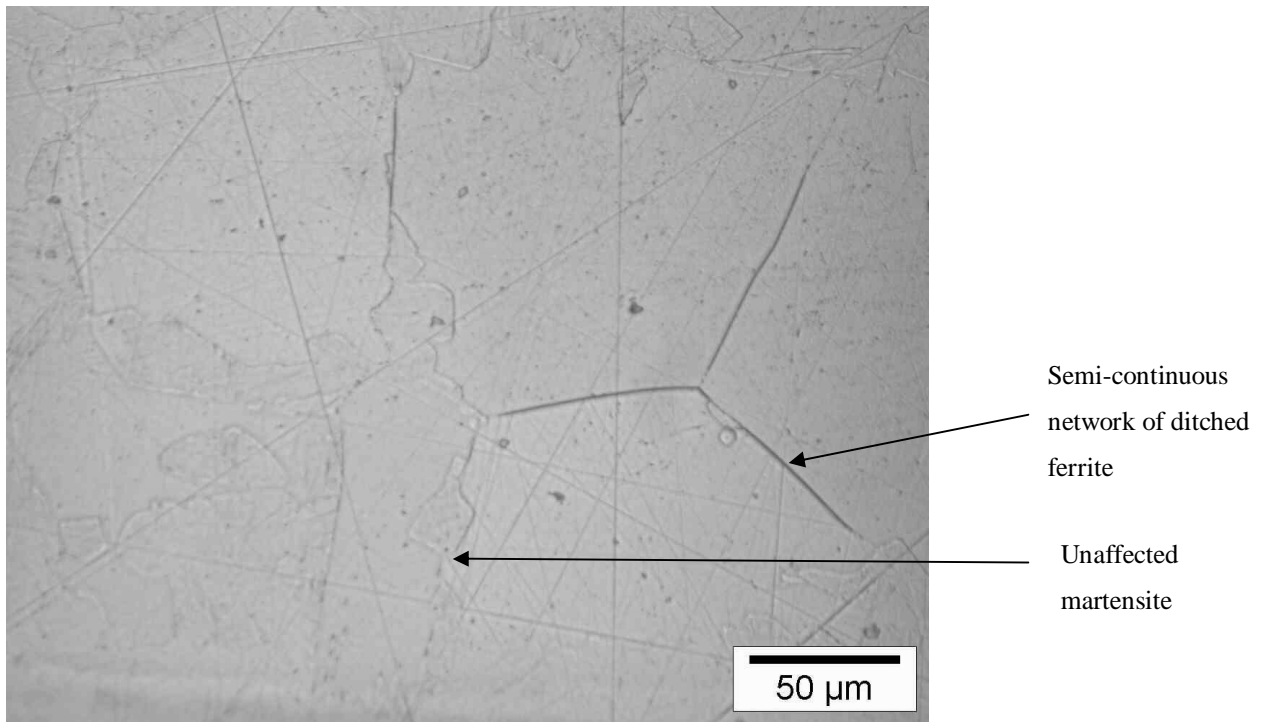


Figure 5.25. Optical photomicrograph of autogenous butt-weld B12 (41311 at 120.9 J/mm) after the potentiostatic chromium depletion test. A semi-continuous network of ditched ferrite-ferrite grain boundaries is visible. (X500)

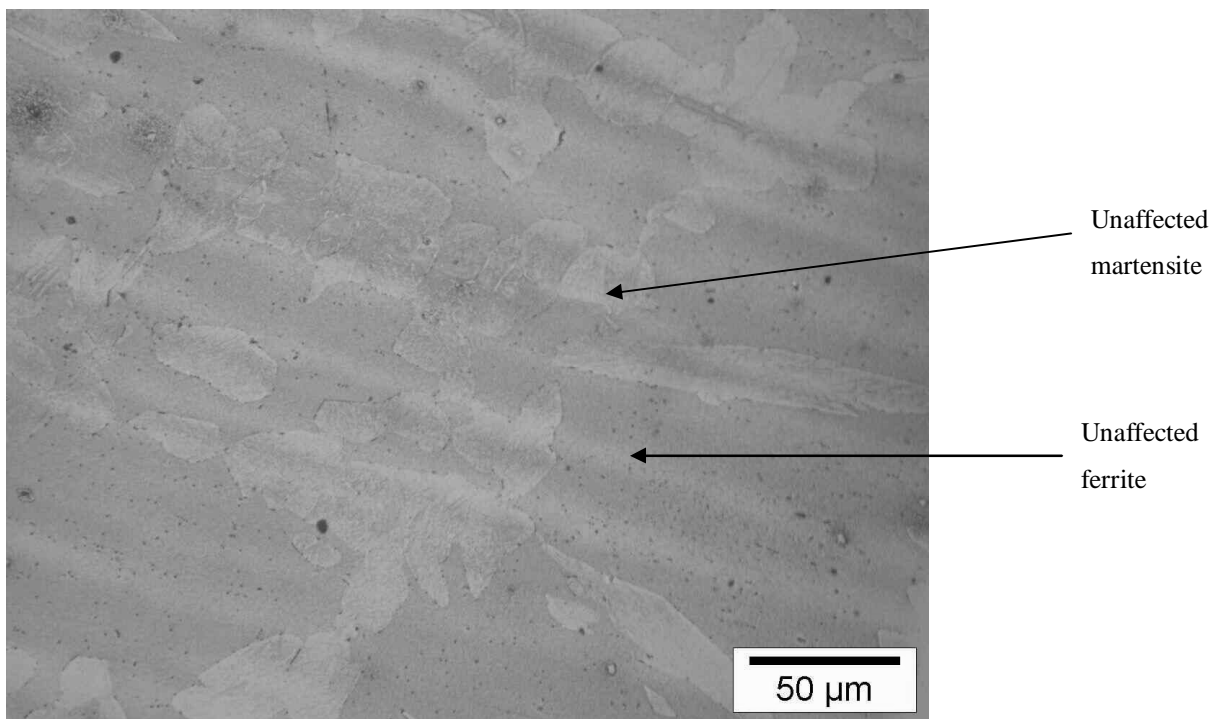


Figure 5.26. Optical photomicrograph of autogenous butt-weld A18 (41220 at 262.7 J/mm) after the potentiostatic chromium depletion test. No ferrite-ferrite grain boundaries are present (X500)

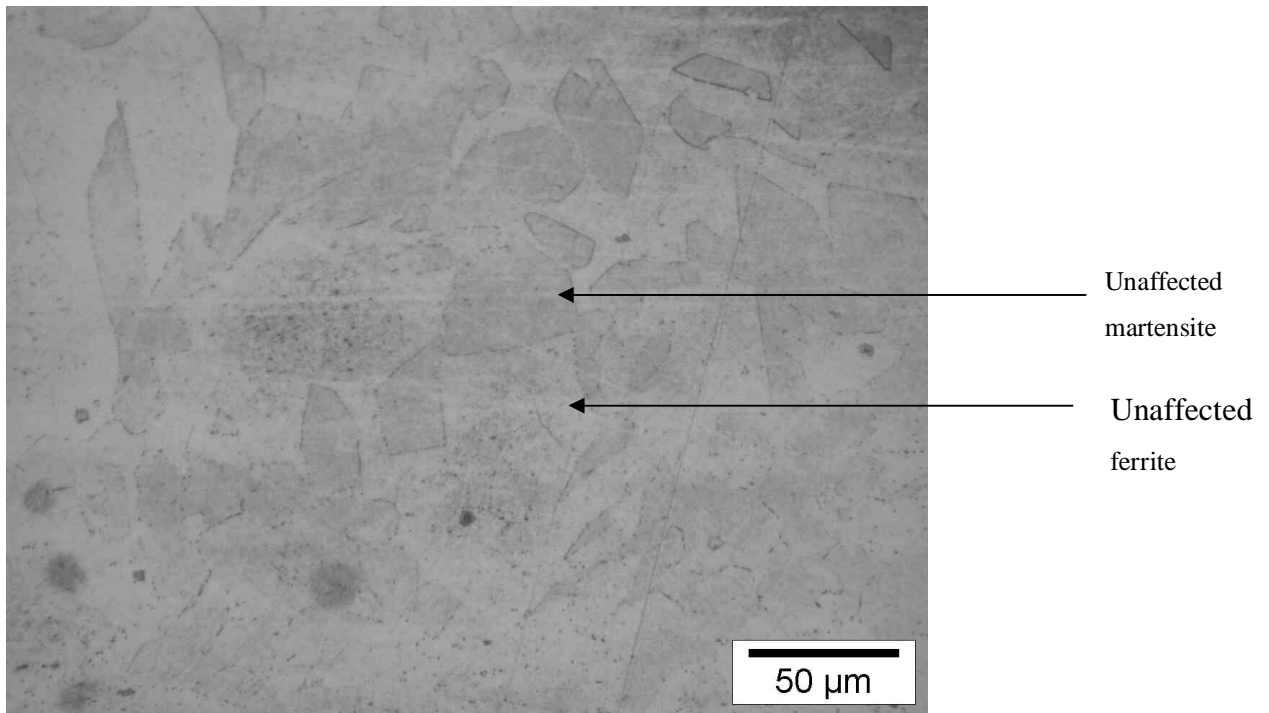


Figure 5.27. Optical photomicrograph of autogenous butt-weld B15 (41311 at 250.6 J/mm) after the potentiostatic chromium depletion test. No ferrite-ferrite grain boundaries are present. (X500)

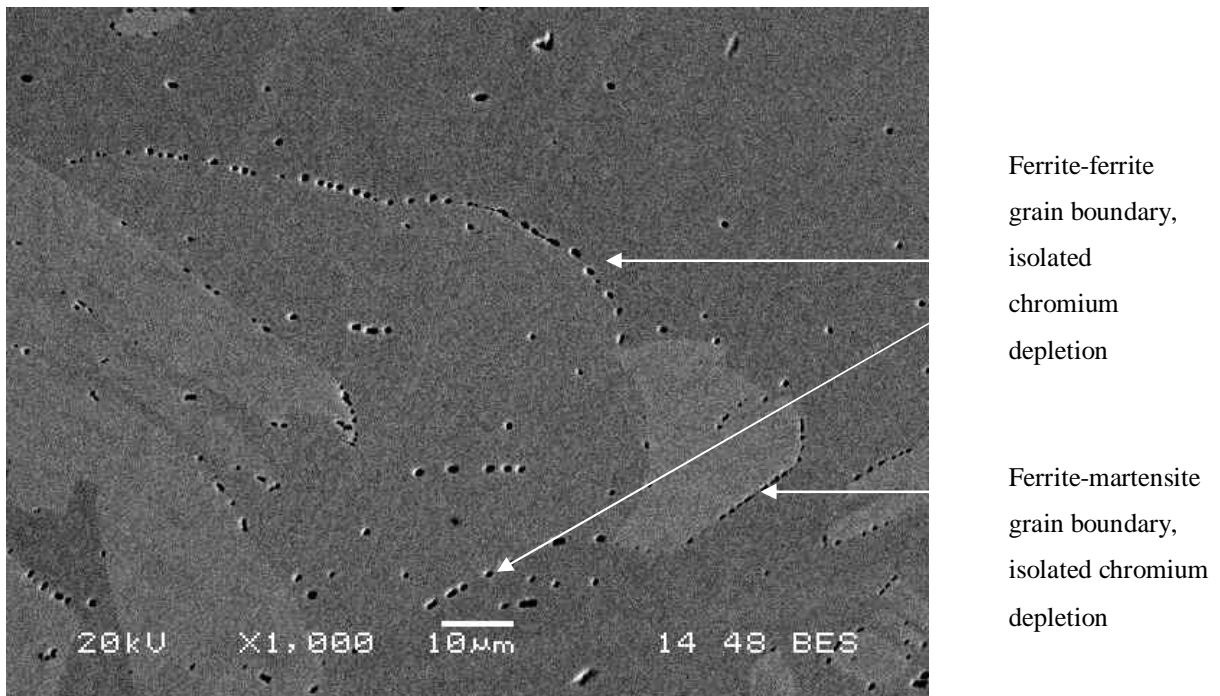


Figure 5.28. SEM backscatter photomicrograph of autogenous butt-weld A18 (41220 at 262.7 J/mm) after the potentiostatic etch. A ferrite-ferrite grain boundary is present, but it is not continuously ditched. (X1000).

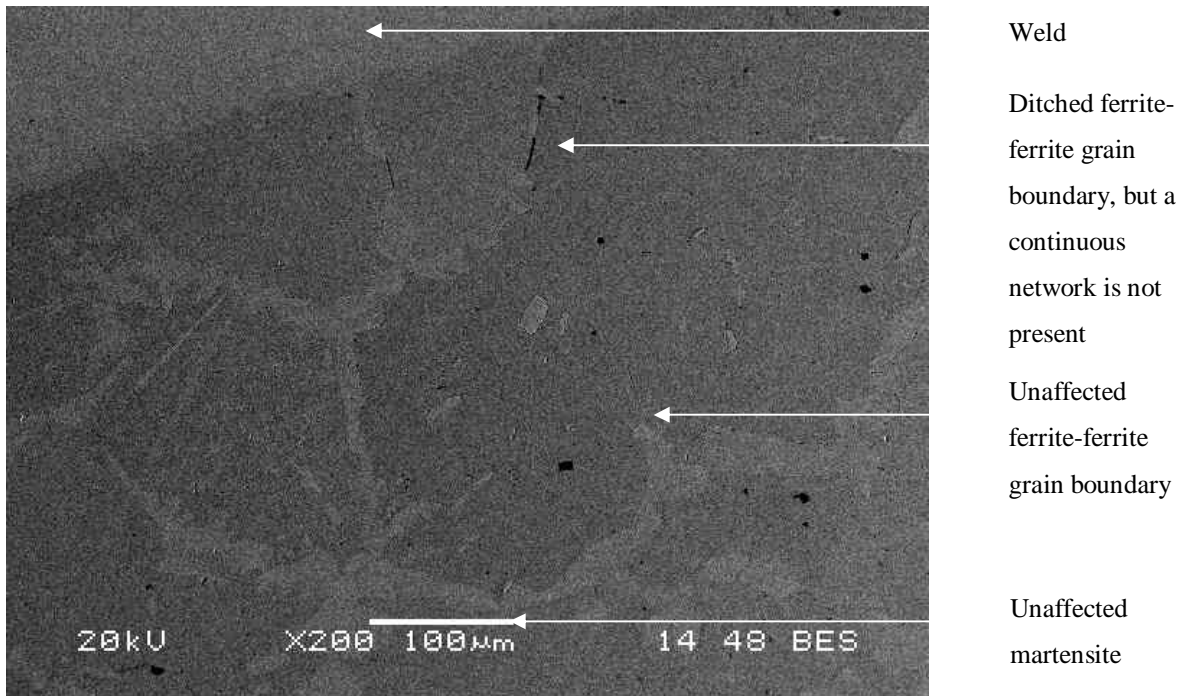


Figure 5.29. SEM backscatter photomicrograph of the HTHAZ of the autogenous butt-weld A18 (41220 at 262.7 J/mm) after the potentiostatic etch. Note the ditched ferrite-ferrite grain boundary close to the weld. (X200).

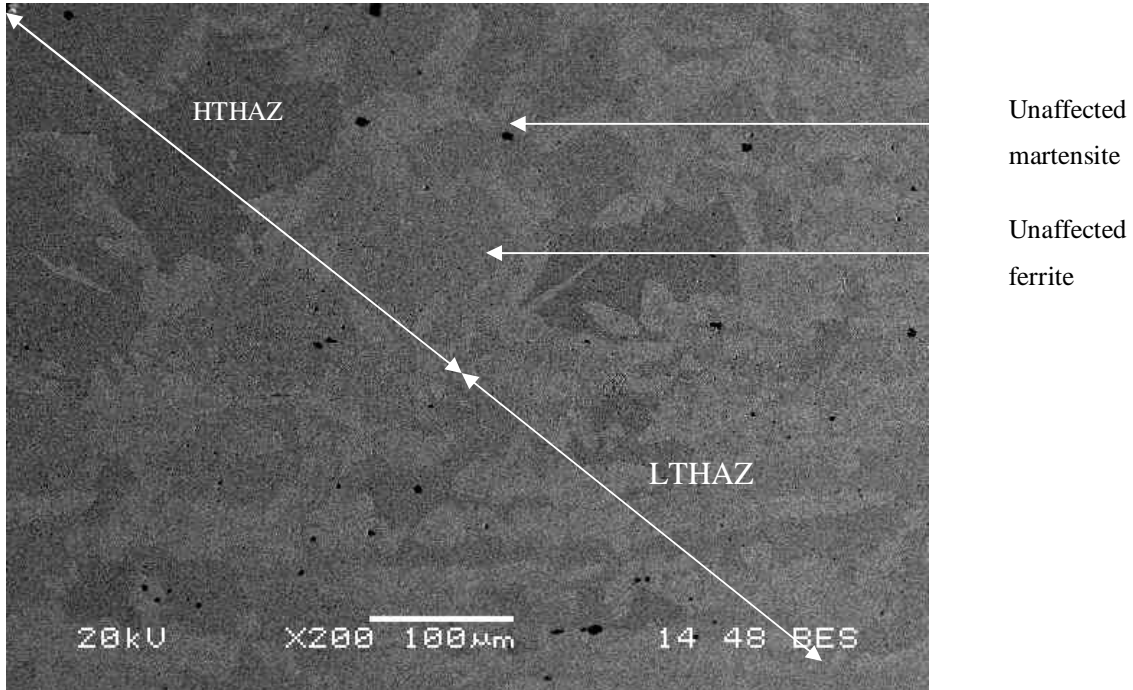


Figure 5.30. SEM backscatter photomicrograph of the HTHAZ and LTHAZ of the autogenous butt-weld A18 (41220 at 262.7 J/mm) after the potentiostatic etch. No ferrite-ferrite grain boundaries are present. (X200).

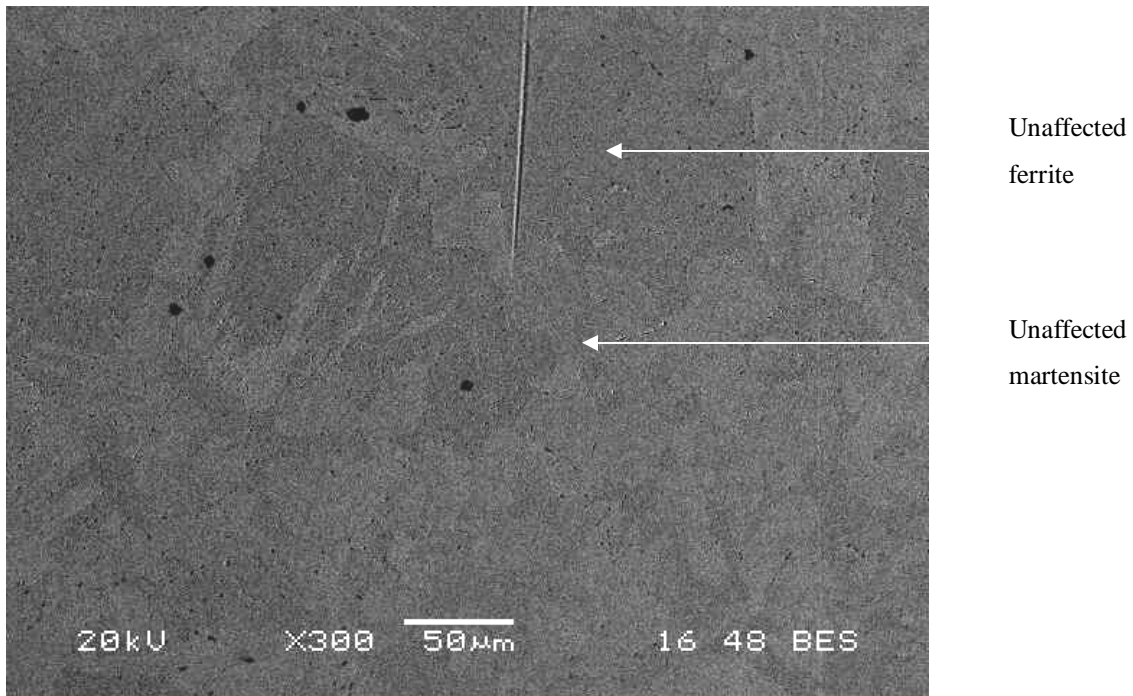


Figure 5.31. SEM backscatter photomicrograph of the HTHAZ and LTHAZ of the autogenous butt-weld B13 (41311 at 191.7 J/mm) after the potentiostatic etch. No ferrite-ferrite grain boundaries are present. (X300).

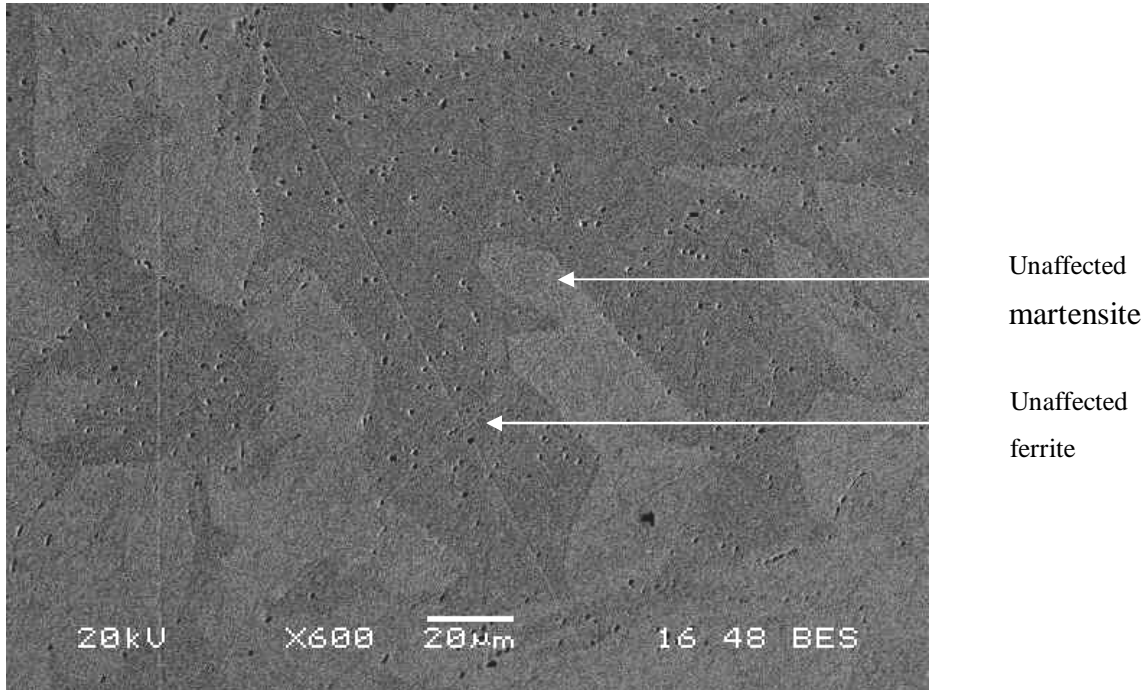


Figure 5.32. SEM backscatter photomicrograph of the HTHAZ of the autogenous butt-weld B13 (41311 at 191.7 J/mm) after the potentiostatic etch. No ferrite-ferrite grain boundaries are present. (X600).

Figures 5.28 to 5.30 show various regions of weld A18 after the potentiostatic etch. Some evidence of chromium depletion is visible in Figure 5.28, but attack is not continuous, even on the ferrite-ferrite grain boundary shown.

In Figure 5.29 most of the grain boundaries are covered in martensite and no attack is evident on these grain boundaries. Two ferrite-ferrite grain boundaries close to the weld bead show evidence of chromium depletion, but it should be noted that a continuous network of ditched ferrite-ferrite grain boundaries is not present. In Figure 5.30 a lower magnification was used, which shows the high temperature heat-affected zone as well as some of the low temperature heat-affected zone. No attack was observed.

Figure 5.31 shows a large area of weld B13, including the high temperature heat-affected zone and part of the low temperature heat-affected zone. Here, no ferrite-ferrite grain boundaries are present, only ferrite-martensite phase boundaries, as well as in Figure 5.32, which shows the high temperature heat-affected zone at a higher magnification. No chromium depletion is evident on any of the ferrite-martensite grain boundaries.

#### **5.6.2. Discussion**

Mass loss measurements, often used as a criterion for quantifying susceptibility to sensitisation, (especially with samples sensitised through isothermal heat treatment), is generally inappropriate for welds, since only a small portion of the sample is likely to be sensitised. Also, isothermally sensitised welds are generally quite homogeneous, while welds often display non-uniform microstructures and localised composition variations. Therefore, current density is also a difficult parameter to apply in the case of welds, as measurement of the sensitised area and estimation of the portion of the current contributed by this area make evaluation extremely difficult <sup>[1]</sup>. In this investigation, the microstructure of the welds after sensitisation testing was used to evaluate whether the high temperature heat-affected zone was in the sensitised condition.

The modified Practice Z of ASTM 763-99 showed evidence of intergranular attack that was not substantiated by either Practice W of the same standard, or by the 0.5 M H<sub>2</sub>SO<sub>4</sub> potentiostatic etch test that reveals chromium depletion. As a result, the attack observed in the parent material after the boiling acid test does not appear to be related to sensitisation and is therefore not relevant to this discussion. The remainder of this discussion will focus on the results from the other tests, which contribute to the understanding of 3CR12 sensitisation during low heat input welding.

The 10% oxalic electrolytic etch was designed to reveal the presence of chromium carbides. Since carbides may be present in an unsensitised, healed structure, the presence of carbides does not necessarily imply sensitisation, only its possibility. The absence of carbides, on the other hand, indicates that the structure is

not sensitised. The 0.5 M H<sub>2</sub>SO<sub>4</sub> potentiostatic etch reveals chromium depletion and is therefore a valid test to establish sensitisation.

The results from the oxalic acid etch and the 0.5 M H<sub>2</sub>SO<sub>4</sub> potentiostatic etch are in excellent agreement, and will therefore be discussed together. 41220 and 41311 show the same trends. After welding at low heat input levels, a continuous network of ferrite-ferrite grain boundaries exists in the high temperature heat-affected zone. The ferrite-ferrite grain boundaries contain chromium carbide precipitates, present in the form of an unbroken network. The presence of intergranular chromium-rich carbides result in chromium depletion in the region of the ferrite-ferrite grain boundaries, confirmed through potentiostatic etching. The martensite content increases as the heat input increases, and at some point (different for the two steels) a largely continuous network of martensite-ferrite grain boundaries emerges. Once a predominantly continuous martensite network is present, sensitisation ceases to be a problem. Carbon preferentially partitions to the high temperature austenite phase, and when most of the grain boundaries are covered in austenite during cooling, these act as a carbon sink preventing the supersaturation of the ferrite phase and subsequent carbide precipitation.

The same phenomenon is observed in duplex ferritic-austenitic stainless steels.

Weld A18 in grade 41220 (262.7 J/mm) and weld B13 in grade 41311 (191.7 J/mm) represent the lowest heat input levels where no sensitisation was detected. Photomicrographs of these welds show that continuous ditching of grain boundaries did not occur during oxalic acid etching or potentiostatic etching. This indicates that these welds are not sensitised. It can be assumed that all the welds in the welding matrix examined in this investigation that were performed at higher heat input levels than A18 and B13 (A19 to A26 and B14 to B26) are also not sensitised.

Differences in the behaviour of the two grades can be attributed to the chemical composition variation. The pertinent differences between these two grades (including material chemistry in terms of carbon, nickel and chromium) are shown in Table 5.2. This shows that 41311 has a third less carbon than 41220, almost the same chromium content, and more nickel (almost double). From the Kalthauser ferrite factor calculation, it follows that 41311 has a higher austenite potential than 41220. This results in more austenite forming during cooling in the 41311 material than in 41220 at the same welding parameters.

B13 was welded at a lower heat input and a faster welding speed than A18, resulting in a faster cooling rate and a similar martensite content. 41311 therefore retains a continuous martensite network on the grain boundaries at a lower heat input than 41220, implying that a faster cooling rate, and therefore a higher welding speed, can be tolerated.

It is interesting to note that the Ti/(C+N) ratios of the two grades are different. Even though grade 41311 has a ratio almost six times higher than 41220, it still suffered from sensitisation during low heat input welding. From the results, it seems that a higher Ti/(C+N) ratio helps to restrict the range of heat inputs resulting in sensitisation, but it does not prevent sensitisation.

*Table 5.2. Summary of differences between A18 and B13. These welds represent the lowest heat inputs where no sensitisation was observed during this investigation.*

	A18 (grade 41220)	B13 (grade 41311)
% Carbon (wt)	0.018	0.012
% Chromium (wt)	11.61	11.57
% Nickel (wt)	0.33	0.55
Kalthauser Ferrite Factor*	12.1	10.6
Ti/(C+N)	0.814	4.714
$\Delta t_{15-8}$ (s)	8.27	2.39
Cooling rate ( $^{\circ}\text{C/s}$ )	84.6	292.7
$q$ (W)	620	2217
$n$ (mm/s)	2.36	11.56
Heat input (J/mm)	262.7	191.8
% Martensite (estimate)	$26.6 \pm 2.4$	$22.2 \pm 3.0$

\*FF = Cr + 6xSi + 8xTi + 4xMo + 2xAl - 40x(C + N) - 4xNi

It can be concluded that low heat input welding and very fast cooling rates are deleterious for both grades of 3CR12 investigated. Although these results were obtained for arc welds, any welding process that results in low heat input levels, such as laser welding, could potentially lead to sensitisation. The expected benefits associated with low heat input levels and fast cooling rates (less grain growth and improved toughness in the heat-affected zone) in these type-EN 1.4003 steels, will only be realised at the cost of reduced corrosion resistance.

5.7. REFERENCES

1. Poulson, B. Sensitisation of ferritic steels containing less than 12% Cr. Corrosion Science. Vol. 18, Pergamon Press. 1978. pp. 371 - 395.

CHAPTER 6

SUMMARY AND CONCLUSIONS

6.1. SUMMARY

This investigation studied the sensitisation of a ferritic stainless steel during continuous cooling after welding. The steel examined during the course of this project forms part of the EN 1.4003 class of material and is supplied by Columbus Stainless, a primary stainless steel producer in South Africa, under the trade name of 3CR12.

The chemical composition of 3CR12 allows it to pass through the austenite + ferrite dual-phase field on the Fe-Cr phase diagram on cooling. During welding, the partial solid-state phase transformation to austenite aids in controlling heat-affected zone grain growth. To further restrict grain growth, a maximum heat input of 1 kJ/mm and a maximum interpass temperature of 100°C are recommended by Columbus Stainless. Austenitic welding consumables are specified for joining 3CR12 in the majority of applications. During welding, any austenite that forms on cooling through the  $\alpha + \gamma$  phase field, transforms to martensite at lower temperatures, resulting in typical heat-affected zone microstructures consisting of ferrite grains surrounded by grain boundary martensite.

Due to the dual-phase austenite-ferrite structure present in 3CR12 during cooling, it was originally believed to be largely immune to sensitisation during welding. A number of recent in-service failures were, however, caused by stress corrosion cracking associated with sensitisation during welding. It has since been shown that in order to sensitise 3CR12, the material needs to be heated to a temperature above the carbide dissolution range within the  $\alpha + \gamma$  phase field. If the as-supplied material, in its fully healed ferritic condition with the majority of the carbon trapped as carbides, is heat treated to such a temperature, the austenite formed will absorb most of the carbon that is liberated as the carbides dissolve. Upon cooling, the austenite transforms to martensite. If this martensite is subsequently heated within the carbide precipitation range, chromium-rich carbides precipitate on the martensite-ferrite grain boundaries, resulting in sensitised martensite. In practice, this requires heating to a temperature above approximately 950°C, followed by rapid cooling, and then reheating to a temperature within the carbide precipitation range (during heat treatment or welding). Multiple welds with overlapping heat-affected zones can also sensitise during welding, but this phenomenon is restricted to welds with very specific geometries.

The objective of this investigation was to demonstrate that a single 3CR12 weld can sensitise during continuous cooling after welding. This occurs when low heat input welding results in very fast cooling rates. Rapid cooling after welding can suppress austenite nucleation as the heat-affected zone cools through the  $\alpha + \gamma$  phase field, resulting in almost fully ferritic high temperature heat-affected zone (HTHAZ)

microstructures. The ferrite phase is supersaturated in carbon, and extensive carbide precipitation occurs at the ferrite-ferrite grain boundaries. The fast cooling rate also prevents the back diffusion of chromium to the depleted regions adjacent to the chromium-rich carbides, resulting in a continuous network of sensitised ferrite-ferrite grain boundaries. As the heat input increases, the cooling rate is reduced and more austenite forms in the heat-affected zone. This austenite transforms to martensite at lower temperatures and is retained down to room temperature as a grain boundary martensite network. If enough austenite forms on cooling to absorb excess carbon (austenite has a higher carbon solubility limit than ferrite), a continuous network of chromium depleted zones does not form and sensitisation is prevented. Slower cooling after welding at higher heat input levels also allows the ferrite to desensitise through diffusion of chromium from the grain interiors into any chromium depleted zones.

During the course of this investigation, two grades of 3CR12 with slightly different chemistries (grade 41220 has a lower austenite potential than grade 41311) were welded using a series of effective heat inputs ranging from about 30 J/mm to almost 500 J/mm. Gas tungsten arc welding with argon shielding gas was used to produce autogenous bead-on-plate welds, and to join 3CR12 autogenously to AISI 316L using square butt welds. This procedure was used to restrict corrosive attack to the heat-affected zone during sensitisation testing. A conduction-driven heat flow model was used to determine the efficiency of the welding machine in order to calculate the actual heat input of each experimental weld. Various calculations were performed to demonstrate the influence of welding parameters (such as heat flux,  $q$ , and welding speed,  $v$ ) on the cooling rate after welding and on the measured martensite content of the high temperature heat-affected zone.

The martensite content of the high temperature heat-affected zone of each experimental weld was estimated using point-counting techniques. After welding at very low heat input levels (around 30 J/mm), a continuous network of ferrite-ferrite grain boundaries, with almost no martensite, was observed in the HTHAZ. With an increase in heat input, an increase in the HTHAZ martensite content was noted. Due to its higher austenite potential, grade 41311 contained more HTHAZ martensite than grade 41220 after welding at comparable heat input levels. Grade 41311 formed an almost continuous network of martensite on the HTHAZ grain boundaries at a lower minimum heat input (192 J/mm, corresponding to a cooling rate of 293°C/s) than grade 41220, where continuous ferrite-ferrite grain boundaries only disappeared after welding at heat inputs of 263 J/mm (corresponding to a cooling rate of 85°C/s) or higher. Both welds contained almost the same amount of martensite after welding at these heat input levels (grade 41311 contained 22.2% ( $\pm 3.0$ ) martensite, and grade 41220 contained 26.6% ( $\pm 2.4$ )).

Three tests were used to assess whether the heat-affected zones were in the sensitised condition after welding. A modified Strauss test (with a reduced acid content and shorter exposure time than prescribed by Practice Z of ASTM 763-99 to compensate for the low chromium content of 3CR12) was used to reveal

embrittlement caused by sensitisation and intergranular attack. After bending, the samples were mounted, polished and etched electrolytically in a saturated oxalic acid solution (Practice W of ASTM 763-99) to reveal the presence of carbides in the structure. Since the modified Strauss test yielded unsatisfactory results, a 0.5 M H<sub>2</sub>SO<sub>4</sub> potentiostatic etch was used to verify the results of the oxalic acid etch. This test produced preferential attack of any chromium depleted regions in the HTHAZ of the experimental welds.

The oxalic acid electrolytic etch revealed that extensive chromium carbide precipitation occurred on any ferrite-ferrite grain boundaries in the HTHAZ. At low heat input levels, almost continuous networks of ditched ferrite-ferrite grain boundaries were observed in the HTHAZ. At higher heat inputs, an increase in grain boundary martensite content was observed, but ferrite-ferrite grain boundaries remained ditched. Even in high heat input welds, where most of the HTHAZ grain boundaries were covered with martensite, isolated ferrite-ferrite grain boundaries were ditched. Discontinuous carbide precipitation was observed on some of the ferrite-martensite boundaries, but in the majority of the samples examined, attack was largely restricted to the ferrite-ferrite boundaries.

The potentiostatic etch test confirmed the results of the electrolytic oxalic acid etch. Chromium depleted zones, associated with the ferrite-ferrite grain boundaries, were observed in the high temperature heat-affected zones of the low heat input welds that contained almost no martensite. As the martensite content increased, chromium depleted zones were noted at the ferrite-ferrite grain boundaries, whereas the martensite phase appeared mostly unaffected. High heat input welds, with martensite covering most of the HTHAZ grain boundaries, displayed chromium depletion on isolated ferrite-ferrite grain boundaries, but continuous chromium depleted networks were no longer visible. The lowest heat input levels where continuous chromium depleted zones were observed were 263 kJ/mm for grade 41220 (weld A18) and 192 kJ/mm for grade 41311 (weld B13). In welds produced at higher heat input levels, ferrite-ferrite grain boundaries were virtually eliminated, and the heat-affected zones were shown to be unsensitised.

## 6.2 CONCLUDING REMARKS

Based on the results obtained during this investigation, the following conclusions were drawn:

Sensitisation of 3CR12 during continuous cooling after welding is possible if low heat inputs are used.

Welding at low heat input levels can suppress transformation to austenite as the heat-affected zone cools through the  $\alpha + \gamma$  dual-phase region during welding. This results in largely ferritic high temperature heat-affected zones.

Carbon supersaturation of the ferrite occurs in the absence of sufficient austenite during cooling, resulting in extensive carbide precipitation on the ferrite-ferrite grain boundaries. Chromium back diffusion is prevented by rapid cooling, and the ferrite-ferrite grain boundaries are sensitised to intergranular corrosion.

With an increase in heat input, cooling after welding is delayed, and more austenite forms in the high temperature heat-affected zone. Sensitisation is prevented by the presence of enough martensite to eliminate continuous ferrite-ferrite grain boundaries.

A sufficiently high austenite potential should be maintained to promote austenite formation during cooling. In this respect, a reduction in carbon content or an increase in the amount of ferrite-forming elements in 3CR12 needs to be balanced by the addition of austenite-forming elements, such as nickel.

Excessive welding speeds appear to exacerbate sensitisation during low heat input welding.

### 6.3 RECOMMENDATIONS

In addition to specifying a maximum heat input for welding 3CR12 (to limit heat-affected zone grain growth), guidelines supplied to fabricators should include a minimum recommended heat input level. This minimum heat input will be a function of the plate thickness and chemistry, but 300 J/mm appears to be an appropriate limit for 3 mm plate. Heat flow modelling can be used for different 3CR12 chemistries to calculate appropriate minimum heat input levels for various plate thicknesses. A maximum fusion line cooling rate of 80°C/s ( $\Delta t_{15-8} = 8.75$  s) can be used as a preliminary guideline to distinguish between heat inputs likely to cause sensitisation, and those where cooling after welding is slow enough to prevent the formation of continuous chromium depleted zones.

Guidelines should also emphasize the harmful effect of fillet weld overlap (most welding standards limit the amount of allowable overlap) and excessive welding speeds.

Stabilised grades of 3CR12 were recently introduced into the market by Columbus Stainless. Further research is needed to determine whether these grades are susceptible to sensitisation after welding at low heat input levels.

## Appendix A

Table A.1. Original welding matrix.

Weld	Welding current	Arc Potential	Welding speed	Heat input
	(A)	(V)	(mm/s)	(J/mm)
1	167	14	33.33	70
2	97	12	16.67	70
3	44	8	5.00	70
4	222	15	33.33	100
5	128	13	16.67	100
6	50	10	5.00	100
7	317	21	33.33	200
8	208	16	16.67	200
9	91	11	5.00	200
10	263	19	16.67	300
11	167	15	8.33	301
12	125	12	5.00	300
13	259	18	11.67	399
14	208	16	8.33	400
15	143	14	5.00	400
16	231	18	8.34	499
17	167	15	5.00	501
18	83	10	1.67	497
19	200	15	5.00	600
20	91	11	1.67	599
21	219	16	5.00	701
22	106	11	1.67	698
23	235	17	5.00	799
24	111	12	1.67	798
25	250	18	5.00	900
26	125	12	1.67	898

## Appendix B

Table B.1 Welding parameters measured for 41220 joined to 316L using autogenous butt welds.

Weld	Welding current	Arc Voltage	Welding Speed	Heat Input
	A	V	mm/s	J/mm
A1	168	14	33.3	33.7
A2	109	10	16.7	31.2
A3	38	10	4.94	36.7
A4	222	14	33.3	44.6
A5	130	10	16.7	37.2
A6	50	9	4.94	43.5
A7	355	19	33.3	96.7
A8	223	15	16.7	95.7
A9	91	10	4.94	88.0
A10	301	16	16.7	137.7
A11	189	14	8.23	153.6
A12	125	10	4.94	120.9
A13	272	17	11.57	190.9
A14	210	16	8.23	195.0
A15	144	13	4.94	181.0
A16	252	17	8.23	248.6
A17	168	13	4.94	211.1
A18	118	11	2.36	262.7
A19	199	15	4.94	288.6
A20	127	12	2.36	308.4
A21	219	16	4.94	338.8
A22	135.5	12	2.36	329.1
A23	236	16	4.94	365.1
A24	146	13	2.36	384.1
A25	252	17	4.94	414.2
A26	164	13	2.36	431.5

Heat input corrected for an arc efficiency of:  $h = 47.76\%$

Table B.2 Autogenous bead-on-plate welds on 41220 used for microstructural work.

Weld	Welding Current	Arc Voltage	Welding Speed	Heat Input
	A	V	mm/s	J/mm
1	168	14	33.7	33.3
2	95	13	16.06	36.7
3	42	9	5.34	33.8
4	222.5	15.5	33.7	48.9
5	129	13	16.09	49.8
6	60	9	5.34	48.3
7	335	19	33.7	90.2
8	210	16	16.09	99.7
9	166	10	5.34	148.5
10	275	18	33.7	70.2
11	175	13	16.09	67.5
12	146	12	5.34	156.7
13	290	17	11.58	203.3
14	225	15	8.13	198.3
15	164	13	5.34	190.7

Heat input corrected for an arc efficiency of:  $h = 47.76\%$

Table B.3 Welding parameters measured for 41311 joined to 316L using autogenous butt-welds.

Weld	Welding current	Arc Potential	Welding Speed	Heat Input
	A	V	mm/s	J/mm
B1	168	13	33.3	31.3
B2	109	9	16.7	28.1
B3	38	9.5	4.94	34.9
B4	222	16	33.3	50.9
B5	130	10	16.7	37.2
B6	50	9	4.94	43.5
B7	352	20	33.3	101.0
B8	223	15	16.7	95.7
B9	91	10	4.94	88.0
B10	301	16	16.7	137.7
B11	190	15	8.23	165.4
B12	125	10	4.94	120.9
B13	273	17	11.56	191.7
B14	210	16	8.23	195.0
B15	144	18	4.94	250.6
B16	252	17	8.23	248.6
B17	168	14	4.94	227.4
B18	118	10	2.36	238.8
B19	199	15	4.94	288.6
B20	127	12	2.36	308.4
B21	219	16	4.94	338.8
B22	135.5	12.5	2.36	342.8
B23	236	16	4.94	365.1
B24	246	13	2.36	647.2
B25	252	17	4.94	414.2
B26	165	13	2.36	434.1

Heat input corrected for an arc efficiency of:  $h = 47.76 \%$

Table B.4 Autogenous bead-on-plate welds on 41311 used for microstructural work.

Weld	Welding current	Arc Potential	Welding Speed	HI
	A	V	mm/s	J/mm
1	168	14	33.7	33.3
2	95	13	16.09	36.7
3	42	9	5.34	33.8
4	222	16	33.7	50.3
5	129	13	16.09	49.8
6	60	9	5.34	48.3
7	335	19	33.7	90.2
8	210	16	16.09	99.7
9	106	10	5.34	94.8
10	275	18	16.09	146.9
11	175	13	8.13	133.6
12	146	10	5.34	130.6
13	290	17	11.58	203.3
14	225	15	8.13	198.3
15	164	13	5.34	190.7

**Heat input corrected for an arc efficiency of:  $h = 47.76\%$**

Table B.5. z used to calculate the cooling time from 1500 °C to 800 °C for equation 5.1.

Actual heat input (J/mm)	(m)
33.4	0.001489
47.76	0.001826
95.52	0.002965
143.28	0.004258
191.04	0.004885
238.8	0.007139
286.56	0.007675
334.32	0.008242
382.08	0.008385
429.84	0.012212

Table B. 6 Weld parameters, cooling time and rate (from 1500°C to 800°C) and % martensite measured in the high temperature heat-affected zone for 41220.

Weld	Welding current (A)	Arc potential (V)	Welding speed (mm/s)	Actual heat input (J/mm)	Power (W)	Cooling time (s)	Cooling rate (°C/s)	% Martensite	Standard Deviation
A1	168	14	33.3	33.7	1123.3	0.22	3098.8	0.22	0.08
A2	109	10	16.7	31.2	520.6	0.29	2396.4	0.43	0.14
A3	38	10	4.9	36.7	181.5	0.65	1067.7	3.37	0.59
A4	222	14	33.3	44.6	1484.4	0.27	2639.7	0.59	0.10
A5	130	10	16.7	37.2	620.9	0.33	2099.8	1.60	0.80
A6	50	9	4.9	43.5	214.9	0.72	978.9	2.49	0.52
A7	355	19	33.3	96.7	3221.4	0.77	905.8	1.65	0.28
A8	223	15	16.7	95.7	1597.6	0.87	808.5	2.58	4.19
A9	91	10	4.9	88.0	434.6	1.50	466.2	8.07	2.37
A10	301	16	16.7	137.7	2300.1	1.74	402.1	9.11	1.19
A11	189	14	8.2	153.6	1263.7	2.08	336.6	9.97	3.09
A12	125	10	4.9	120.9	597.0	2.59	270.7	10.03	1.57
A13	272	17	11.6	190.9	2208.4	2.39	293.0	15.08	4.81
A14	210	16	8.2	195.0	1604.7	2.63	266.3	16.39	5.64
A15	144	13	4.9	181.0	894.1	3.18	219.9	18.69	0.73
A16	252	17	8.2	248.6	2046.0	5.04	138.8	18.56	3.10
A17	168	13	4.9	211.1	1043.1	5.84	119.8	25.87	4.19
A18	118	11	2.4	262.7	619.9	8.27	84.6	26.58	2.37
A19	199	15	4.9	288.6	1425.6	6.53	107.1	32.98	3.93
A20	127	12	2.4	308.4	727.9	9.20	76.2	38.75	3.34
A21	219	16	4.9	338.8	1673.5	7.42	94.4	44.72	3.46
A22	135.5	12	2.4	329.1	776.6	10.20	68.7	45.13	3.28
A23	236	16	4.9	365.1	1803.4	7.66	91.4	46.88	1.35
A24	146	13	2.4	384.1	906.5	10.48	66.8	49.84	3.04
A25	252	17	4.9	414.2	2046.0	14.70	47.6	54.22	1.21
A26	164	13	2.4	431.5	1018.2	18.40	38.0	55.78	2.12

Heat input corrected for an arc efficiency of:  $h = 47.76\%$

Table B.7 Weld parameters, cooling time and rate (from 1500°C to 800°C) and % martensite measured in the high temperature heat-affected zone for 41311.

Weld	Welding current (A)	Arc potential (V)	Welding speed (mm/s)	Actual heat input (J/mm)	Power (W)	Cooling time (s)	Cooling rate (°C/s)	% Martensite	Standard Deviation
B1	168	13	33.3	31.3	1043.1	0.23	3061.9	0.81	0.28
B2	109	9	16.7	28.1	468.5	0.30	2374.2	5.78	1.21
B3	38	9.5	4.9	34.9	172.4	0.65	1079.5	6.88	0.61
B4	222	16	33.3	50.9	1696.4	0.26	2658.7	6.88	1.82
B5	130	10	16.7	37.2	620.9	0.33	2108.4	7.81	0.91
B6	50	9	4.9	43.5	214.9	0.72	977.5	10.94	0.91
B7	352	20	33.3	101.0	3362.3	0.82	858.0	5.94	1.52
B8	223	15	16.7	95.7	1597.6	0.91	769.5	12.69	3.04
B9	91	10	4.9	88.0	434.6	1.55	450.2	9.22	3.95
B10	301	16	16.7	137.7	2300.1	1.74	402.1	24.84	3.64
B11	190	15	8.2	165.4	1361.2	2.08	336.6	30.42	2.22
B12	125	10	4.9	120.9	597.0	2.61	268.7	30.00	3.64
B13	273	17	11.6	191.7	2216.5	2.39	292.7	22.19	3.04
B14	210	16	8.2	195.0	1604.7	2.60	269.2	37.66	3.95
B15	144	18	4.9	250.6	1237.9	3.20	218.7	40.63	1.82
B16	252	17	8.2	248.6	2046.0	5.04	138.8	45.63	6.07
B17	168	14	4.9	227.4	1123.3	5.84	119.8	53.13	5.46
B18	118	10	2.4	238.8	563.6	8.27	84.6	47.19	6.07
B19	199	15	4.9	288.6	1425.6	6.53	107.1	41.25	1.21
B20	127	12	2.4	308.4	727.9	9.20	76.2	51.25	10.32
B21	219	16	4.9	338.8	1673.5	7.42	94.4	60.31	4.86
B22	135.5	12.5	2.4	342.8	808.9	10.20	68.7	59.69	8.50
B23	236	16	4.9	365.1	1803.4	7.66	91.4	53.13	6.07
B24	146	13	2.4	384.1	906.5	10.48	66.8	56.56	1.21
B25	252	17	4.9	414.2	2046.0	14.70	47.6	58.28	3.34
B26	165	13	2.4	434.1	1024.5	18.40	38.0	70.31	3.64

Heat input corrected for an arc efficiency of:  $h = 47.76\%$

Table B.8. Number of HTHAZ grain boundaries with martensite in 41220.

Sample	Continuous ditched ferrite-ferrite	Percentage of grain boundaries that contain martensite	Continuous ditched ferrite-martensite	Weld	
				3CR12	3CR12+316L
A1	Yes	0%	Few	ü	
A2	Yes	0 to 4%	Few	ü	
A3	Yes	0 to 8%	Few	ü	
A4	Yes	0 to 17%	Few	ü	
A5	Yes	0 to 17%	Few	ü	
A6	Yes	0 to 17%	Few	ü	
A7	Yes	0 to 17%	Few	ü	
A8	Yes	0 to 17%	Few	ü	
A9	Yes	8 to 17%	Few	ü	
A10	Yes	8 to 50%	Few	ü	
A11	Yes	8 to 67%	Few		ü
A12	Yes	8 to 100%	Few		ü
A13	Yes	0 to 100%	Few		ü
A14	Yes	8 to 100%	Few	ü	
A15	Yes	17 to 100%	Localised		ü
A16	Yes	50 to 100%	Localised		ü
A17	Yes	50 to 100%	Localised		ü
A18	Localised	67 to 100%	Localised		ü
A19	Localised	67 to 100%	Localised		ü
A20	Localised	83 to 100%	Localised		ü
A21	Localised	92 to 100%	Localised		ü
A22	Localised	92 to 100%	Localised		ü
A23	Localised	92 to 100%	Localised		ü
A24	Localised	92 to 100%	Localised		ü
A25	Localised	100%	Localised		ü
A26	Localised	92 to 100%	Localised		ü

Table B.9 Number of HTHAZ grain boundaries with martensite in 41311

Sample	Continuous ditched ferrite-ferrite	Percentage of grain boundaries that contain martensite	Continuous ditched ferrite-martensite	Weld	
				3CR12	3CR12+316L
B1	Yes	0%	Few	ü	
B2	Yes	0 to 4%	Few	ü	
B3	Yes	0 to 8%	Few	ü	
B4	Yes	0 to 17%	Few	ü	
B5	Yes	0 to 17%	Few	ü	
B6	Yes	0 to 17%	Few	ü	
B7	Yes	0 to 17%	Few	ü	
B8	Yes	0 to 17%	Few	ü	
B9	Yes	8 to 17%	Few	ü	
B10	Yes	8 to 50%	Few		ü
B11	Yes	8 to 67%	Few		ü
B12	Yes	8 to 100%	Few		ü
B13	Localised	0 to 100%	Localised		ü
B14	Localised	8 to 100%	Localised		ü
B15	Localised	17 to 100%	Localised		ü
B16	Localised	50 to 100%	Localised		ü
B17	Localised	50 to 100%	Localised		ü
B18	Localised	67 to 100%	Localised		ü
B19	Localised	67 to 100%	Localised		ü
B20	Localised	83 to 100%	Localised		ü
B21	Localised	92 to 100%	Localised		ü
B22	Localised	92 to 100%	Localised		ü
B23	Localised	92 to 100%	Localised		ü
B24	Localised	92 to 100%	Localised		ü
B25	Localised	100%	Localised		ü
B26	Localised	92 to 100%	Localised		ü